Analysis of Sub-10 nm Precipitates Extracted from Microalloyed Steels

Dissertation zur Erlangung des Grades des
Doktors der Ingenieurwissenschaften
der Naturwissenschaftlich-Technischen Fakultät
der Universität des Saarlandes

von
M.Sc. Louis Weber

INM - Leibniz-Institut für Neue Materialien gGmbH
Arbeitsgruppe Strukturbildung

Saarbrücken, November 2021

Tag des Kolloquiums:	31. März 2022
Dekan:	Prof. Dr. Jörn Walter
Berichterstatter:	Prof. Dr. Tobias Kraus Prof. Dr. Christian Motz
Vorsitz:	Prof. Dr. Stefan Diebels
Akad. Mitarbeiter:	Dr. Frank Aubertin

Abstract

Analysis of Sub-10 nm Precipitates Extracted from Microalloyed Steels

by M.Sc. Louis Weber

Microalloyed steels contain small quantities ($\leq$ 0.5 wt%) of the microalloying elements Ti, Nb, V. Judicious combination of TMCP parameters and microalloyed steel composition leads to formation of desirable nm-sized carbide, nitride, carbonitride inclusions which improve steel mechanical properties. TMCP optimisation relies on understanding the interrelation between TMCP parameters and precipitate properties.

A characterisation routine was developed in the group to provide statistically meaningful data on precipitates size distribution and chemical composition.[1] Precipitates with diameters below 10 nm could not be investigated with the existing routine. Such precipitates are of interest because they play a key role in precipitation hardening.

This thesis extends the existing characterisation routine to sub-10 nm precipitates extracted from microalloyed steels. Electrolytic extraction was investigated as alternative extraction process to reduce undesired particle loss during chemical extraction. The suitability of various electrolytes to provide a stable colloidal suspension for colloidal analysis was assessed. Chemically extracted precipitates underwent differential centrifugation to isolate sub-10 nm precipitates and enable their size and chemical composition characterisation. Improvements in precipitate analysis were achieved by implementation of speed-ramp analytical ultracentrifugation and precipitate number density determination.

Zusammenfassung

Analysis of Sub-10 nm Precipitates Extracted from Microalloyed Steels

von M.Sc. Louis Weber

Mikrolegierte Stähle enthalten geringe Mengen ($\leq$ 0.5 wt%) der Mikrolegierungselemente Ti, Nb, V. Eine geschickte Kombination aus TMCP-Parametern und Stahlzusammensetzung führt zur Bildung nm-großer Karbid-, Nitrid-, Karbonitrideinschlüsse, die mechanische Eigenschaften verbessern. TMCP-Optimierung beruht auf dem Verständnis des Zusammenhangs zwischen TMCP-Parametern und Ausscheidungseigenschaften.

Eine vorhandene Charakterisierungsroutine liefert statistisch aussagekräftige Daten über die Größenverteilung und die chemische Zusammensetzung der Ausscheidungen.[1] Ausscheidungen mit Durchmessern unter 10 nm konnten mit der bestehenden Methode nicht untersucht werden. Solche Ausscheidungen sind von Interesse, da sie eine Schlüsselrolle bei der Ausscheidungshärtung spielen.

Diese Arbeit erweitert die bestehende Charakterisierungsroutine auf extrahierte Ausscheidungen kleiner 10 nm. Elektrolytische Extraktion wurde als alternatives Extraktionsverfahren erprobt, um unerwünschten Partikelverlust zu reduzieren. Die Eignung von Elektrolyten zur Bereitstellung einer stabilen kolloidalen Suspension zur Analyse mit kolloidalen Messmethoden wurde bewertet. Fraktionierung chemisch extrahierter Ausscheidungen mittels Differentialzentrifugation ermöglichte die Charakterisierung von Ausscheidungen kleiner 10 nm. Ausscheidungscharakterisierungsverbesserungen wurden durch Einführung der analytischen Ultrazentrifugation mit Geschwindigkeitsrampe und der Bestimmung der Ausscheidungsdichte erzielt.

Acknowledgements

I would like to thank my esteemed supervisor Prof. Dr. Tobias Kraus for his constant support and tutelage throughout my years as PhD candidate at INM-Leibniz Institute for New Materials.

I would like to express my sincere gratitude to the Aktien-Gesellschaft der Dillinger Hüttenwerk board for the financial support of this thesis. I would like to extend my gratefulness to Volker Schwinn (Aktien-Gesellschaft der Dillinger Hüttenwerke - Head of Research, Development and Design Department) and Dr.-Ing. Thorsten Staudt (Aktien-Gesellschaft der Dillinger Hüttenwerke - Heavy Plate Research Department) for entrusting me with this project and for the constructive and enjoyable cooperation.

I would also like to thank Prof. Dr. mont. Christian Motz for his activity as scientific advisor and second referee.

I would like to express my deep appreciation to Andreas Hegetschweiler who paved the way of this thesis, ensured knowledge transfer, and gave me judicious pieces of advice.

I am deeply grateful to Dr.-Ing. Johannes Walter (Friedrich-Alexander-Universität Erlangen-Nürnberg - Chair of Particle Technology) for his helping hand in implementing speed-ramp AUC and developing my AUC understanding.

I would like to thank the numerous structure formation group colleagues with whom I truly enjoyed working with over the years and especially Anna Zimmermann, Robert Strahl, Indra Backes, Long Zhang, and Lukas Engel. Special thanks go to Anja Colbus who not only was of great help in the lab with her experience and meticulousness, but also sparked new ideas with her curiosity and line of questioning.

I am deeply grateful for the support of so many colleagues at INM and in particular Isabella Tavernaro, Hwirim Shim, Christina Muth, Werner Schneider, Jörg Schmauch, Herbert Beermann, Uwe Magar, Andrea Jung, Sarah Schumacher, Birgit Nothdurft, Dr. Claudia Fink-Straube, Dipl.-Ing. Robert Drumm. I also thankfully acknowledge Jürgen Höpfner (Beckman Coulter), Martin Britscher, and Christian Ersfeld for their efforts in overcoming challenges posed by the AUC speed-ramp implementation. Special thanks go to Dr. Marcus Koch for sharing his knowledge and experience in eye-opening discussions.

I would like to thank Johannes Webel (Universität des Saarlandes - Chair of Functional Materials) and Dr.-Ing. Hongcai Wang (Ruhr Universität Bochum- Chair for Materials Science and Engineering) for the thrilling cooperations and fruitful discussions.

Finally I gratefully acknowledge Marc Laub (Universität des Saarlandes - Chair for Experimental Methodology of Materials Science), Selina Neuhaus (Universität des Saarlandes - Chair for Applied Mechanics), and Martin Müller (Universität des Saarlandes - Chair of Functional Materials) for informative exchanges during our meetings with the Aktien-Gesellschaft der Dillinger Hüttenwerke.

Statement on Contributions

I carried out all experiments and measurements presented in this thesis except for the ones listed below:

- Atom Probe Tomography (APT) investigations were carried out by Johannes Webel at Saarland University Chair of Functional Materials in Saarbrücken, Germany.
- Carbon Extraction Replicas (CERs) were produced by Jürgen Vogt and analysed by Dr. Thorsten Staudt at Aktien-Gesellschaft der Dillinger Hüttenwerke in Dillingen, Germany.
- Certain electrolytic cell components were designed and manufactured by Werner Schneider, Herbert Beermann from the INM-Leibniz Institute for New Materials Engineering department in Saarbrücken, Germany.
- Cryogenic Transmission Electron Microscopy (TEM) investigations were conducted by Dr. Marcus Koch from the INM-Leibniz Institute for New Materials Physical Analytics department in Saarbrücken, Germany.
- Electron transparent foils (ETFs) required for Scanning Transmission Electron Microscopy (STEM) investigations were prepared by Birgit Nothdurft from the INM-Leibniz Institute for New Materials Physical Analytics department in Saarbrücken, Germany.
- Foil thinning by ion milling and STEM analysis were both carried out by Jörg Schmauch from the Saarland University Experimental Physics department in Saarbrücken, Germany.
- Environmental scanning electron microscopy investigations were conducted by Lukas Engel from the INM-Leibniz Institute for New Materials Structure Formation group in Saarbrücken, Germany.
- Inductively Coupled Plasma Optical Emission Spectroscopy (ICP-OES) analyses were carried out by Andrea Jung from the INM-Leibniz Institute for New Materials Chemical Analytics department in Saarbrücken, Germany.
- Microalloyed steel samples were prepared for electrolytic and chemical extraction at Aktien-Gesellschaft der Dillinger Hüttenwerke in Dillingen, Germany and at the INM-Leibniz Institute for New Materials Engineering department in Saarbrücken, Germany.
- Silica nanoparticles were synthesised by Anja Colbus at the INM-Leibniz Institute for New Materials in Saarbrücken, Germany. Anja Colbus also contributed to chemical particle extractions and performed certain Dynamic Light Scattering (DLS) measurements.

Publication Report

In the frame of the cooperation between Aktien-Gesellschaft der Dillinger Hüttenwerke, Companhia Brasileira de Metalurgia e Mineração, Saarland University, and INM - Leibniz-Institute for New Materials efforts were joined to facilitate precipitate characterisation via Atom Probe Tomography (APT) for microalloyed steels with low precipitate densities:

- "Particle Encapsulation Techniques for Atom Probe Tomography of Precipitates in Microalloyed Steels" by Johannes Webel, Louis Weber, Emina Vardo, Dominik Britz, Tobias Kraus, and Frank Mücklich.
  The manuscript was submitted to *Ultramicroscopy*.
  https://doi.org/10.1016/j.ultramic.2021.113219

A manuscript presenting precipitate number density determination techniques in microalloyed steels is in preparation.

- "Complementary Precipitate Number Density Determination in Microalloyed Steels by Atom Probe Tomography and Matrix Dissolution" by Louis Weber, Johannes Webel, Frank Mücklich, and Tobias Kraus.

Contents

Abstract **iii**

Zusammenfassung **v**

Acknowledgements **vii**

Statement on Contributions **ix**

Publication Report **xi**

1 Precipitates in steel and their analysis **1**

2 Theory **7**
2.1 High-Strength Low-Alloy (HSLA) Steels . . . 7
2.2 Sample Preparation . . . 9
2.2.1 Electron Transparent Foils (ETFs) . . . 9
2.2.2 Carbon Extraction Replica (CER) . . . 9
2.2.3 Matrix Dissolution Technique (MDT) . . . 10
Chemical Extraction . . . 10
Electrolytic Extraction . . . 10
2.3 Characterisation Techniques . . . 13
2.3.1 Electron Microscopy . . . 13
Scanning Electron Microscopy (SEM) . . . 13
Transmission Electron Microscopy (TEM) . . . 14
Scanning Transmission Electron Microscopy (STEM) . . . 15
2.3.2 Analytical Ultracentrifugation (AUC) . . . 16
Sedimentation Velocity Experiment . . . 17
Speed Ramp Experiment . . . 19
Mathematical Theory of Particle Sedimentation . . . 19
Optical Particle Detection . . . 21

3 Experimental Methods **23**
3.1 Microalloyed Steel Samples . . . 23
3.2 Electron Transparent Foil Preparation . . . 23
3.3 Carbon Extraction Replica Preparation . . . 24
3.4 Matrix Dissolution Technique . . . 25
3.4.1 Chemical Particle Extraction . . . 25
3.4.2 Electrolytic Particle Extraction . . . 25
3.4.3 Silica Nanoparticle Synthesis . . . 27
3.5 Fractionation of Extracted Particles . . . 29
3.6 Particle Characterisation . . . 29
3.6.1 Analytical Ultracentrifugation (AUC) . . . 29
AUC Characterisation of Reference Gold Nanoparticles . . . 32
3.6.2 Atom Probe Tomography (APT) . . . 32

3.6.3 Dynamic Light Scattering (DLS) . . . 33
3.6.4 Electron Microscopy (TEM, STEM) . . . 33
3.6.5 Inductively Coupled Plasma Optical Emission Spectroscopy (ICP-OES) . . . 35

4 Results & Discussion **37**
4.1 Electrolytic Extraction of Sub-10 nm Particles . . . 37
4.1.1 Acetylacetone Electrolyte . . . 38
4.1.2 Methyl Salicylate / Salicylic Acid Electrolyte . . . 43
4.1.3 Maleic Acid Electrolyte . . . 43
4.1.4 Maleic Anhydride Electrolyte . . . 44
4.1.5 Summarising Remarks . . . 49
4.2 Size Fractionation of Chemically Extracted Particles . . . 50
4.2.1 Particle Fractionation Techniques . . . 50
Postextraction Fractionation . . . 51
Fractionating Characterisation Techniques . . . 53
4.2.2 Analytical Ultracentrifugation . . . 53
4.2.3 Differential Centrifugation Fractionation . . . 56
4.3 Post-Fractionation Analysis of Sub-10 nm Particles . . . 60
4.3.1 Size Distribution Determination . . . 60
Analysis of the Fractions . . . 60
Carbon Extraction Replica Analysis . . . 62
Error Sources in Size Distribution Determination via AUC . . . 63
4.3.2 Chemical Composition of sub-10 nm Particles . . . 66
4.4 Determination of the Density of Precipitates in Microalloyed Steel . . . 70
4.4.1 Precipitate Number Density Determination via AUC & ICP-OES 70
4.4.2 Precipitate Number Density Determination via APT . . . 72
4.4.3 Comparison of Precipitate Number Density Determination Techniques . . . 74
Degree of Niobium Precipitation . . . 74
Sample Homogeneity . . . 74
Measurement Errors & Statistical Uncertainties . . . 75
Particle Size Detection Limits . . . 77

5 Conclusion & Outlook **79**

A Mathematical Theory of Particle Sedimentation **81**
A.1 Sedimentation Equivalent Diameter Determination . . . 81
A.2 Core-Shell Particle Density Determination . . . 81
A.3 Particle Diameter Determination . . . 82

B Electrolytic Cell Setup **83**

C SR-AUC Implementation **85**
C.1 Reference Gold Nanoparticles . . . 85

D Automated STEM Analysis of Gold Nanoparticles **89**

Bibliography **91**

List of Figures

2.1 Microstructure evolution over TMCP stages. 8
2.2 CER production process. 10
2.3 Electrolytic cell based on the three electrode setup. 11
2.4 Electron-matter interaction generated signals. 13
2.5 Absorbance in SV-AUC. 17
2.6 Schematic representation of the AUC setup. 21
2.7 Double sector AUC cells with different centerpiece thicknesses. 22
2.8 Representation of **a** Rayleigh scattering and **b** Mie scattering for particles of different diameters (∅). 22

3.1 Electrolytic cell setup. 26
3.2 TEM characterisation of silica nanoparticles. 28
3.3 DLS characterisation of silica nanoparticles. 28
3.4 Schematic representation of differential centrifugation fractionation. . 29
3.5 Measurement parameters for SV-AUC and SR-AUC. 30

4.1 TEM analysis of steel fragments extracted in experiment n°1. 39
4.2 SEM working electrode analysis after experiment n°1. 39
4.3 TEM analysis of a SiO_x microparticle from experiment n°1. 40
4.4 TEM analysis of steel fragments extracted in experiment n°2. 40
4.5 SEM working electrode analysis after experiment n°2. 41
4.6 TEM analysis of SiO_x-network from experiment n°2. 41
4.7 TEM analysis of the suspension from experiment n°3. 42
4.8 TEM analysis of the suspension using Mizukami et al. [97] electrolyte. 43
4.9 TEM analysis of SiO_x-network with the maleic acid electrolyte. 44
4.10 TEM analysis of a SiO_x microparticle with the maleic acid electrolyte. . 44
4.11 NWPSDs for chemically and electrolytically extracted particles. 45
4.12 TEM analysis of the suspension using the maleic anhydride electrolyte. 46
4.13 TEM analysis of suspensions from experiment n°4 and 5. 47
4.14 NWPSDs of electrolytically extracted particles. 48
4.15 Impact of silica particle addition on electrolytic extraction. 49
4.16 TEM size distribution of particles chemically extracted from steel C. . . 50
4.17 NWPSDs via AUC and CER STEM analyses. 54
4.18 Turbidity density projections in SR-AUC. 55
4.19 DLS analysis of fractionation products. 57
4.20 AUC analysis of fractionation products. 57
4.21 TEM analysis of fractionation products. 58
4.22 Fractionation efficiency according to NWPSDs in AUC. 60
4.23 Impact of AUC cell centerpiece length on NWPSD. 61
4.24 Sub-10 nm particle analysis via SV-AUC and STEM on CER. 62
4.25 TEM analysis of SiO_x-network in chemically extracted particles. 64
4.26 TEM and AUC NWPSDs of chemically extracted particles. 64
4.27 Dependency of AUC NWPSD on particle material properties. 65

4.28 Mie-correction efficiency evaluation. 66
4.29 STEM analysis of sub-10 nm particles. 67
4.30 Monitoring of extracted particles' purification process via ICP-OES. . . 68
4.31 TEM analysis of particles chemically extracted from steel D. 71
4.32 Size analysis of particles chemically extracted from steel D. 71
4.33 APT analysis of steel D. 73
4.34 Precipitate formation homogeneity in steel D. 75
4.35 Precipitate number densities determined with APT and AUC/ICP-OES. 76
4.36 NWPSDs via AUC and APT for steel D. 77

A.1 Schematic core-shell particle representation. 82

B.1 Technical drawings of electrolytic cell electrodes. 83
B.2 Technical drawings of electrolytic cell electrode plugs. 84

C.1 EWPSDs provided by SV-AUC and SR-AUC. 85
C.2 MWL detector information in SR-AUC. 87

D.1 Automated STEM analysis of a gold nanoparticle mixture. 90

List of Tables

3.1 Composition of investigated microalloyed steels. 23
3.2 Chemicals for electrolytic extraction. 27
3.3 Chemicals for silica nanoparticle synthesis. 27
3.4 Zeta Potential measurements of silica nanoparticles in Milli-Q water. . 28
3.5 Estimated optical properties of extracted particles at $\lambda = 633\,\mathrm{nm}$. . . . 33

4.1 Complexing agents of the electrolytes. 38
4.2 10 wt% acetylacetone, 1 wt% TMAC, methanol. 38
4.3 10 wt% maleic anhydride, 2 wt% TMAC, methanol. 45
4.4 10 wt% maleic anhydride, 2 wt% TMAC, methanol, surfactants. 47
4.5 Fractionation parameters. 56
4.6 Variations in particle material properties for NWPSD determination. . 65
4.7 Ti and Nb content in collected fractions determined via ICP-OES. . . . 67
4.8 Precipitate identification in APT. 72
4.9 Precipitate number density in APT. 73
4.10 Summary of determined precipitate number densities. 74
4.11 Minimum precipitate diameters in AUC, APT, and STEM. 77

C.1 Diameters of reference gold nanoparticles in AUC, TEM, DLS. 86

List of Abbreviations

APT	**A**tom **P**robe **T**omography
AU	**A**nalytical **U**ltracentrifuge
AUC	**A**nalytical **U**ltra**c**entrifugation
CA	**C**omplexing **A**gent
CASRN	**C**hemical **A**bstracts **S**ervice **R**egistry **N**umber
CER	**C**arbon **E**xtraction **R**eplica
Cond.	**C**onductivity
DCDT	Time Derivative Method
DLS	**D**ynamic **L**ight **S**cattering
EDS	**E**nergy **D**isperse *X*-ray **S**pectroscopy
EELS	**E**lectron **E**nergy **L**oss **S**pectroscopy
EEPROM	**E**lectrically **E**rasable **P**rogrammable **R**ead-**O**nly **M**emory
Elec. Mob.	**E**lectrophoretic **M**obility
ETF	**E**lectron **T**ransparent **F**oil
EWPSD	**E**xtinction **W**eighted **P**article **S**ize **D**istribution
FFF	**F**ield **F**low **F**ractionation
FIB	**F**ocused **I**on **B**eam
FIM	**F**ield **I**on **M**icroscopy
F4	**F**low **F**ield-**F**low **F**ractionation
GS	**G**ravitational **S**weep
HSLA	**H**igh-**S**trength **L**ow-**A**lloy
ICP-MS	**I**nductively **C**oupled **P**lasma **M**ass **S**pectroscopy
ICP-OES	**I**nductively **C**oupled **P**lasma **O**ptical **E**mission **S**pectroscopy
MDT	**M**atrix **D**issolution **T**echnique
MWL	**M**ulti**W**ave**L**ength
NNLS	**N**on-**N**egative **L**east **S**quares
NWPSD	**N**umber **W**eighted **P**article **S**ize **D**istribution
ODF	**O**riented **D**ark **F**ield
PEELS	**P**arallel **E**lectron **E**nergy-**L**oss **S**pectroscopy
P/N	**P**art **N**umber
PSD	**P**article **S**ize **D**istribution
RCF	**R**elative **C**entrifugal **F**orce
SANS	**S**mall-**A**ngle **N**eutron **S**cattering
SCE	**S**aturated **C**alomel **E**lectrode
SDS	**S**odium **D**odecyl **S**ulfate
SEM	**S**canning **E**lectron **M**icroscopy
SP-ICP-MS	**S**ingle-**P**article **I**nductively **C**oupled **P**lasma **M**ass **S**pectroscopy
STEM	**S**canning **T**ransmission **E**lectron **M**icroscopy
SV	**S**edimentation **V**elocity
SR	**S**peed **R**amp
TEM	**T**ransmission **E**lectron **M**icroscopy
Temp.	**T**emperature
TEOS	**T**etra**E**thyl**O**rtho**S**ilicate

TMAC	**T**etra**M**ethyl**A**mmonium **C**hloride
TMCP	**T**hermo**M**echanical **C**ontrolled **P**rocessing
TTT	**T**ime **T**emperature **T**ransformation
XRD	**X**-**R**ay **D**iffraction

List of Symbols

c	electron velocity
C	sample concentration
$C(s)$	sedimentation coefficient dependent sample concentration
C_0	initial sample concentration
D	sample diffusion constant
E_k	electron kinetic energy
E_λ	extinction
f	frictional coefficient
$F(s)$	sedimentation coefficient distribution
$F(x)$	extinction frequency distribution
F_b	buoyant force
F_f	frictional force
F_g	gravitational force
$g(s)$	sedimentation coefficient distribution
h	Planck's Constant = $6.626\,07 \times 10^{-34}\,\mathrm{m^2 \cdot kg \cdot s^{-1}}$
j	scattering behaviour parameter
$K1$	rotor specific stretching factor
$K2$	rotor specific stretching factor
l	thickness of a body crossed by light
l_C	particle core radius
l_S	ligand shell thickness
m_0	electron velocity
m_C	total mass of carbon contained in the precipitates
$m_\mathrm{Dissolved\ Steel}$	mass of dissolved steel
m_Nb	total mass of niobium contained in the precipitates
m_P	particle mass
m_S	mass of displaced solvent
n_solvent	solvent refractive index
r	radius from center of rotation
r_d	detector position
r_m	meniscus position
r_P	particle-radius from center of rotation distance
$r_{Particle}$	particle radius
r_sb	sedimentation boundary radius
s	sedimentation coefficient
$s(t_\mathrm{i})$	sedimentation coefficient at detection time $\mathrm{t_i}$
S	Svedberg, $1\ \mathrm{S} = 1 \times 10^{-13}\ \mathrm{s}$
t	time
u	particle sedimentation velocity
v	sedimentation boundary velocity
V_Core	particle core volume
V_P	particle volume

V_{Shell}	particle shell volume
x	hydrodynamic particle diameter
ε_{λ}	extinction coefficient
η_{S}	solvent viscosity
λ	light wavelength
λ_{e}	electron wavelength
$\bar{v}$	partial specific volume
π	Pi = 3.141 59
ρ_{Core}	particle core density
ρ_{P}	particle density
ρ_{S}	solvent density
ρ_{Shell}	shell density
ρ_{Steel}	steel density
ω	rotor spinning velocity

Chapter 1

Precipitates in steel and their analysis

Microalloyed [2, 3], stainless [4–6], and low-carbon [7, 8] steels can contain inclusions ranging from clusters composed of a few atoms to micrometer sized particles. Nanoprecipitates in microalloyed steels greatly impact mechanical properties through precipitation hardening.[9–20] Microalloying elements (titanium, niobium, vanadium) are responsible for additional grain-refinement and solid solution strengthening.[15, 18–21] Niobium, for example, enables grain-refinement strengthening by forming carbide/carbonitride precipitates in austenite which delay austenite recrystallisation. Recrystallisation retardation allows for an increase in nucleation sites for the austenite/ferrite transformation, resulting in fine grain sizes.[20, 21] Several approaches have been developed to characterise inclusions regarding their size, shape, chemical composition, and to study their precipitation kinetics with the aim of controlling inclusion formation to achieve desired material properties. These approaches are either based on the investigation of bulk samples [2, 5, 9–14, 16–18, 22–45], replicated samples [46–50], dissolved samples where the inclusions are extracted from the iron matrix [4, 51–61] or a combination of the aforementionned approaches [1, 3, 6–8, 15, 19–21, 62–83]. This section provides an overview of state of the art characterisation techniques for nanoprecipitates in microalloyed steels.

Investigation of bulk samples

Metallographic sample preparation is required prior to microstructure investigations via light microscopy [9–13, 23–25, 29, 31, 36, 38–40, 44, 45] and/or scanning electron microscopy (SEM) [2, 5, 9, 17]. Energy dispersive X-ray spectroscopy (EDS) in SEM can be used for chemical composition analysis of micrometer sized particles protruding from the metallographic section. Electron transparent foils (ETFs) with an approximate thickness of hundred nanometres are prepared by thinning of lamellae produced in a focussed ion beam/scanning electron microscope (FIB/SEM) for transmission electron microscopy (TEM), EDS, scanning transmission electron microscopy (STEM), and electron energy loss spectroscopy (EELS) investigations.[2, 9–13, 16–18, 22–27, 30, 33–36, 38–40, 42, 44, 45, 84–87] Nanoscaled tips are needed for atom-probe tomography (APT) [2, 9–14, 22–42] and field ion microscopy (FIM) [28, 29, 31, 32]. Mechanical properties [9–13, 16–18, 27, 36, 39, 40, 44, 83], small-angle neutron scattering (SANS) [10, 12, 25, 27, 38, 83], and electrical resistivity [43] measurements also require specific sample preparations.

Studies exclusively analysing bulk samples mostly combine multiple characterisation techniques to investigate inclusions [2, 16, 18, 29, 30, 33, 35, 40, 42, 44, 45], precipitation kinetics [9, 11, 22, 23, 26–28, 31, 32, 36, 38, 39], strengthening mechanisms [17, 24], and hydrogen trapping at particles [34]. A combination of different

characterisation techniques allows for detailed studies, because they yield complementary pieces of information and allow for comprehensive analysis of steels.[10, 12, 13, 25] Only a few cases are reported where a single characterisation technique is employed.[5, 14, 37, 41, 43, 86, 87]

Investigation of bulk samples requires time-consuming sample preparation for each characterisation technique that has to be used and suffers from poor statistics when determining particle size distributions. Investigating extraction replicas and/or using the matrix dissolution technique allows to overcome this statistical limitation. Extraction replicas can easily be produced and are preferred to investigations on bulk samples for rapid particle characterisation.

Investigation of replicated samples

Precipitates protruding from the metallographically prepared surface of samples can be transferred onto a thin film for subsequent electron microscopy analysis. The thin film containing extracted precipitates is referred to as extraction replica. Extraction replicas with a carbon [47, 49, 50], Al_xO_y [46], or Al [46, 49] film can be used to analyse inclusions in microalloyed steels by electron microscopy (TEM, STEM, EDS, EELS).[8, 79, 80, 85]

Investigation of extraction replicas is a well-established, straightforward technique for precipitate characterisation. Compared to the investigation of ETFs, extraction replicas only contain the particles on a thin film of carbon or aluminium based material. Therefore, no matrix contribution is measured in EDS or EELS [47, 88], while the spatial resolution is retained. Analysis of extraction replicas suffers from several limitations. Etching steps are involved in the preparation of extraction replicas, which can lead to undesired particle loss.[48, 88] Extraction replicas also suffer from a lack of reproducibility.[89] TEM investigation of extraction replicas and bulk samples only allows for time-consuming analysis of a small sample volume.[19, 20, 90] Additionally, detection of sub-10 nm particles in bright-field imaging can be challenging because of the particles low contrast.[91] Therefore, electrical resistivity measurements or chemical analysis should be preferred to electron microscopy when determining the volume fraction of particles in a sample.[89, 92] Because carbon extraction replicas (CERs) do not allow for an unbiased carbon analysis of particles due to the carbon film, Scott et al. [46] developed carbon-free, aluminium based films. These films are used for carbon analysis and carbon-nitrogen ratio determination of inclusions.[46] However, precipitate analysis with CERs remains the standard procedure in the industry.

Smith and Nutting [47] have shown the suitability of CERs to investigate carbides in the nanometre range contained in microalloyed steels via TEM. Craven et al. [49, 50] employed CERs to investigate TiNb(CN) and non-titanium based nanoparticles in microalloyed steels via electron microscopy. Particle size distributions were determined and sub-10 nm niobium based particles could be imaged. Béreš et al. [20] and Craven et al. [50] proved that analysis of sub-10 nm particles via CER combined with electron microscopy is feasible. Annular dark field imaging proved to be valuable for morphology investigations and parallel electron energy-loss spectroscopy (PEELS) allowed for a detailed chemical composition analysis of particles composed of several phases.

Beyond particle characterisation CERs can be combined with investigations on bulk microalloyed steel samples to determine the impact of precipitation strengthening on mechanical properties. The latter can be determined by measuring the hardness, elongation, yield and tensile strength of the microalloyed steel after different thermomechanical controlled processing (TMCP) routes.[19, 81] Combining CER investigation and measurement of mechanical properties allows to follow precipitation kinetics and to assess the strengthening mechanisms of alloying elements in solution and particles.[15, 20, 21] Following the microstructure of the metallographically prepared bulk sample throughout the TMCP route via light microscopy, combined with CERs investigation also allows for study of precipitation kinetics.[74, 82]

A combined investigation of CERs and bulk samples can also allow for detailed precipitation kinetics studies. The bulk sample is characterised via electrical resistivity measurements [75–77] and APT [62, 68]. APT allows for highly precise three-dimensional analysis of inclusions ranging from clusters to nanoparticles regarding chemical composition, size, and shape. Such clusters can barely be investigated through electron microscopy of thin-foils or extraction replicas.[62] APT also allows for detection of alloying elements dissolved in the matrix, which can foster understanding precipitation kinetics when combined with electrical resistivity measurements.[68]

Matrix dissolution technique

The investigation of dissolved samples is also referred to as matrix dissolution technique.[1, 51, 64, 66] It consists in dissolving the iron matrix either chemically with acids [1, 7, 51, 52, 55, 57, 58, 60, 61, 63–67, 70, 93, 94] or halogens [6, 56, 58–60, 70, 94], or electrolytically to extract inclusions. The electrolytic extraction process requires to wire the investigated steel sample as an anode and to immerse it in an electrolyte that can be aqueous [53, 69, 71, 95] or non-aqueous [3, 4, 6, 64–66, 70, 72, 73, 78, 94–97].

The matrix dissolution technique was developed in the last century to extract non-metallic inclusions such as Al_2O_3 and SiO_2 from steel.[55, 58] Chemical extraction was predominantly used and followed by the so-called residue method [55] to determine the quantity of non-metallic inclusions in the steel sample. Later on, XRD [60, 61] of the dried extracted particles, chemical analysis, and spectrochemical analysis [60] were introduced for characterisation. More recently electrolytic extraction was combined with SEM and EDS to analyse micrometer sized rare earth metal oxides in stainless steel [4] and ferroalloys [96]. Matrix dissolution plays an increasingly important role in the analysis of precipitates in microalloyed steels. Lu et al. [51] investigated niobium-rich nanoparticles in a Grade 100 microalloyed steel by combining chemical extraction using acids with TEM/EDS, XRD, and ICP analysis. Qualitative chemical composition estimation and particle size distribution determination were successfully carried out.[51] Others used chemical [52, 57] and electrolytic [53] extraction to successfully isolate the particles from the iron matrix of microalloyed steels, allowing for particle characterisation utilising electron microscopy, XRD, and spectrophotometrical methods.

The matrix dissolution technique has the advantage to allow for analysis of orders of magnitude more precipitates than investigations on bulk and replicated samples. It enables colloidal analysis of extracted precipitates. The matrix dissolution technique

suffers from two major limitations. SiO_x-network formation was reported for chemical extraction using acids.[1, 51, 52, 64, 65] The sol-gel like formation of this network [98] leads to an enclosure of the extracted particles in amorphous SiO_x hindering subsequent particle analysis. Undesired particle loss is inherent to the matrix dissolution technique [52, 63, 67, 71, 94] and must be reduced to avoid obtention of biased size distributions when analysing the extracted particles. Inoue et al. [94] investigated the applicability of chemical and electrolytic extraction methods for specific oxide and sulfide particles regarding dissolution loss. Rivas et al. [69] and Yamada et al. [54] published reviews regrouping previously tested extraction methods for specific types of particles and steels. Hegetschweiler et al. [52] investigated the impact of differently concentrated acids and reactant temperature upon Ti(CN) and Nb(CN) nanoparticle etching. An improved extraction protocol employing sulfuric acid and a dispersant agent was presented to reduce particle etching and achieve colloidally stable suspensions. Due to remaining undesired particle loss the matrix dissolution technique does not allow for the characterisation of smallest precipitates compared to investigations on bulk and replicated samples. A combination with the analysis of bulk or replicated samples gives access to the complete precipitate size range.

The extracted particles can be separated from the solvent for characterisation purposes by filtering [3, 4, 6, 7, 55–58, 61, 63, 69–73, 78, 93, 96] or centrifugation [1, 51–53, 59, 64–67]. Filtering is often preferred when investigating micrometer sized inclusions.[3, 4, 7, 73, 96] Centrifugation is recommended to avoid particle loss through filter retention when nanoparticles as small as two nanometres in diameter need to be collected.[1, 51, 52] Extracted particles have been analysed by electron microscopy techniques (TEM, STEM, EDS), spectrometry (inductively coupled plasma mass spectrometry ICP-MS, inductively coupled plasma optical emission spectrometry ICP-OES, single-particle inductively coupled plasma mass spectrometry SP-ICP-MS), X-ray diffraction (XRD), and colloidal characterisation techniques (analytical ultracentrifugation AUC, field flow fractionation FFF, dynamic light scattering DLS). These complementary characterisation techniques enable a more efficient inclusion analysis compared to the characterisation techniques utilised for bulk and replicated samples. They provide statistically meaningful data for determination of particle size and chemical composition.[1, 53, 64, 67, 69, 83, 95, 99–101]

The matrix dissolution technique does not allow for spatially resolved investigation of inclusions and therefore needs to be combined with the analysis of bulk samples or replicated samples if particle location in the steel matrix is relevant. Comparative particle characterisation using SEM on metallographically prepared surfaces and on extracted particles showed that particle size, shape, chemical composition can only be precisely determined for extracted particles. Investigations on the sample surface only allow for location of the particles and rough estimation of the size and chemical composition of micrometer sized precipitates.[3, 6, 7, 63, 70, 73] Nonetheless combining the matrix dissolution technique and investigations of bulk samples provides valuable data upon precipitation kinetics [71], precipitation effect on mechanical properties, and strengthening kinetics [78, 83], and particle stability [69, 94] that could not be obtained through analysis of extracted particles alone. The investigation of extracted titanium and/or niobium carbonitride nanoparticles was combined with TEM or STEM investigation of CER to validate the matrix dissolution technique by monitoring possible particle loss [64, 69] and to validate the particle size distribution data provided by SP-ICP-MS [67], AUC, and FFF [1, 95, 99–101]. Lu et al.

[65, 66] used TEM-foils to study bulk particles unaltered by the CER production and extraction procedure. For an extensive steel sample characterisation additional microstructural analysis was carried out by means of light microscopy and SEM on a metallographically prepared bulk sample surface.[66] Park et al. [72] combined the investigation of extracted particles and CER with electrical resistivity measurements on a bulk sample to go beyond particle characterisation and study precipitation kinetics.

Analysis of precipitates with diameters below 10 nm

Precipitates with diameters below ten nanometres form in microalloyed steel for instance during the accelerated cooling step of TMCP. They significantly improve microalloyed steels yield strength through precipitation hardening. The contribution of fine precipitates to yield strength improvement can be enhanced by reducing their size and increasing their volume fraction.[1, 102, 103]

Precipitates with diameters below ten nanometres can be investigated on bulk and replicated samples. Electron microscopy investigations of microalloyed steel ETFs allow for determination of size, shape, chemical composition, and location of fine precipitates in the steel matrix.[15, 18, 80] Particles with diameters below ten nanometres have been successfully imaged [2, 26, 30, 38, 39, 42, 65, 66], but extensive characterisation is often carried out via APT [2, 26, 30, 38, 39, 42] or CER [65, 66]. APT is preferred because it is a high-resolution three-dimensional characterisation method. TEM investigations of precipitates with diameters below ten nanometres on CERs are feasible.[20, 50, 84] Craven et al. [50] employed PEELS for precise chemical composition determination of single particles. They claim that the fine precipitates observed are either Nb(CN), NbC, or NbTiC depending on the composition of the investigated microalloyed steel.

The matrix dissolution technique enables extraction of precipitates with diameters below ten nanometres. Lu et al. [65, 66] showed that precipitates with diameters below ten nanometres can be extracted successfully. Artefacts due to the extraction process such as agglomerated particles, or the engulfment of precipitates in a SiO_x-network hindered extensive TEM investigations of extracted precipitates with diameters below ten nanometres. Therefore, particle size distribution determination via TEM analysis of CERs was preferred to TEM analysis of extracted particles.[65] Hegetschweiler et al. [52] present a novel chemical extraction process using sulfuric acid to overcome existing limitations in TEM analysis of extracted particles due to SiO_x-network formation and enable sub-10 nm precipitate characterisation. Particle size distributions of extracted particles could be determined via TEM [1] and STEM [67]. Precipitates with diameters below ten nanometres are reported and EDS [67] allowed for qualitative chemical composition analysis of these fine precipitates. Hegetschweiler et al. [67] introduced SP-ICP-MS as a powerful characterisation technique for size distribution and chemical composition determination of extracted precipitates. Nb and Ti based precipitates with diameters below ten nanometres cannot be analysed by means of SP-ICP-MS due to apparatus limit of detection. Besides well-established chemical and TEM analysis of extracted particles, colloidal characterisation techniques have recently been reported to be suitable for characterisation of fine precipitates.[1, 99–101]

Outlook

Characterisation of sub-10 nm precipitates in microalloyed steels is possible via investigations on bulk and replicated samples but limited to samples with high particle number densities. Numerous bulk and replicated samples investigated in the literature exhibit high particle number densities, because they contain precipitations in the ferritic phase.[8, 11, 14, 16–18, 20, 25–28, 30, 32–36, 38–42, 44, 62, 80] Particle number density in microalloyed steels depends upon thermomechanical processing.[9, 10, 13, 22] It is not always possible to select the thermomechanical processing route in such a way that the particle number density is high enough to allow for bulk sample (APT, thin-foils) and extraction replica investigations.

The matrix dissolution technique is required to enable precipitate analysis for microalloyed steel samples displaying insufficient particle number densities for investigations on bulk and replicated samples. Matrix dissolution combined with colloidal characterisation techniques allows for swift analysis of numerous, including sub-10 nm, particles ($> 10^9$). To the best of the author's knowledge only a few studies concerning analysis of particles extracted from microalloyed steels via colloidal characterisation techniques have been carried out.[1, 67, 97, 99–101, 104]

This thesis aims at extending the combination of matrix dissolution technique with AUC, electron microscopy, ICP-OES to sub-10 nm precipitate analysis. The reliability and robustness of the developed characterisation routine were discussed with respect to CER investigations. The developed characterisation routine is thought to greatly benefit precipitation kinetics studies when combined with investigations of bulk samples such as electric resistivity, mechanical properties and/or matrix APT measurements.[105] This thesis implements an electrolytic and chemical matrix dissolution technique for microalloyed steel samples to enable analysis of extracted sub-10 nm precipitates. The suitability of electrolytic precipitate extraction for precipitate extraction with a minimised particle loss compared to chemical extraction was studied. Several electrolytes were tested to achieve stable colloidal suspensions suitable for AUC analysis. Extracted precipitates were extensively characterised to present insights on shape, size, and chemical composition of precipitates in the sub-10 nm range. In addition to sub-10 nm precipitate characterisation this thesis also presents a precipitate number density determination technique combining AUC analysis of chemically extracted precipitates and ICP-OES analysis of the bulk sample. Results were discussed in the light of complementary APT and ETF investigations.

Chapter 2

Theory

2.1 High-Strength Low-Alloy (HSLA) Steels

The chemical composition of HSLA steels can be adapted to achieve specific mechanical properties, corrosion resistance, and good weldability. Tensile strengths of HSLA steels range from 275 to 450 MPa [106, 107], a better strength-to-weight ratio than common low-carbon steels. This is exploited in offshore structures, pipelines, storage tanks, and structural parts of industrial equipment.[106]

This thesis focuses on a type of HSLA steel referred to as microalloyed steel.[106] Microalloyed steels can be defined as low-carbon alloy steels with no alloying element exceeding 5 wt%.[108] Typical alloying elements added in small quantities (< 0.1 wt%) are titanium, niobium, and vanadium.[106] They induce desirable titanium, niobium, or vanadium based carbide, nitride, or carbonitride nanoparticle formation in the microalloyed steel during TMCP. The particles cause precipitation, grain-refinement, and also solid solution strengthening thereby guaranteeing the outstanding mechanical properties of microalloyed steels.[15–21, 109] Detailed explanations on the working principle of the above mentioned strengthening mechanisms can be found in reviews and monographies [1, 95, 110–112].

Thermomechanical Controlled Processing (TMCP)
TMCP combines thermal (heat treatment, cooling) and mechanical (rolling) processing of microalloyed steel slabs to achieve precipitate formation and fine grain size (1-3 µm). TMCP involves subsequent reheating, rolling, and accelerated cooling (**Fig. 2.1**).[1, 103, 113–115] First, casted microalloyed steel slabs undergo reheating. Temperatures up to 1 250 °C are necessary to dissolve most of the microalloying elements that precipitated during slab casting. Due to their low solubility in austenite titanium nitride precipitates do not dissolve completely upon reheating. These inclusions with a size of approximately 300 nm end-up pinning austenite grain boundaries and prevent grain coarsening.[1, 95, 103, 113, 114, 116]

In the second stage the microalloyed steel slab is cooled down, but maintained above recrystallisation temperature for rough rolling. Rough rolling leads to a defect free structure of fine austenite grains. The subsequent finish rolling is carried out at a temperature between the recrystallisation and the austenite to ferrite transformation temperature. The applied plastic deformations elongate austenite grains. Besides a microstructural change and obtention of the so-called pancake austenite, finish rolling also results in the formation of precipitates 50 nm in size. Strain-induced precipitation of titanium, niobium, and vanadium allows for microstructure control during TMCP.[1, 95, 103, 113, 114]

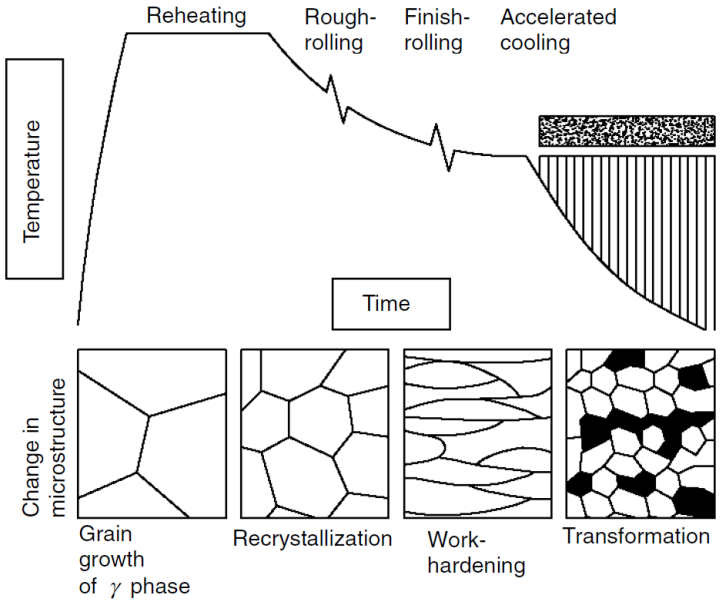

FIGURE 2.1: Effect of the different TMCP stages on the steel microstructure. Figure adopted with permission from [117].

In the third stage accelerated cooling is carried out to form ferrite with desired microstructure. Depending on the cooling rate bainite, perlite, or martensite can be formed besides ferrite and affect mechanical properties.[1, 95, 103, 113, 114] The ferrite grain size depends upon finish rolling parameters. Strong deformations lead to numerous lattice defects which result in nucleation sites for the ferrite to austenite transformation. The more nucleation sites, the smaller the ferrite grain size. The accelerated cooling step is also responsible for the formation of precipitates smaller 10 nm. These particles contribute to the mechanical property profile of the microalloyed steel through precipitation hardening.

This thesis aims at providing a characterisation routine for sub-10 nm particles. This routine can be used to characterise precipitates for a given microalloyed steel sample and TMCP stage. Knowing the property profile of these particles the effect of TMCP parameter changes on the particle properties can subsequently be monitored to optimise TMCP. Optimisation of TMCP can be carried out based on theoretical approaches. The knowledge of solubility products of titanium, niobium, or vanadium based nitrides and carbides allows for a more controlled TMCP. Parameter variations in TMCP can affect precipitation hardening and grain refinement strengthening efficiency [1, 115, 116], for instance to keep some niobium in solid solution and form precipitates smaller 10 nm that strengthen the microalloyed steel.[103] Extensive precipitate characterisation (chemical composition, size, shape) helps tuning TMCP parameters to achieve specific precipitates. Combined with microstructure control microalloyed steels with highly specific property profiles could be produced. Precipitate characterisation via investigation of pristine, replicated and/or dissolved samples requires proper sample preparation.

2.2 Sample Preparation

Chapter 1 reviews published precipitate analyses of bulk, replicated, and dissolved microalloyed steel samples.

2.2.1 Electron Transparent Foils (ETFs)

Electron transparent foils of microalloyed steel samples can be prepared by target preparation via FIB.[26, 118] Trenches are milled in the bulk material to bare a foil of microalloyed steel. The foil is then lifted out, attached to a grid and ion milled to remove FIB preparation artefacts and to reach electron transparency thickness. Other ETF preparation technique are based on mechanical polishing with subsequent ion polishing [79, 118] or electropolishing [9, 118].

Thin foils are useful to locate precipitates in the steel structure [15, 65, 66] and to determine the orientation relationship between precipitates and matrix [8, 22]. TEM investigations of thin foils also allow for size and chemical composition determination of precipitates.[15, 18, 80] Reliable EDS measurements are limited to precipitates significantly larger than the electron beam. A matrix contribution is measured for smaller particles. The steel matrix is not only detrimental to EDS analysis of fine precipitates. Its magnetic field also interacts with the electron beam.[15, 79, 80] Size determination via TEM investigation of ETFs can be falsified by precipitates cut during ETF preparation and overlapping precipitates. Contrast-based sub-10 nm precipitate identification is a limitation of electron microscopy investigations on ETFs. The generated contrast intensity depends upon the precipitate volume and crystallographic orientation. Electron diffraction and weak electron scattering at sub-10 nm precipitates limit the contrast intensity. Further the foil thickness, interactions of the electron beam with the magnetic sample and sample heterogeneity impact precipitate identification.

2.2.2 Carbon Extraction Replica (CER)

The first step in CER preparation of a steel sample consists in producing a polished metallographic section (**Fig. 2.2 1**). After cleaning the sample is etched until the microstructure becomes visible in light microscopy. The inclusions are now protruding from the steel matrix (**Fig. 2.2 2**). Then a thin carbon film (< 100 nm) is evaporated or sputtered onto the metallographic section (**Fig. 2.2 3**).[118, 119] Carbon film thickness is crucial for subsequent TEM investigation. For sub-10 nm particles significantly smaller than the carbon film thickness poor contrast and blurriness due to the amorphous carbon will impede characterisation.[88, 89] A second etching step or electropolishing is required to float off the carbon film from the steel matrix (**Fig. 2.2 4**). Alternatively electropolishing can be employed.[1, 120, 121] The sample can be ground and polished to prepare additional CERs.[47] CERs can be investigated via TEM and STEM to determine particle size distribution and chemical composition (EDS, EELS).[8, 20, 21, 49, 50, 62, 72, 74–77, 79, 80, 82, 85]

Besides carbon film thickness considerations the investigation of CERs for sub-10 nm particle analysis suffers from particle loss which can occur through undesired etching of inclusions that will end up being attached to the carbon film during **2** and **4** (**Fig. 2.2**).[1, 48, 88] Undesired etching of sub-10 nm particles leads to characterisation of a biased system. Sub-10 nm particles contained in the steel at a depth that lies

between the metallographic section and the bottom of the largest particles attached to the carbon film can be flushed away in **2** and **4** (**Fig. 2.2**). This second type of particle loss results in a biased particle size distribution shifted towards larger particle diameters.[88, 92] Formation of aggregates during CER production [88] adds to the limited extraction efficiency [1] and lack of reproducibility [89] of CERs. Ashby et Ebeling [89] came to the conclusion that CERs are suitable for the determination of volume fraction of particles in steel, but that more accurate methods should be preferred.

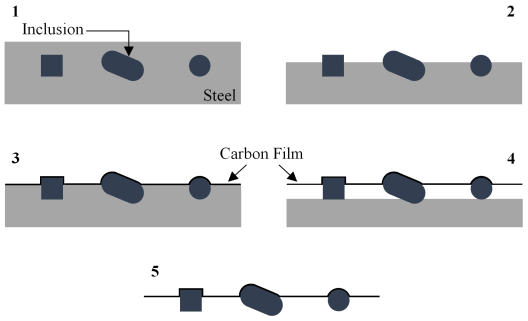

FIGURE 2.2: Steps in the CER production process: **1** Preparation of a polished metallographic section, **2** Partial free-etching of particles, **3** Carbon film deposition, **4** Second etching step, **5** Final CER after removal from the steel sample. Figure adapted with permission from [120].

2.2.3 Matrix Dissolution Technique (MDT)

Sub-10 nm particles have successfully been extracted via chemical extraction [1, 65–67]. Hegetschweiler et al. [52] provided a chemical extraction procedure mitigating undesired particle etching and SiO_x-network formation. This thesis adopts their chemical extraction procedure and extends the existing characterisation routine to sub-10 nm particles. Electrolytic extraction is tested as an alternative extraction process to further reduce undesired particle loss.

Chemical Extraction

Sulfuric or hydrochloric acid is added to microalloyed steel chippings to dissolve the iron matrix. A dispersing agent stabilises the extracted precipitates.[52, 93] The released particles are isolated for characterisation purposes. To avoid particle loss through filter retention centrifugation is preferred to filtration when collecting nano-sized precipitates.[1, 51, 52] TEM [51, 52, 65–67], spectrometry (ICP-OES, SP-ICP-MS) [51, 52, 65–67], XRD analysis [61, 65, 66], and more recently colloidal characterisation techniques (AUC, FFF) [1] have been reported for particle characterisation.

Electrolytic Extraction

Electrolytic extraction of inclusions from microalloyed steel requires an electrolytic three electrode setup (**Fig. 2.3**) composed of a working, a counter and a reference electrode. The electrochemical steel dissolution takes place at the working electrode. The reference electrode allows to monitor the working electrode potential and the counter electrode carries the current together with the working electrode. Reduction occurs at the cathode (**Eq. 2.1**) and oxidation occurs at the anode (**Eq. 2.2**). During

operation of an electrolytic cell the oxidoreduction reaction (**Eq. 2.3**) takes place. The electrolyte conductivity is caused by movement of ionic species. Convection, migration, and diffusion are the three transport mechanisms reported for ions in the electrolyte.[122] Stirring the electrolyte reduces transportation induced kinetic inhibitions of the oxidoreduction reaction.

$$Ox_1 + n_1 \cdot e^- \rightarrow Red_1 \tag{2.1}$$

$$Red_2 \rightarrow Ox_2 + n_2 \cdot e^- \tag{2.2}$$

$$n_1 \cdot Red_2 + n_2 \cdot Ox_1 \rightarrow n_2 \cdot Red_1 + n_1 \cdot Ox_2 \tag{2.3}$$

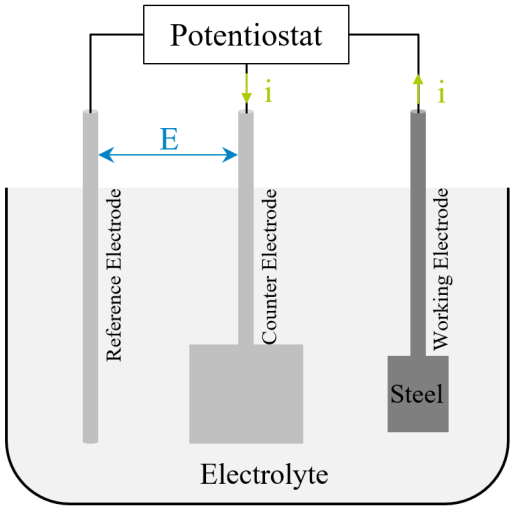

FIGURE 2.3: Electrolytic cell based on the three electrode setup with i the current flowing through the cell and E the potential between the counter and reference electrodes. The reference electrode ensures application of a desired potential. The counter electrode balances the current observed at the dissolving working electrode.

Numerous aqueous and non-aqueous electrolyte compositions are suitable for electrolytic inclusion extraction.[54, 69] Non-aqueous electrolytes are typically composed of a complexing agent (CA), a supporting electrolyte, and a solvent. The CA complexes the dissolved iron ions and keeps it in solution. The supporting electrolyte provides non-reacting ions that increase electrolyte conductivity and ensure that transport is diffusion-limited.[122, 123] The solvent has to be compatible with the CA and the supporting electrolyte in terms of solubility and stability. A non-aqueous electrolyte composed of acetylacetone, tetramethylammonium chloride (TMAC), and methanol has been used for extraction of titanium and niobium based precipitates from microalloyed steels.[54, 66, 78] Instead of acetylacetone other CAs such as methyl salicylate/salicylic acid [54, 94, 97], maleic acid [69], maleic anhydride [54, 94] can be used for electrolytic extraction.

This paragraph focuses on a methanol-based electrolyte containing acetylacetone as CA and the quaternary ammonium salt TMAC as supporting electrolyte. The protogenic solvent methanol also takes part in the oxidoreduction reaction for this electrolyte composition. Iron is oxidised at the anode to iron(II) (**Eq. 2.4**) or iron(III) (**Eq. 2.5**), methanol is reduced at the cathode to a methoxide anion (**Eq. 2.6** or **Eq. 2.7**), and the protons recombine to gaseous hydrogen. The metoxide anion is attracted

towards the anode, i.e. the working electrode, where ferrous methoxide is formed on the steel surface (**Eq. 2.8** or **Eq. 2.9**). The ferrous methoxide reacts with the CA and is removed from the anode surface (**Eq. 2.10** or **Eq. 2.11**).[124]

$$Fe \rightarrow Fe^{2+} + 2 \cdot e^{-} \tag{2.4}$$
$$or \quad Fe \rightarrow Fe^{3+} + 3 \cdot e^{-} \tag{2.5}$$

$$2 \cdot CH_3OH + 2 \cdot e^{-} \rightarrow 2 \cdot CH_3O^{-} + H_2 \tag{2.6}$$
$$or \quad 3 \cdot CH_3OH + 3 \cdot e^{-} \rightarrow 3 \cdot CH_3O^{-} + \frac{3}{2} \cdot H_2 \tag{2.7}$$

$$Fe^{2+} + 2 \cdot CH_3O^{-} \rightarrow Fe(OCH_3)_2 \tag{2.8}$$
$$or \quad Fe^{3+} + 3 \cdot CH_3O^{-} \rightarrow Fe(OCH_3)_3 \tag{2.9}$$

$$Fe(OCH_3)_2 + 3 \cdot CA \rightarrow FeCA_3{}^{2+} + 2 \cdot CH_3O^{-} \tag{2.10}$$
$$or \quad Fe(OCH_3)_3 + 3 \cdot CA \rightarrow FeCA_3{}^{3+} + 3 \cdot CH_3O^{-} \tag{2.11}$$

Potentiodynamic polarisation curves are used to determine the potential range allowing for inclusion extraction with minimised particle loss.[66, 125, 126] Electrolyte potentials ranging from -0.3 to 0.5 V vs saturated calomel electrode (SCE) were estimated suitable for HSLA steel dissolution in the acetylacetone electrolyte.[66] The dissolution rate depends upon the applied potential and is limited by undesired particle etching. Exceeding 0.5 V vs SCE leads to pronounced dissolution of titanium and niobium-based precipitates. Compared to chemical inclusion extraction, electrolysis requires more time to dissolve the same sample quantity.[6] Applying less than -0.3 V vs SCE does not allow for microalloyed steel dissolution.

The extracted precipitates have been isolated via centrifugation or filtration and then analysed for size, shape, and chemical composition via colloidal characterisation techniques (FFF, DLS, AUC) [1, 95] and spectrometry (ICP-OES, ICP-MS) [3, 69, 78, 95]. The dried suspension can also be analysed via electron microscopy (TEM, SEM, EDS) [3, 4, 6, 53, 64, 73, 95, 96] and XRD [3, 53, 60, 61, 64, 69].

2.3 Characterisation Techniques

2.3.1 Electron Microscopy

Secondary electrons and backscattered electrons are used for imaging purposes in scanning electron microscopy (SEM) (**Fig. 2.4**). Transmission electron microscopy (TEM) relies on direct beam, or scattered electrons for imaging. Chemical composition determination in SEM and TEM is achieved via characteristic X-rays analysis. In scanning transmission electron microscopy (STEM) chemical analysis can also be carried out by monitoring the energy distribution of inelastically scattered electrons for electron energy loss spectroscopy (EELS) to investigate e.g. atom coordination. The electron beam size can be adapted via apertures to maintain beam coherence, adapt image contrast, or perform energy dispersive X-ray spectroscopy (EDS) point measurements. The theoretical limit of resolution for an electron microscope depends on the smallest electron wavelength achievable. An increase in acceleration voltage reduces the electron wavelength (**Eq. 2.12**). Electron microscopy analysis of sub-10 nm particles is limited by sample preparation aspects rather than by SEM, TEM, STEM resolution.

$$\lambda_e = \frac{h}{\left[2 \cdot m_0 \cdot E_k \cdot \left(1 + \frac{E_k}{2 \cdot m_0 \cdot c^2}\right)\right]^{\frac{1}{2}}} \tag{2.12}$$

with the electron wavelength λ_e, Planck's constant h, the electron velocity m_0, the electron kinetic energy E_k, the electron velocity c.

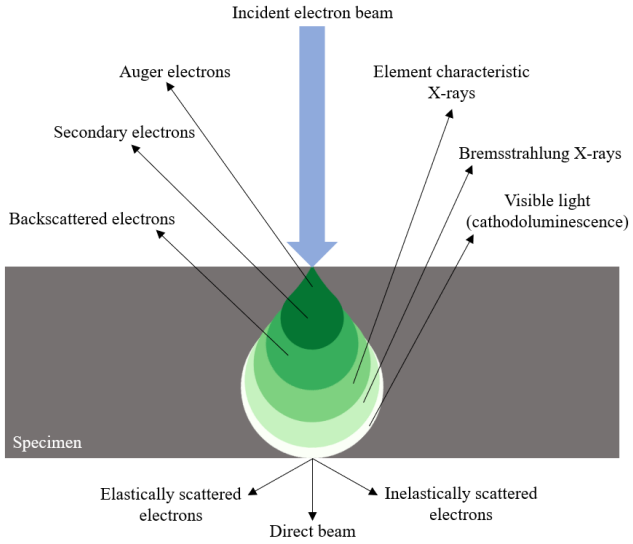

FIGURE 2.4: Signals generated by electron-matter interaction which can be used for electron microscopy investigations. Figure adapted with permission from [118].

Scanning Electron Microscopy (SEM)

This section reviews limitations of SEM investigations of pristine and replicated samples as well as extracted particles. Metallographically prepared bulk specimen of microalloyed steel can be imaged with SEM for particle characterisation [3, 5–7, 63, 66, 70, 73, 79, 94] and microstructure investigation [2, 9, 16, 17, 80, 90]. While

SEM investigations provide valuable information on phases in presence and grain orientation, they only provide size distributions of limited accuracy due to sample preparation limitations. Size and shape of particles slightly protruding through specimen surface cannot be determined as precisely as in ETFs and CERs.[70, 79] Time-efficient determination of statistically meaningful PSDs is impeded by the low number of particles accurately measurable. When investigating particles smaller 10 nm in a cross section, an unavoidable matrix contribution impedes unambiguous determination of precipitate chemical composition.[6, 73]

SEM investigation of CERs allows for precipitate imaging and size determination. However the secondary electron signal provides insufficient contrast for automatic particle analysis [79], so that time-efficient PSD determination cannot be achieved via SEM of CERs. Precipitates down to 10 nm in size can be imaged according to Varano et al. [127]. EDS spot analysis allows for quantitative chemical composition estimation, but the limited count rate highlights the technical limitation of EDS spot analysis in SEM for sub-10 nm precipitates. SEM has to be seen as an alternative to higher resolution TEM for analysis of microalloyed steel CERs for research groups, or companies without access to TEM facilities.

SEM investigation of extracted precipitates is often referred to as three-dimensional investigation in the literature.[4, 6, 73, 96] Compared to the two-dimensional cross section investigations, the extracted precipitates are collected on a filter. This approach finds application in the characterisation of µm-sized precipitates.[3, 4, 6, 7, 70, 73, 96] Filter loss for precipitates in the sub-10 nm range [1, 51, 52] and the limited resolution capability of SEM compared to TEM are the reason why SEM investigation is not suited for analysis of sub-10 nm sized precipitates extracted from microalloyed steel.

Transmission Electron Microscopy (TEM)

TEM investigations can be carried out on ETFs, CERs, and extracted particles. TEM on pristine samples requires the preparation of an ETF. Imaging of the thin foil provides information upon microalloyed steel microstructure [2, 9, 13, 15, 16, 18, 39, 40, 45, 80], precipitate arrangement in the different phases [2, 13, 15–18, 33, 35, 38–40, 45, 65], precipitate size down to a few nanometres and shape [2, 8–10, 12, 13, 15–18, 22, 23, 27, 30, 34, 38–40, 45, 66, 75, 79, 80]. Chemical composition of precipitates is accessible via EDS [8, 9, 12, 15, 17, 18, 23, 66, 75] and EELS [8, 45, 80]. Precipitates in ETFs are enclosed in an iron matrix which systematically contributes to the EDS signal for precipitates the size of the electron beam or smaller.[88] The magnetism of the iron matrix is responsible for electron beam deflection which can be corrected by the operator. Selected area diffraction is used to determine crystallographic properties of the precipitates [8, 9, 15, 16, 18, 22, 23, 30, 33, 34, 39, 40, 45, 65, 66, 80] and their orientation relationship with the iron matrix [2, 8, 15, 16, 18, 22, 23, 30, 33, 34, 45, 65, 66, 80]. The collected information allows for precipitation type identification (e.g. interphase or strain-induced precipitation) [16, 18, 38, 66]. Besides precipitate characterisation, TEM investigations on thin foils enable interaction studies between precipitates and dislocations.[17, 66] Tedious sample preparation and time-consuming optimisation of TEM settings hinder an efficient precipitate analysis. Statistically meaningful precipitate characteristics are difficult to obtain from a single thin foil, since only a small area is available for analysis [79] and particle size distribution determination suffers from overlapping projections of precipitates [92]. Studies rely on

high resolution techniques such as APT to obtain more precise data on precipitate size and chemical composition [12, 13, 22, 30, 33–36, 39] or use TEM to validate APT data [26, 40].

Studying precipitates in extraction replicas allows to overcome undesired iron matrix effects. As for TEM investigations of ETFs, the investigation of CERs in TEM allows for precipitate size and shape determination.[8, 9, 11, 15, 19–21, 23, 25, 46, 48, 62, 64, 65, 69, 72, 74–76, 82] According to literature the smallest particles which can be extracted from the steel surface lie in the range from less than 1 nm to 3 nm in diameter, making TEM on extraction replicas suitable for analysis of sub-10 nm precipitates.[19, 20, 62, 64, 80] EDS and EELS measurements are usually employed for a qualitative estimation of precipitate composition [8, 9, 11, 15, 19–21, 23, 25, 46, 48, 62, 64, 65, 69, 72, 74–76, 82]. Recently EELS has been used to quantitatively determine chemical compositions of precipitates.[46, 80] Selected area diffraction can also be employed to study precipitate crystallography.[19, 20, 62, 64, 76] While the orientation relationship of precipitates to the iron matrix cannot be studied in extraction replicas, precipitate arrangement in steel can still be investigated [15, 20, 62] and precipitate volume fraction determined [19, 21]. The carbon film in CERs impedes determination of carbon content in precipitates. An alternative to CERs has been developed by Scott el al. [46] to determine precipitate carbon content and carbon to nitrogen ratios. Extraction replica preparation should be carefully executed to avoid artifacts such as undesired particle loss and particle displacement.[48, 88]

TEM investigations of extracted particles provide statistically more meaningful PSDs than TEM investigations of ETFs and CERs. The improved particle density benefits the identification of precipitate families with different chemical compositions via EDS. The suitability of the MDT for precipitate analysis was demonstrated through TEM and EDS investigations of extracted precipitates. Read et al. [53] determined the size, shape, and chemical composition of electrolytically extracted precipitates. Lu et al. [51, 64–66] extended the suitability of the MDT to chemically extracted precipitates. They also introduced the combination of MDT and TEM as a valuable complementary approach to investigations on pristine or replicated samples, by discussing metallurgical findings based on results provided by all three approaches. Hegetschweiler et al. [1, 67] used TEM investigations on chemically extracted precipitates to establish colloidal characterisation techniques for precipitate analysis.

TEM investigation of ETFs is irreplaceable to determine precipitate/matrix orientation relationships and precipitate arrangement in the steel matrix. The same holds true of TEM investigation of CERs for precipitate arrangement analysis. TEM combined with pristine, replicated or dissolved samples has to be carried out depending on the research focus. Hegetschweiler et al. [1, 52] investigated the particle loss inherent to the MDT technique and found that the amount of undesired particle etching can be neglected when comparing PSDs obtained via TEM investigations of CERs and extracted precipitates for the chemical extraction protocol presented in [52]. Sub-10 nm precipitates have successfully been extracted from microalloyed steels and accounted for in the determined PSD.[1]

Scanning Transmission Electron Microscopy (STEM)

STEM has the advantage to allow for an improved precipitate characterisation, because it allows for an enhanced resolution and for EELS point analysis and mapping.

The application of STEM for precipitate analysis in ETFs ranged from simple precipitate detection [94] to comprehensive investigation including size, shape, chemical composition and crystal structure determination [9, 25, 26, 42]. Commonly EDS point analysis [9, 26], or EDS mapping [25] has been employed to assess precipitate composition. The high precision of STEM combined with ETFs allows for detailed determination of microstructural features and precipitate distribution within the microalloyed steel.[9] Wang et al. [42] combined STEM and APT to study the formation of clusters and their evolution into precipitates. These observations were only made possible by the high-resolution STEM equipment since the precipitate chemical compositions appeared to be too similar for differentiation in APT. Neither conventional SEM, nor TEM would have provided the required imaging capabilities. CERs have been imaged in STEM to determine precipitate size [1, 49, 50, 68, 74, 79], shape [49, 68, 74], and chemical composition through EDS [68, 74] or EELS [50] with a higher precision than with TEM and SEM [79]. Further, STEM investigations on CERs allow for study of precipitation distribution in the steel microstructure with a better resolution than TEM.[68, 74] These elements are used to study precipitate evolution in a steel sample at different treatment stages [68, 74], or to compare precipitation status between different steels [50]. To the best of the author's knowledge STEM investigations on extracted precipitates have only been carried out by Hegetschweiler et al. [1, 67], to study precipitate size, shape, and chemical composition with higher accuracy and precision than TEM.

2.3.2 Analytical Ultracentrifugation (AUC)

Theodor Svedberg invented an analytical ultracentrifuge (AU) in 1924 to determine particle size distributions. He provided a fractionating characterisation technique with Ångström resolution and reliable statistics to determine particle sizes in the range 1 - 5 000 nm.[128–130] A centrifugal force is applied to the investigated colloidal system and resulting particle sedimentation is monitored to determine sedimentation coefficients containing particle size information. Temperature control is critical for a successful AUC measurement. Peltier elements in the rotor chamber maintain the desired temperature and operation under high vacuum minimises heat generating friction between the spinning rotor and the gas atoms in the rotor chamber. AUs can contain absorption, interference, schlieren, or fluorescence optics. Absorption optics contain either turbidity, or UV-Vis detectors for single-, or multi-wavelength (MWL) detection.[128, 130] Sedimentation velocity (SV), sedimentation equilibrium, synthetic boundary, density gradient, and approach to equilibrium experiments can be carried out with an AU.[130] In SV-experiments the rotor is either kept at constant speed or accelerated. The latter is referred to as gravitational sweep (GS) experiment and one has to distinguish between multi-speed GS experiments [131, 132] and speed ramp GS experiments [133]. In multi-speed GS experiments the rotor speed exhibits a stair shaped profile over time, while in speed ramp GS experiments the rotor speed is linearly increased throughout the course of the experiment.

In an AU equipped with absorption optics the AU rotor is spinning at a given speed and the AUC measurement cell crosses the optical beam path only briefly. The spectrometer scans across the sectors of the measurement cell and monitors particle sedimentation induced by rotor movement in a SV-experiment at constant speed. Because the particles sediment with a characteristic velocity, the particle size distribution of the suspension can be determined. In a speed ramp SV-experiment the spectrometer does not scan across measurement cell sections. The spectrometer is at a

fixed position (e.g. section middle) and detects particles sedimenting in the linearly increasing gravitational field when they pass the fixed spectrometer radial position. This also allows for particle size distribution determination. An AU equipped with a MWL UV-Vis detector is utilised in this thesis to analyse particles extracted from microalloyed steels. The following sections will focus on the type of experiments carried out in this thesis and the theoretical background of optical detection of sedimenting particles.

Sedimentation Velocity Experiment

Particle sedimentation speed depends on particle size, density, and shape. This leads to fractionation of the different particle populations. The extinction measured across the measurement cell (**Fig. 2.5**) allows for radial concentration profile determination. The concentration gradient corresponds to the sedimentation boundary. For each scan a sedimentation boundary is measured at t_i and its radial position r_{sb} is determined. **Eq. 2.13** links the sedimentation boundary velocity to the sedimentation coefficient and can be integrated to determine the mean sedimentation coefficient of the investigated particles (**Eq. 2.14**). The mean sedimentation coefficient can be used for data analysis of monomodal colloids.

$$v = \frac{dr_{sb}}{dt} = \frac{s}{\omega^2 \cdot r} \tag{2.13}$$

$$\ln \frac{r_{sb}}{r_m} = s \cdot \int_0^t \omega^2 dt \tag{2.14}$$

with the sedimentation boundary velocity v, the sedimentation boundary radius r_{sb}, the time t, the sedimentation coefficient s, the rotor spinning velocity ω, the radius from center of rotation r, and the meniscus position r_m.

$$g(s) = \frac{d\left(\frac{C(s)}{C_0}\right)}{ds} \cdot \left(\frac{r}{r_m}\right)^2 \tag{2.15}$$

with the sedimentation coefficient distribution $g(s)$, the sample concentration for a given sedimentation coefficient $C(s)$, the initial sample concentration C_0, the sedimentation coefficient s, the radius from center of rotation r, the meniscus position r_m.

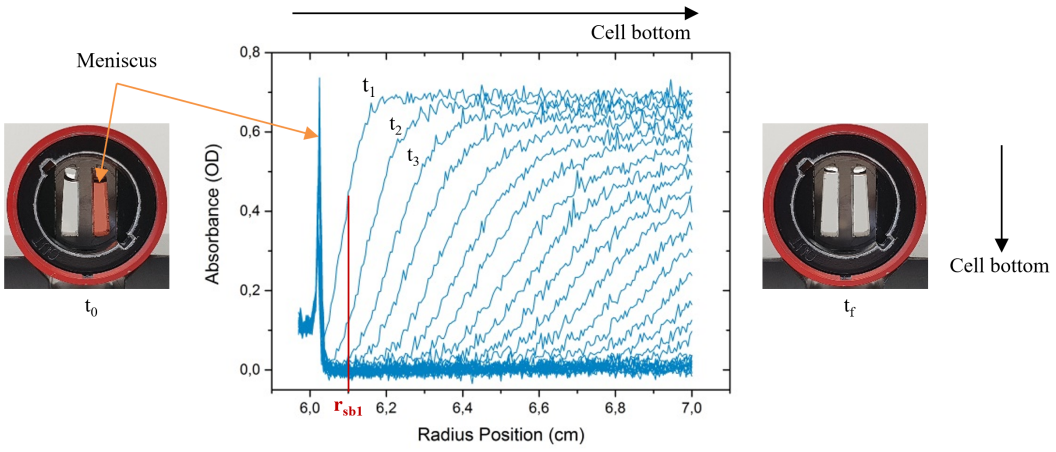

FIGURE 2.5: Change in absorbance as a function of radial position during SV-experiment.

For suspensions with broad particle size distributions or for multimodal colloids a sedimentation coefficient distribution (**Eq. 2.15**) is preferred to the mean sedimentation coefficient for accurate data analysis. Data analysis for determination of sedimentation coefficient distribution can be carried out with either parameter free approaches (time derivative method DCDT [134–137], van Holde-Weischet analysis [138]) or direct boundary modelling [139–142]. In this thesis direct non-negative least-squares (NNLS) boundary modelling (ls-g*(s)) is used in Sedfit, a freely available AUC data analysis software provided by the Schuck lab.[139, 143] The ls-g*(s) model is suitable for analysis of multimodal or broad colloidal systems containing large particles ($\varnothing > 30\,\mathrm{nm}$), because it assumes ideal, non-diffusing particles.[144] For high resolution data analysis of smaller particles either rotor speed selection allows to neglect diffusion and the ls-g*(s) model is used , or models based on the Lamm equation are employed.[140] In Spyder, a freely available python environment, the sedimentation coefficient distribution is then converted into an extinction weighted particle size distribution. This step requires particle density knowledge. The ligand shell is considered in particle density determination (**Eq. 2.16**, refer to **Appendix A** for derivation):

$$\rho_\mathrm{P} = \rho_\mathrm{Shell} + \left(\frac{x - 2 \cdot l_\mathrm{S}}{x}\right)^3 \cdot (\rho_\mathrm{Core} - \rho_\mathrm{Shell}) \tag{2.16}$$

with the particle density ρ_P, the shell density ρ_Shell, the hydrodynamic particle diameter x, the shell thickness l_S, and the particle core density ρ_Core.

The shell density equals the ligands density and the core density equals the material density. Insertion of **Eq. 2.16** into **Eq. 2.27** leads to **Eq. 2.17** (refer to **Appendix A** for derivation):

$$\frac{x^2}{18 \cdot \eta} \cdot \left(\frac{\rho_\mathrm{Shell} \cdot \left(x^3 - (x - 2 \cdot l_\mathrm{S})^3\right) + \rho_\mathrm{Core} \cdot (x - 2 \cdot l_\mathrm{S})^3}{x^3} - \rho_\mathrm{S}\right) - s = 0 \tag{2.17}$$

with the solvent viscosity η_S, the solvent density ρ_S, and the sedimentation coefficient s.

Sedimentation coefficient values are known and corresponding particle radii are determined using **Eq. 2.17**. To complete extinction weighted PSD determination, the extinction frequency distribution needs to be assessed. The extinction frequency distribution is determined via axis transformation (**Eq. 2.18**):

$$F(x) = F(s) \cdot \frac{ds}{dx} \tag{2.18}$$

with the extinction frequency distribution $F(x)$ and the sedimentation coefficient distribution $F(s)$.

The sedimentation coefficient frequency distribution $F(s)$ is provided by Sedfit. The sedimentation coefficient equation is known (**Eq. 2.17**). The particle radius depending particle density equation is known (**Eq. 2.16**). Calculation of ds/dx allows for extinction frequency distribution obtention. Combining the extinction frequency distribution and the particle radii, the extinction weighted PSD can be plotted. Before further determination of the mass and number weighted PSD, Mie correction has to be considered. Obtention of a number weighted PSD after SV-experiment is crucial

for direct comparison with TEM PSD. A number weighted TEM PSD cannot be directly compared to a sedimentation coefficient distribution, extinction weighted, or mass weighted distribution.

Concentration differences between particle populations in complex mixtures are limiting for SV-experiments at constant speed.[133] In a classical SV-experiment at constant speed certain particle populations can sediment before the rotor has reached set rotor speed and acquisition is started. Analysis of multimodal colloidal systems can be a limit of the classical SV-experiment, because a compromise rotor speed allowing for acquisition of sufficient boundaries for each population has to be identified. Implementation of a speed ramp experiment allows to circumvent the two latter limitations by gradually increasing rotor speed during acquisition.

Speed Ramp Experiment

Combination of a MWL spectrometer and a speed ramp SV-experiment allows for detailed analysis of individual components in multimodal colloidal systems and significantly reduces signal loss due to particle sedimentation prior to acquisition start. The MWL spectrometer is at a fixed radial position and measures the extinction intensity as a function of rotor speed and time. The sedimentation coefficient corresponding to given particle can be determined by **Eq. 2.19**:

$$s(t_i) = \frac{\ln \frac{r_d}{r_m}}{\int_{t_0}^{t_1} \omega^2 dt} \tag{2.19}$$

with the sedimentation coefficient at the detection time $s(t_i)$, the detector position r_d, the meniscus position r_m, and the rotor spinning velocity ω.

During data acquisition the denominator of **Eq. 2.19** is continuously calculated. Once the sedimentation coefficient distribution is determined, Mie theory and Stokes law (**Eq. 2.27**) are used to derive particle sizes and a wavelength independent particle size distribution.[133, 143] The MWL spectrometer maintains the fixed radial position set by the operator, but gravitational force stretches the rotor, leading to increasingly important differences between spectrometer and cell position. **Eq. 2.20** corrects for rotor specific stretching and the radial offset [143]:

$$r_m(t) = r_m(t_0) + K_1 \cdot f(t) + K_2 \cdot f(t)^2 \tag{2.20}$$

with the meniscus position at zero rotor speed $r_m(t_0)$ and the rotor specific stretching factors K_1 and K_2.

In this thesis data analysis was performed with a software developed by Walter named high dynamic range-multiwavelength fitting (HDR-Multifit).[133, 145] Mie correction was applied to the obtained sedimentation coefficient distributions to determine number-weighted particle size distributions.

Mathematical Theory of Particle Sedimentation

Sedimentation velocity and speed ramp experiments provide sedimentation coefficient distributions from which particle size information needs to be derived. Svedberg developed a sedimentation theory where three forces act on nanoparticles in

the AUC measurement cell during centrifugation: gravitational force (F_g), buoyant force (F_b), and frictional force (F_f) (**Eq. 2.21-2.23**): [1, 130, 143]

$$F_g = m_P \cdot \omega^2 \cdot r_P \tag{2.21}$$

$$F_b = -m_S \cdot \omega^2 \cdot r_P = -m_P \cdot \bar{v} \cdot \rho_S \cdot \omega^2 \cdot r_P \tag{2.22}$$

$$F_f = -f \cdot u \tag{2.23}$$

with the particle mass m_P, the rotor spinning velocity ω, the distance between the considered particle and the radius from center of rotation r_P, the mass of displaced solvent m_S, the partial specific volume $\bar{v}$ which equals to the inverse of particle density $1/\rho_P$, the solvent density ρ_S, the frictional coefficient f, and the sedimentation velocity of the considered particle u.

The sum of the forces applied to the particle is zero at equilibrium:

$$F_g + F_b + F_f = m_P \cdot \omega^2 \cdot r_P - m_P \cdot \bar{v} \cdot \rho_S \cdot \omega^2 \cdot r_P - f \cdot u = 0 \tag{2.24}$$

Eq. 2.25 is obtained upon rearranging of **Eq. 2.24**:

$$\frac{m_P \cdot (1 - \bar{v} \cdot \rho_S)}{f} = \frac{u}{\omega^2 \cdot r_P} \equiv s \tag{2.25}$$

Eq. 2.25 provides the definition of the sedimentation coefficient s. The sedimentation coefficient is expressed in Svedberg (S, 1 S = 10^{-13} s). The frictional coefficient equals to:

$$f = 3 \cdot \pi \cdot \eta_S \cdot x \tag{2.26}$$

with the solvent viscosity η_S and the sphere diameter x.

Combining **Eq. 2.25** and **Eq. 2.26** the sedimentation equivalent diameter can be determined (refer to **Appendix A** for the derivation):

$$x = \sqrt{\frac{18 \cdot \eta_S \cdot s}{\rho_P - \rho_S}} \tag{2.27}$$

The sedimentation equivalent diameter only equals to the hydrodynamic diameter in the case of non-solvated, hard, spherical particles with a uniform density.[1, 130, 143]

A more sophisticated sedimentation theory based on thermodynamics is provided by the Lamm equation (**Eq. 2.28**). Particle sedimentation and particle diffusion are considered, the diffusion term can be neglected for sufficiently large particles. When investigating sub-10 nm particles either a diffusion term is added or high rotor speeds are chosen to suppress diffusion. AUC measurement data analysis with the Lamm equation is suitable for narrowly distributed colloidal systems containing small particles.[1, 130, 143]

$$\frac{\partial C}{\partial t} = \underbrace{D \cdot \left(\frac{\partial^2 C}{\partial r^2} + \frac{1}{r} \cdot \frac{\partial C}{\partial r} \right)}_{\text{diffusion}} - \underbrace{\omega^2 \cdot s \cdot \left(r \cdot \frac{\partial C}{\partial r} + 2 \cdot C \right)}_{\text{sedimentation}} \tag{2.28}$$

with the sample concentration C, the time t, the sample diffusion constant D, the radius from center of rotation r, the sedimentation coefficient s, and the rotor spinning velocity ω.

Optical Particle Detection

A MWL UV-Vis Detector AU was used for particle analysis in this thesis. Detailed descriptions of MWL UV-Vis detector setup integration in preparative ultracentrifuges can be found in the literature.[146–148] The MWL UV-Vis detector AU apparatus is schematically represented in **Fig. 2.6 a**.

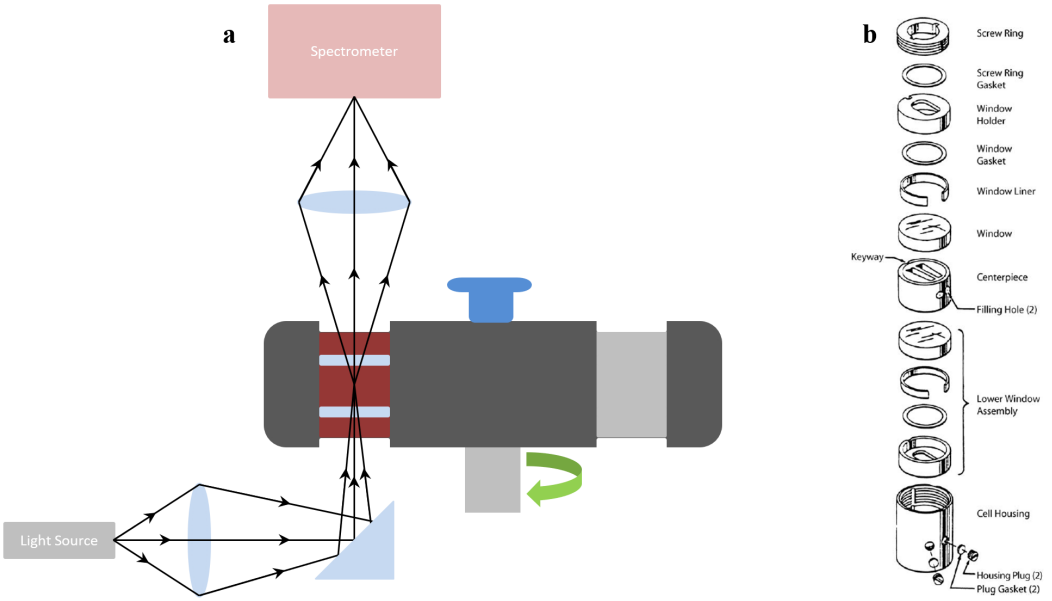

FIGURE 2.6: Schematic representation of the AUC setup.
a Optical beam path in an MWL UV-Vis detector AU.
b Double sector cell assembly (adopted with permission from [130]).

A xenon flash lamp emitting light with a wavelength from approximately 200 to 2 000 nm is employed as light source. The light is guided through the AUC measurement cell and propagates to the charge-coupled device (CCD) based MWL spectrometer.[143] Depending on the AUC experiment, several measurement cell designs are available.[130] The double section cell design adopted in this thesis is depicted in **Fig. 2.6 b**. One chamber is typically filled with the sample and the other chamber is filled with the corresponding solvent. Centerpieces with different thicknesses can be employed depending on sample volume and concentration (**Fig. 2.7**). It is preferable to measure low concentration suspensions in a cell with a thicker centerpiece to increase absorption according to Beer-Lamberts law (**Eq. 2.29**):

$$E_\lambda = \varepsilon_\lambda \cdot C \cdot l \tag{2.29}$$

with the extinction E_λ, the extinction coefficient ε_λ, the sample concentration C, and the thickness of the body crossed by light l.

The extinction, also called absorbance, measured by the MWL spectrometer is more pronounced and has a better signal to noise ratio for measurement cells with a

thicker centerpiece. Acquired signal quality is improved, which allows for enhanced precision in particle size distribution determination.

FIGURE 2.7: Double sector AUC cells with different centerpiece thicknesses.

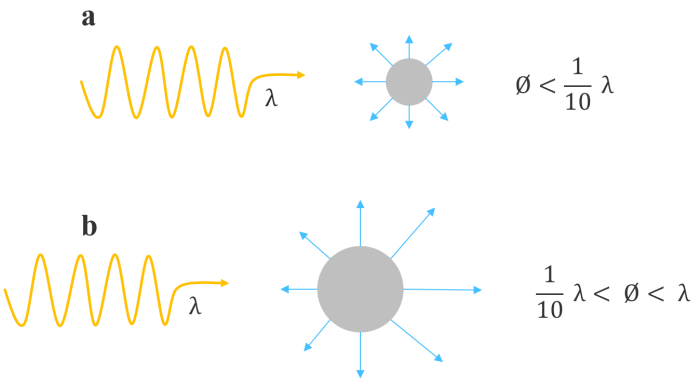

FIGURE 2.8: Representation of **a** Rayleigh scattering and **b** Mie scattering for particles of different diameters (∅).

Absorption optics measure extinction, i.e. the intensity of the scattered and absorbed light at the nanoparticles. Mie theory describes elastic light scattering at particles. The intensity of scattered light depends on the considered wavelength and particle size. The scattering behaviour of incident light depends on parameter j (**Eq. 2.30**):

$$j = 2 \cdot \pi \cdot n_{\text{solvent}} \cdot \frac{x}{\lambda} \tag{2.30}$$

with the solvent refractive index n_{solvent}, the particle diameter x, and the wavelength of the incident light λ.

For j smaller than one ($\varnothing < \lambda/10$) Rayleigh scattering occurs (**Fig. 2.8 a**). Light with different wavelengths does not scatter equally at a particle, because the scattering intensity is proportional to j^4. For j around one ($\lambda/10 < \varnothing < \lambda$) Mie scattering is observed (**Fig. 2.8 b**).[133, 149] A Mie correction is applied to remediate to the wavelength dependency of Rayleigh and Mie scattering intensity. The Mie theory is only valid for spheres, but can be extended to coated particles and ellipsoids.[150] In this thesis Mie coefficients and Mie efficiencies are determined according to the work of Mätzler [151, 152] and Bohren and Huffman [150]. Mie correction is applied to the extinction weighted PSD, to determine the mass weighted PSD and subsequently the number weighted PSD in this thesis.

Chapter 3

Experimental Methods

This chapter provides detailed information on the investigated microalloyed steel samples and procedures for sample preparation and analysis.

3.1 Microalloyed Steel Samples

The microalloyed, thermomechanically rolled steel samples used in this thesis were provided by the Aktien-Gesellschaft der Dillinger Hüttenwerke located in Dillingen/Saar, Germany. Chemical composition of the samples can be found in **Table 3.1**. Steel A and steel B were almost identical in composition and production processes. Only steel D was subjected to a two-step thermal post-processing treatment in a furnace model HT 04/17 (Nabertherm GmbH, Lilienthal, Germany) to ensure complete precipitate formation. First, steel D was heated to 1 250 °C for 30 min and then quenched in water. Second, steel D was heated to 690 °C for 60 min and then quenched in water.

	Composition wt%			
Element	**Steel A**	**Steel B**	**Steel C**	**Steel D**
C	0.04	0.04	0.06	0.04
Si	0.33	0.33	0.17	0.32
Mn	1.49	1.50	1.65	1.68
N	0.003	0.003	0.004	0.004
Al	0.04	0.03	0.03	0.03
Cu	0.25	0.25	0.23	0.22
Mo	0.01	0.01	0.01	0.02
Ni	0.27	0.27	0.23	0.23
Cr	0.03	0.03	0.03	0.05
V	0.001	0.001	0.001	0.001
Nb	0.05	0.05	0.04	0.08
Ti	0.02	0.01	0.02	0.001
Carbon Equivalent	0.33	0.33	0.37	0.36

TABLE 3.1: Composition of investigated microalloyed steels.

3.2 Electron Transparent Foil Preparation

Electron transparent foils (ETFs) were prepared in a FEI Versa 3D FIB (Thermo Fisher Scientific, Waltham, United States of America) operating in high-vacuum conditions. A 300 nm thick platinum layer was deposited on a 30 µm x 5 µm area by electron

beam (2 keV, 1.1 nA, normal incidence). Then a 2.5 µm thick platinum layer was deposited on top by gallium ion beam (30 keV, 1 nA, 52°). A microalloyed steel sample foil was prepared with the gallium ion beam (30 keV, 15 nA) and polished with the gallium ion beam at 30 keV, 1 nA and 5 kV, 77 pA to obtain an approximately 100 nm thick foil. A NanoMill Model 1040 (Fischione Instruments, Export, United States of America) was used for further foil thinning (900 eV, $\pm$ 10° incidence).

3.3 Carbon Extraction Replica Preparation

Carbon Extraction Replicas (CERs) were produced with the following procedure:

(i) The metallographic section was ground and polished to 1 µm.
Grinding steps: 1 200, 2 000, 4 000. MD-Piano grinding discs (Struers, Copenhagen, Denmark) were used.
Polishing steps: polishing to 3 µm using MD-Dac polishing cloth disc and DP-Suspension A, 3 µm (Struers, Copenhagen, Denmark). Polishing to 1 µm using MD-Nap polishing cloth disc and DP-Suspension A, 1 µm (Struers, Copenhagen, Denmark). Diamond lubricant yellow (Microdiamant AG, Lengwil, Switzerland) was used in each polishing step.

(ii) The polished metallographic section was etched. It was immersed in 2 % Nital until it became slightly matt (for 2 to 5 s). Nital solution was prepared using 65 % nitric acid (Th. Geyer GmbH & Co. KG, Höxter, Germany).

(iii) The etched metallographic section was masked with crepe tape so that only the part to be examined remained free.

(iv) The etched metallographic section was sputtered with carbon. A Cressington Carbon Coater 108carbon/A (TESCAN GmbH, Dortmund, Germany) operated in automatic evaporation and two two-stage sharpened 6.15 mm carbon electrodes were used.
Sputtering parameters: vaccuum < 10^{-2} mbar, 4.5 V, 1.8 s sputtering time per pulse, 6 to 20 pulses.

(v) The crepe tape was removed and a small grid was scratched into the C-layer with a cutter knife.

(vi) The carbon covered metallographic section was immersed in 5 % Nital. Nital solution was prepared using 65 % nitric acid. It took 10 to 90 min for the scratched replicas to detach from the section.

(vii) The detached replicas were retrieved from the Nital solution with a NS-Inox-H tweezer (Dumont, Montignez, Switzerland) and deposited onto PYSER standard TEM grids (Plano GmbH, Wetzlar, Germany).

3.4 Matrix Dissolution Technique

3.4.1 Chemical Particle Extraction

Precipitates were chemically extracted with $0.5\,\mathrm{mol}\cdot\mathrm{L}^{-1}$ sulfuric acid (95 – 97 %, Sigma-Aldrich, Germany) and 0.1 vol% Disperbyk-2012 (BYK Additives & Instruments, Wesel, Germany) according to the extraction protocol developed by Hegetschweiler et al.[1, 52] All chemicals were used as purchased without any further purification. Ultrapure water was produced in a Milli-Q water-purification system type Advantage A10 and Elix 20 (Merck Millipore, Burlington, United States of America). Undesired ionic species and Disperbyk-2012 excess were removed from the suspension by centrifugation. The suspensions were centrifuged eight times at 70 000 RPM and 20 °C for 90 min in a preparative ultracentrifuge Optima XE-90 (Beckman Coulter, Brea, United States of America). The fixed-angle titanium rotor type 70 Ti (Beckman Coulter, Brea, United States of America) was used in combination with 32.4 mL OptiSeal polypropylene tubes (P/N 361625, Beckman Coulter, Brea, United States of America) and the appropriate Spacers (P/N 361669, Beckman Coulter, Brea, United States of America). After the first seven centrifugation runs the removed supernatant was replaced with Milli-Q water after having redispersed the residue by sonication in a Sonorex Super RK 514 BH (BANDELIN electronic GmbH & Co. KG, Berlin, Germany) ultrasonic bath for 5 min.

3.4.2 Electrolytic Particle Extraction

The electrolytic cell setup depicted in **Fig. 3.1** was connected to a Potentiostat/Galvanostat Model 273A Princeton Applied Research (Ametek Inc., Berwyn, United States of America) which was used as potentiostat and operated with the PowerSuite software version 2.50.0 (Ametek Inc., Berwyn, United States of America). Technical drawings of the electrodes and electrode plugs can be found in **Appendix B**. The electrolytic setup was mounted on a RCT basic magnetic stirrer (IKA, Staufen im Breisgau, Germany) to increase ionic species mobility. A LiCl saturated (in ethanol), Ag/AgCl reference electrode with double-junction system (P/N 6.0726.100, Metrohm, Herisau, Switzerland) was used to monitor applied potential and ensure it was nominal. To determine applied potential the experiment needed to be interrupted. Cell enable was switched to off and the PowerSuite operating software closed. Then the Ag/AgCl electrode was wired as reference electrode and immersed in the electrolyte, the platinum wire (former reference electrode) was wired as working electrode and the platinum counterelectrode remained wired as counterelectrode. The buttons local and then measure only were pressed on the potentiostat prior to switching cell enable on. The applied potential was displayed by the potentiostat.

The microalloyed steel working electrode was ground and cleaned after manufacturing. Grounding was carried out with plain backed CarbiMet silicon carbide grinding papers (P 240 > P 400 > P 1 200 > P 2 500) (Buehler, Lake Bluff, United States of America). After grinding the working electrode was immersed in acetone and sonicated for 10 min in a Sonorex Super RK 514 BH (BANDELIN electronic GmbH & Co. KG, Berlin, Germany) ultrasonic bath. In a second cleaning step the working electrode was then rinsed with ethanol, immersed in ethanol and sonicated for another 10 min in the same ultrasonic bath.

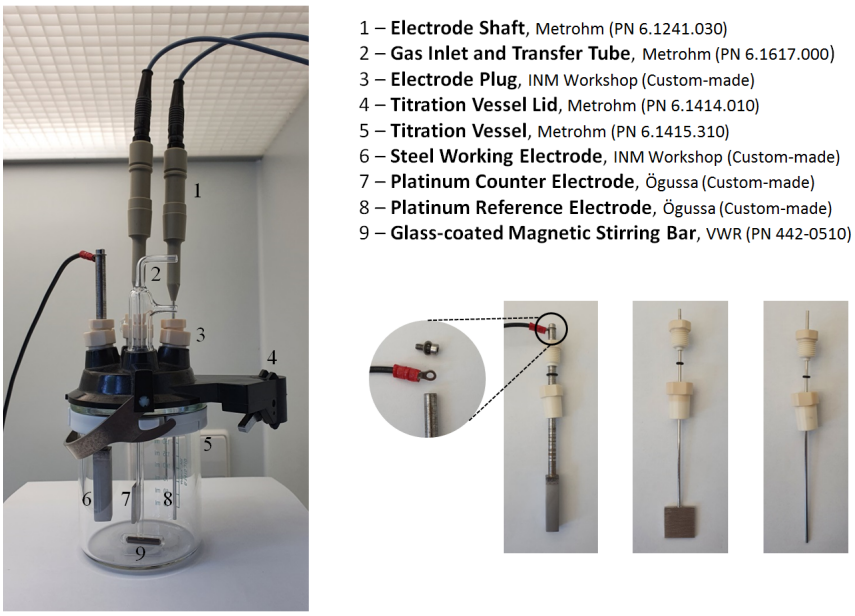

FIGURE 3.1: Components used in electrolytic cell setup assembly.

The electrolytes were freshly prepared. All chemicals were used as purchased without any further purification. The electrolyte components were weighed with a Practum precision scale (Sartorius AG, Göttingen, Germany). The filled titration vessel was closed with its lid. Argon was then flushed through the cell via the gas inlet and transfer tube with a flow of 1.5 NL/h for 20 min under magnetic stirring at level 4 to homogenise the electrolyte and remove oxygen. The gas inlet and transfer tube was connected to a bubbler to enable pressure release. The electrodes were then immersed in the electrolyte to the same depth, the argon flow was set to 0.5 NL/h, and the magnetic stirrer motion to level 8. Electrolysis was carried out using the *chronoamperometry one step* template in PowerSuite to maintain a constant potential over time. The working electrode was declared as a solid electrode of defined area and the reference electrode as unspecified. The features *measure open circuit potential as required* and *override auto intensity conditioning* were selected.

After electrolysis the electrolytic cell was disconnected from the potentiotstat and sonicated for 15 min in a Sonorex Super RK 514 BH (BANDELIN electronic GmbH & Co. KG, Berlin, Germany) ultrasonic bath. Undesired ionic species were removed from the suspension by centrifugation. The suspensions were centrifuged ten times at 32 000 RPM and 20 °C for 120 min in a preparative ultracentrifuge Optima XE-90 (Beckman Coulter, Brea, United States of America). The swinging-bucket rotor SW 32 Ti (Beckman Coulter, Brea, United States of America) was used in combination with 30 mL polyallomer tubes (P/N 253060, Herolab GmbH, Wiesloch, Germany). After the first nine centrifugation runs the removed supernatant was replaced with ethanol after having redispersed the residue by sonication in an ultrasonic bath for 5 min. The total mass of dissolved steel was determined by weighing the working electrode before and after electrolysis with a Practum precision scale (Sartorius AG, Göttingen, Germany). Electrolytic cell components were thoroughly cleaned with ethanol in between experiments.

Chemical	CASRN	Manufacturer	Product Number
Methanol	67-56-1	Sigma-Aldrich	32213-M
TMAC	75-57-0	Carl Roth	4747.1
Acetylacetone	123-54-6	Sigma-Aldrich	P7754-A
Methyl Salicylate	119-36-8	Sigma-Aldrich	M6752
Salicylic Acid	69-72-7	Carl Roth	2723.1
SDS	151-21-3	Sigma-Aldrich	L4390
Maleic Acid	110-16-7	Sigma-Aldrich	63180
Maleic Anhydride	168-31-6	Sigma-Aldrich	63200-F
Disperbyk-180	n/a	BYK	105621
TEGO Dispers 662 C	n/a	Evonik	n/a

TABLE 3.2: Chemicals for electrolytic extraction.

3.4.3 Silica Nanoparticle Synthesis

The synthesised silica nanoparticles were added to the electrolyte to attempt a controlled SiO_x-network formation. All chemicals were used as purchased without any further purification. Ultrapure water was produced in a Milli-Q water-purification system type Advantage A10 and Elix 20 (Merck Millipore, Burlington, United States of America). Silica nanoparticles were synthesised according to Hartlen et al. [153]. 91.0 mg of L-arginine (0.52 mmol) were weighted in a 250 mL two-neck flask. Upon addition of 69.005 g of Milli-Q water the solution was homogenised. Addition of 4.5 mL cyclohexane to the Milli-Q water/L-arginine solution was followed by flask installation in a multisynthesis apparatus (Carousel 6 Plus Reaction Station P/N RR99916, Radleys, Saffron Walden, United Kingdom). The mixture was stirred at 150 RPM with a Teflon coated stirring bar and heated up to 60 °C. Once the temperature of 60 °C was reached, 5.5 mL TEOS (24.82 mmol) was added to the two-neck flask. The reaction mixture was then kept at constant temperature (60 °C), constant stirring (150 RPM) for 20 h.

Chemical	CASRN	Manufacturer	Product Number
L-Arginine	74-79-3	Sigma-Aldrich	A5006
Cyclohexane	110-82-7	Carl Roth	KK41.1
TEOS	78-10-4	Sigma-Aldrich	86578
Methanol	67-56-1	Sigma-Aldrich	32213-M

TABLE 3.3: Chemicals for silica nanoparticle synthesis.

After 20 h the particle suspension was separated from the cyclohexane phase using a separatory funnel. Dialysis against 4 L of Milli-Q water was carried out to clean the silica particle suspension with a regenerated cellulose dialysis membrane (P/N 5104.1, Carl Roth GmbH & Co. KG, Karlsruhe, Germany). Milli-Q water was exchanged after 1 h, 2 h, 4 h, 12 h. Finally the suspension was filtered using a 0.22 µm polyethersulfon filter (P/N P821.1, Carl Roth GmbH & Co. KG, Karlsruhe, Germany).

Dialysis of silica particles in water against methanol was performed using a regenerated cellulose dialysis membrane (P/N 5104.1, Carl Roth GmbH & Co. KG, Karlsruhe, Germany) to achieve a stable silica particle suspension in methanol. 11 mL of silica particles in Milli-Q water were dialysed against 500 mL of methanol. Methanol was changed after 5 h 30 min, 3 h 45 min, 13 h 15 min. Silica particles dispersed in

methanol rather than in Milli-Q were used because they were added to a methanol-based electrolyte.

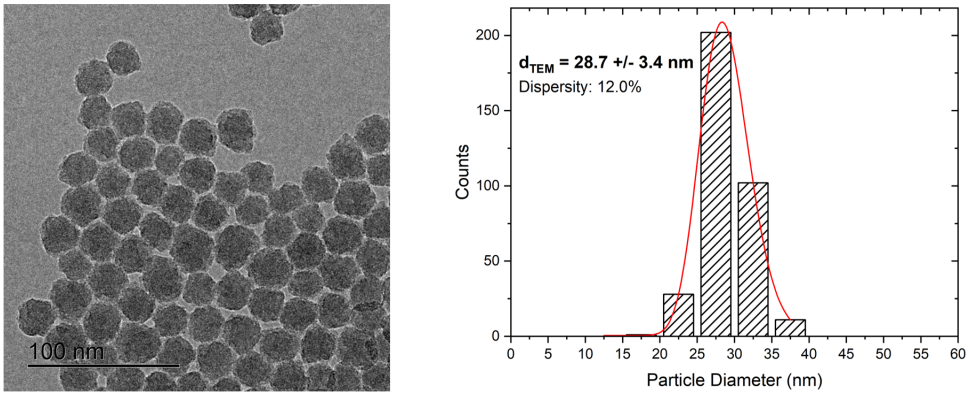

FIGURE 3.2: Silica nanoparticle diameter determination via TEM.

The synthesised silica nanoparticles were characterised via TEM, DLS and ICP-OES. Synthesised nanoparticles were imaged with a JEM-2100(HR) TEM (JEOL, Akishima, Japan) equipped with a lanthanum hexaboride (LaB_6) electron source and an Orius Model SC1000 camera (Gatan Inc., Pleasanton, United States of America). Particle size distribution determination was carried out with Fiji. DLS and zeta-potential measurements were carried out with a Zetasizer Nano ZSP (Malvern Instruments Ltd., Worcestershire, United Kingdom) and DLS data analysis was performed with the general purpose algorithm.

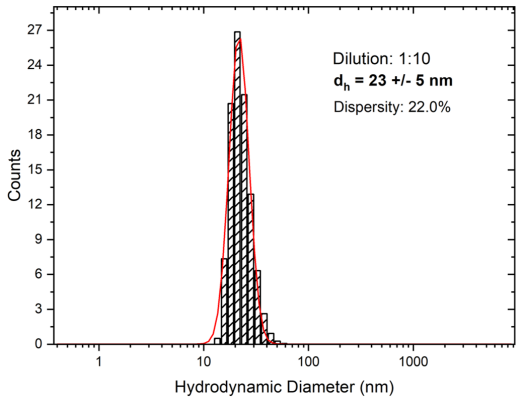

FIGURE 3.3: Silica nanoparticle diameter determination via DLS.

	Temp.	**Zeta Potential**	**Elec. Mob.**	**Cond.**
Unit	°C	mV	$\mu m \cdot cm \cdot V^{-1} \cdot s^{-1}$	$mS \cdot cm^{-1}$
Measurement 1	25	-21.7	-1.7	0.154
Measurement 2	25	-20.2	-1.587	0.154
Measurement 3	25	-19.5	-1.531	0.155
Average	-	-20.47	-1.606	0.154
Standard Deviation	-	1.12	0.086	0.001

TABLE 3.4: Zeta Potential measurements of silica nanoparticles in Milli-Q water.

ICP-OES characterisation of the synthesised silica nanoparticles was carried out with a Jobin Yvon Ultima2 instrument (Horiba, Kyoto, Japan) equipped with a Conikal

nebulizer (PerkinElmer Inc., Waltham, United States of America). The flow rate was set to 0.69 $L \cdot min^{-1}$. The pressure was set to 2.74 bar. The suspension was diluted (1:1 000) prior to characterisation. A Si content of 1 002 $\pm$ 11 $mg \cdot L^{-1}$ was measured.

3.5 Fractionation of Extracted Particles

Fractionation was carried out in a preparative ultracentrifuge Optima XE-90 (Beckman Coulter, Brea, United States of America). The swinging-bucket rotor SW 60 Ti (Beckman Coulter, Brea, United States of America) was used in combination with 4.4 mL polyallomer tubes (P/N 328874, Beckman Coulter, Brea, United States of America). For each fractionation experiment 2 mL of the suspension containing the chemically extracted precipitates were filled into one tube. After centrifugation the supernatant was removed up to the ring marking at the bottom of the tube. The residue was sonicated in a Sonorex Super RK 514 BH (BANDELIN electronic GmbH & Co. KG, Berlin, Germany) ultrasonic bath for 20 min. Up-concentration of the supernatant was achieved by filling the supernatant in a 4.4 mL polyallomer tube (P/N 328874, Beckman Coulter, Brea, United States of America), adding Milli-Q water to prevent tube collapse and centrifugation at 483 750 RCF for 4 h and 20 °C. The supernatant obtained after the up-concentration centrifuge run was discarded and the residue redispersed in a Sonorex Super RK 514 BH (BANDELIN electronic GmbH & Co. KG, Berlin, Germany) ultrasonic bath for 10 min to obtain a sub-10 nm particle suspension of higher concentration.

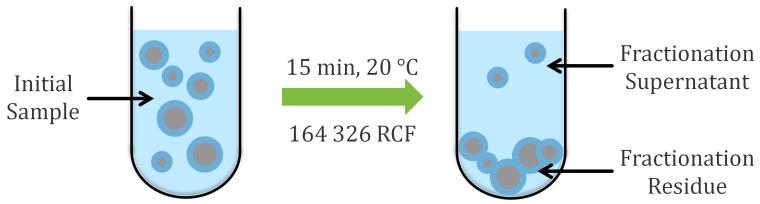

FIGURE 3.4: Schematic representation of the differential centrifugation fractionation.

3.6 Particle Characterisation

3.6.1 Analytical Ultracentrifugation (AUC)

A preparative ultracentrifuge model Optima XL-80K (Beckman Coulter, Brea, United States of America) was modified into a MWL-AU following a design of the open AUC project.[145, 148] An An-60 Ti analytical 4-place titanium rotor (P/N 361964, Beckman Coulter, Brea, United States of America) was used. In the course of this thesis the AU that only allowed for SV experiments at constant speed (SV-AUC) was modified to also allow for SR SV-experiments (SR-AUC). HEX files provided by Johannes Walter (Friedrich-Alexander University Erlangen-Nuremberg) were written with the programmer laqiya tl866 II Plus (Shenzhen Laqi Ya Technology Co., Shenzhen, China) onto blank SST 27SF512 EEPROMs. The original Beckman Coulter EEPROMs on the control and cathode-ray tube board were then replaced with the newly programmed EEPROMs.

AUC measurement cells with sapphire windows and 12 and 20 mm titanium centerpieces (P/N 801-12, P/N 801-20) were purchased from Nanolytics Instruments

GmbH (Potsdam, Germany). Screw ring gaskets (P/N 362328), window gaskets (P/N 327021), window liners (P/N 362329), gaskets for double-sector centerpieces (P/N 330446) and plug gaskets (P/N 327022) were purchased from Beckman Coulter (Brea, United States of America). A counterbalance with weights (P/N 360219) was purchased from Beckman Coulter (Brea, United States of America) and used for both the 12 and 20 mm measurement cells. A torque stand assembly (P/N 361318, Beckman Coulter, Brea, United States of America) was used to close the measurement cells. If measurement cell centerpiece length is not specified the standard 12 mm centerpieces were used.

The AU was controlled with a Labview (version 19.0) user interface provided by Johannes Walter. Measurement parameters are listed in **Fig. 3.5**. For SV experiments at constant speed all parameters were kept constant for measurements of distinct samples, except for the rotor speed and the number of scans which were adapted to each sample. For SR SV-experiments listed parameters were used for all investigated samples.

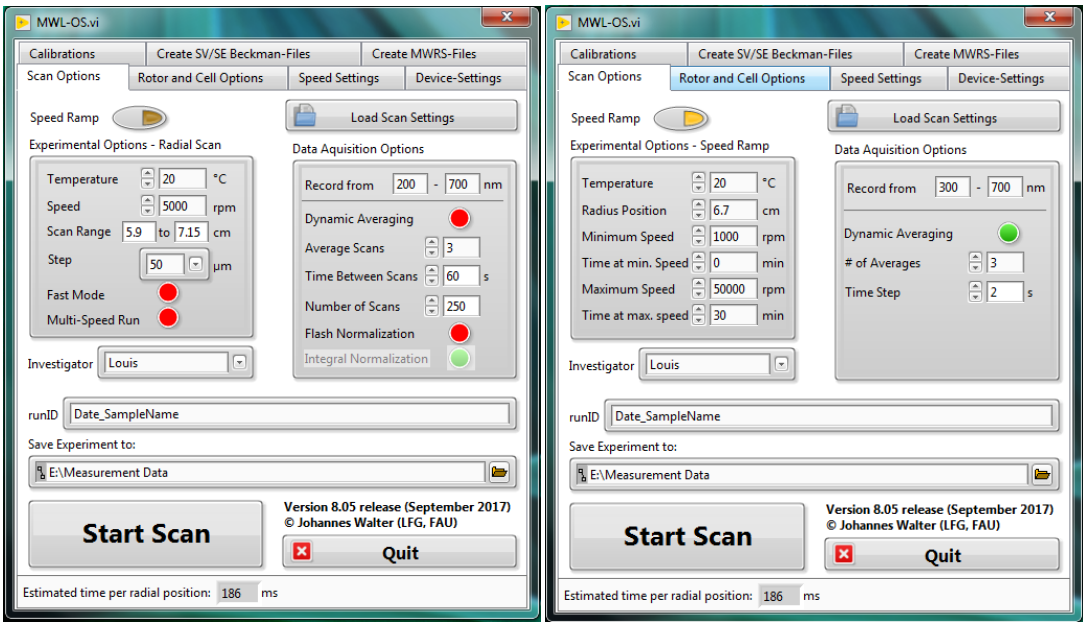

(A) SV-AUC (B) SR-AUC

FIGURE 3.5: AUC parameters for SV-experiments at constant speed (SV-AUC) and SR SV-experiments (SR-AUC).

Data analysis was carried out with Sedfit version 15.01b for SV experiments at constant speed (SV-AUC) and with HDR-Multifit [133, 145] version 1.32g for SR SV-experiments (SR-AUC) prior to number weighted PSD determination in Spyder (version 3.2.6), a freely available python environment. In Sedfit sedimentation coefficient distributions were obtained by using the ls-g*(s) model at 450 nm. Resolution was set to 100 and confidence level to 0.95. The values for s_{min} and s_{max} were adapted to the investigated suspensions. Both the relative intensity noise and time independent noise were fitted. Obtained sedimentation coefficient distributions were imported to Spyder for determination of extinction, mass and number weighted particle size distributions using a Mie correction based on work of Mätzler [151, 152] and Bohren and Huffman [150]. In HDR-Multifit analysis was carried out with a minimum signal count of 500. Standard analysis was selected, analyte density and

analyte refractive index were entered and a direct boundary analysis was carried out. Apparent sedimentation coefficient distributions at 450 nm obtained by selecting the apparent distribution analysis method (moving average and Savitzky-Golay filters set to 20) were imported to Spyder for determination of extinction, mass and number weighted particle size distributions using a Mie correction based on work of Mätzler [151, 152] and Bohren and Huffman [150]. The following parameters were adapted to the investigated sample in Spyder:

- Solvent density, dynamic viscosity and refractive index.
- Particle core material density and complex refractive index.
- Measurement cell centerpiece length (12 or 20 mm).

The density of Milli-Q was set to $998\,\mathrm{kg \cdot m^{-3}}$, the dynamic viscosity was set to $0.001\,002\,\mathrm{kg \cdot m^{-1} \cdot s^{-1}}$ and the refractive index to 1.33. The density of ethanol was set to $789\,\mathrm{kg \cdot m^{-3}}$, the dynamic viscosity to $0.001\,26\,\mathrm{kg \cdot m^{-1} \cdot s^{-1}}$ and the refractive index to 1.42.

Particles in the initial suspensions and residues were considered to be on average equivalent to TiNb(CN) particles in terms of density and optical properties. The particle core material density was set to $6\,655\,\mathrm{kg \cdot m^{-3}}$ and complex refractive index to 1.72 + 1.55 i in the following sections where initial suspensions and/or residues were investigated: 4.1.4, 4.2.2, 4.2.3, 4.3.1. These density and refractive index values are required for NWPSD and correspond to TiNb(CN) properties. TiNb(CN) density was determined by performing the arithmetic mean of TiN, TiC, NbN and NbC densities. The complex refractive index for TiNb(CN) at 450 nm was adopted from Hegetschweiler.[1]

Sub-10 nm particles were thought to be niobium rich with negligible amounts of titanium. Particle core material density was set to $8\,145\,\mathrm{kg \cdot m^{-3}}$ and complex refractive index to 2.07 + 2.25 i in the following sections when investigating supernatants: 4.3.1. These values correspond to Nb(CN) properties. Nb(CN) density was determined by performing the arithmetic mean of NbN and NbC densities. Complex refractive index for Nb(CN) at 450 nm was adopted from Hegetschweiler.[1] For AUC investigations in section 4.4 the particle core material density was set to $7\,820\,\mathrm{kg \cdot m^{-3}}$ and the complex refractive index to 2.07 + 2.25 i.

The thickness of the Disperbyk-2012 ligand shell was set to 5.737 2 nm, the Disperbyk-2012 density to $1\,056\,\mathrm{kg \cdot m^{-3}}$.[1] Analysis was carried out at 450 nm, because this wavelength allows good detection of both niobium and titanium carbides and nitrides without undesired contribution from the dispersing agent.[1] Provided size distributions correspond to particle core distributions, because the ligand shell was accounted for in the data evaluation process.

AU calibration ensured beam straightness between the prism and the spectrometer, optimal step motor position and optimised spectrum intensity. AU angular and radial calibration files were generated. Calibration was validated by measuring the following samples in SV experiments at constant speed:

- $1\,\mathrm{mg \cdot mL^{-1}}$ bovine serum albumine (P/N A7030, Sigma-Aldrich, St. Louis, United States of America) in $25\,\mathrm{mmol \cdot L^{-1}}$ sodium chloride (P/N 71380-M, Sigma-Aldrich) at 40 kRPM.

- 30 nm diameter gold nanospheres (NanoXact - bare, nanoComposix, San Diego, United States of America) diluted 1:1 in Milli-Q at 3 kRPM.
- 81 nm diameter polystyrene beads (P/N 3080A, Thermo Fisher Scientific, Waltham, United States of America) diluted 1:20 in Milli-Q at 10 kRPM.

AUC Characterisation of Reference Gold Nanoparticles

NanoXact gold nanospheres - bare (citrate) with diameters of 5, 10, and 30 nm were purchased from nanoComposix (San Diego, United States of America). Suspensions were provided at 0.05 mg $\cdot$ mL^{-1} in 2 mmol $\cdot$ L^{-1} sodium citrate solution. 5, 10, and 30 nm diameter gold nanoparticle suspensions were diluted 1:1 with Milli-Q and characterised separately via SV-AUC. A mixture of the gold particles was prepared and characterised via SV-AUC and SR-AUC. To prepare the gold nanoparticle mixture 500 µL of each gold nanoparticle suspension was put in a vial and the 1 500 µL of gold nanoparticle mixture was diluted with 1 500 µL of Milli-Q. All AUC measurements were carried out with measurement cells containing a 12 mm centerpiece. SV-AUC measurements were carried out at a rotor speed of 3 kRPM for the 10 nm gold nanoparticle suspension, 30 nm gold nanoparticle suspension and gold nanoparticle mixture. SV-AUC measurement of the 5 nm gold nanoparticle suspension was carried out at 10 kRPM. The number of scans was set to 150 for the 5 nm gold nanoparticle suspension, to 300 for the 10 nm gold nanoparticle suspension, to 30 for the 30 nm gold nanoparticle suspension and 2 700 for the gold nanoparticle mixture. Solvent density was set to 998 kg $\cdot$ m^{-3}, solvent viscosity to 0.001 002 kg $\cdot$ m^{-1} $\cdot$ s^{-1}, solvent refractive index to 1.33, particle density to 19 300 kg $\cdot$ m^{-3}, particle refractive index to 1.6998 + 1.9732 i for analysis at 529 nm.

3.6.2 Atom Probe Tomography (APT)

Specimens were analysed via APT in a LEAP 3000XHR (Cameca SAS, Gennevilliers, France). Prior to analysis the specimens were exposed to ultra-high vacuum (1.33×10^{-8} Pa) and cooled down to 60 K. To achieve single atom field-evaporation a direct current voltage ramp was implemented to reach up to 11 kV. Once the threshold for single atom field-evaporation was reached, ionized atoms were evaporated in a controlled manner by voltage pulsing (200 kHz, 15 % of the direct current voltage). Direct current voltage adaptation ensured a detection rate of 3 ions per 1 000 pulses. Detected ions were analysed with the software package IVAS 3.6.14 (Cameca SAS, Gennevilliers, France). Crystallographic pieces of information provided by the detector hit map were used to reconstruct atoms into the 3D space. Particles (precipitates and/or clusters) in the investigated APT specimens were identified via 1 at% niobium isoconcentration surface and via cluster analysis using the following parameters:

- Minimum number of atoms defining a cluster set to 4.
- Maximum distance between two atoms belonging to the same cluster (D_{max}) set to 2.
- Number of atoms of niobium which must be within a sphere of diameter equal to D_{max} to form a cluster set to 4.

Specimens for APT analysis were prepared as follows. First, the steel sample was ground with plain backed CarbiMet silicon carbide grinding papers (P 240 > P 400

> P 1 200) (Buehler, Lake Bluff, United States of America). Then the sample was polished with MD-Dac polishing cloth discs and corresponding DP-Suspension A (6 µm > 3 µm > 1 µm) (Struers, Copenhagen, Denmark). Lastly the steel D sample was oxide polished (MasterMet, Buehler, Lake Bluff, United States of America). Locations on the polished steel D sample surface were randomly selected for specimen preparation in a Helios Nanolab^{TM} 600 (Thermo Fisher Scientific, Waltham, United States of America) according to the standard FIB lift-out technique [154].

3.6.3 Dynamic Light Scattering (DLS)

PSDs were determined using a Zetasizer Nano ZSP (Malvern Instruments Ltd., Worcestershire, United Kingdom). The samples were sonicated for 5 min in a Sonorex Super RK 514 BH (BANDELIN electronic GmbH & Co. KG, Berlin, Germany) ultrasonic bath before being filled in disposable cuvettes and measured at a temperature of 25 °C in backscatter mode (173°) with a laser of wavelength 633 nm. The equilibration time was set to 120 s and three measurements with eleven runs each (delay between measurements set to 30 s) were carried out. The data presented in this thesis corresponds to the average of the three measurements. Acquired data was analysed using the Zetasizer Software version 7.11. Non-negative least squares fitting was used to determine PSDs. Only the intensity weighted PSDs are presented in this thesis since volume and number weighted PSDs are prone to transformation artefacts. This is mainly due to the unknown optical properties of the extracted particles.

Species	Refractive Index	Extinction Coefficient
TiN	1.3512	2.7599
TiC	3.0787	2.6950
Nb	2.2736	3.2820
Ti(CN)	2.2149	2.7274
TiNb(CN)	2.2443	3.0047

TABLE 3.5: Estimated optical properties of extracted particles at $\lambda =$ 633 nm required for DLS analysis.

The refractive index and absorption values (**Table 3.5**) were estimated as follows. The refractive index and absorption for TiN, TiC, Nb were provided by an online data-base (https://refractiveindex.info/, reference viewed on 27/05/2021). No values were found for NbC, NbN, TiNb(CN), which were estimated using the values found for TiN, TiC, Nb. The mean of the values for TiN and TiC was used as estimate for the optical properties of Ti(CN). The mean of Nb and Ti(CN) was used for TiNb(CN).

3.6.4 Electron Microscopy (TEM, STEM)

A JEM-2100(HR) TEM (JEOL, Akishima, Japan) with a lanthanum hexaboride (LaB_6) electron source was operated at an acceleration voltage of 200 kV and 0.14 nm resolution in the bright field imaging for analysis of extracted particles. An Orius Model SC1000 camera (Gatan Inc., Pleasanton, United States of America) was used for precipitate imaging. EDS point analysis was carried out with a Noran System 7 X-ray Microanalysis system (Thermo Fisher Scientific, Waltham, United States of America). A JEM-ARM200F STEM (JEOL, Akishima, Japan) equipped with a cold field emission gun, a STEM probe corrector (CESCOR) and a JED-2300 Analysis Station

EDS system (JEOL, Akishima, Japan) was used at 200 kV for characterisation of extracted particles and particles contained in ETFs. Fiji (version 1.51w) and Digital Micrograph (version 3.22.1461.0) software were utilised to process acquired TEM and STEM micrographs. Particle size was assessed by measuring the particle area and determining an equivalent circle diameter. EDS point analysis was used to determine average particle chemical composition.

3 µL of a suspension containing extracted particles were deposited onto a carbon coated copper grid (P/N S160, Plano GmbH, Wetzlar, Germany) held by a tweezer (P/N 0202-N0C-PO, Dumont, Montignez, Switzerland) for TEM and STEM analysis of extracted particles. Solvent evaporation took place at room temperature under a vertical stream, clean room ISO 4 flowbox (bc-technology GmbH, Frickenhausen, Germany). Alternative specimen preparation used copper grids with a holy carbon film (P/N S147-2, Plano GmbH, Wetzlar, Germany).

3 µL of a suspension containing extracted particles were deposited on a copper grid with holy carbon film for cryo-TEM specimen preparation. 2 s suspension stamping on the grid allowed for removal of excess suspension. A Gatan CP3 cryoplunger (Gatan Inc., Pleasanton, United States of America) was then used to immerse the grid in liquid ethane ($-165\,^{\circ}\mathrm{C}$). A precooled Gatan 914 cryo-TEM holder (Gatan Inc., Pleasanton, United States of America) was used for imaging of the specimen at low dose in a JEM-2100(HR) TEM (JEOL, Akishima, Japan) at $-170\,^{\circ}\mathrm{C}$ and 200 kV.

Automated CER STEM analysis was carried out in a field emission scanning electron microscope type Merlin equipped with a Gemini II column (Carl Zeiss SMT Inc., Thornwood, United States of America) operated at 20 kV/ 2 nA in the oriented dark field mode. Prior to analysis the SEM chamber experienced a 30 min plasma cleaning with built in CER. Automated analysis was carried out at 50 000x magnification with GenPart, Genesis software (EDAX In., Mahwah, United States of America). Micrographs were acquired at $2\,048 \times 1\,600$ pixel resolution. Prior to analysis grey levels of 0-120 and 135-255 were selected for precipitate identification and analysis. Brightness and contrast are adjusted to ensure the grey levels 120-135 correspond to the matrix. Minimum precipitate size was set to 5 nm and maximum precipitate size to 1 753 nm. Precipitates smaller 5 nm can still be detected due to technical pixel considerations. For each precipitate 90 % of its surface was analysed via EDS for 10 s. For each CER 16 stubs with 4×4 fields each were analysed. Field size was set to $0.002 \times 0.002\,\mathrm{mm}^2$ and field spacing to 0.2 µm. A maximum precipitate limit of 100 per field was set.

NanoXact gold nanospheres - bare (citrate) with diameters of 5, 10, and 30 nm were purchased from nanoComposix (San Diego, United States of America). Suspensions were provided at $0.05\,\mathrm{mg} \cdot \mathrm{mL}^{-1}$ in $2\,\mathrm{mmol} \cdot \mathrm{L}^{-1}$ sodium citrate solution. Gold nanoparticle mixtures were prepared as described in the AUC characterisation section of reference gold nanoparticles and used as reference colloidal system for suitability determination of automated STEM analysis in the sub-10 nm particle diameter range.

3.6.5 Inductively Coupled Plasma Optical Emission Spectroscopy (ICP-OES)

Elemental analysis of suspensions was carried out using a Jobin Yvon Ultima 2 instrument (Horiba, Kyoto, Japan) equipped with a Conikal nebulizer (PerkinElmer Inc., Waltham, United States of America). The flow rate was set to $0.66\,\mathrm{L}\cdot\mathrm{min}^{-1}$. The pressure was set to values in the range of 2.6 and 2.7 bar. The suspensions were either measured undiluted, or diluted (1:10, 1:5) prior to measuring. No particle digestion was carried out.

Elemental analysis of pristine microalloyed steel chippings was carried out using a Jobin Yvon Ultima2 instrument (Horiba, Kyoto, Japan) equipped with a PEEK MiraMist nebulizer (PerkinElmer Inc., Waltham, United States of America). The flow rate was set to $0.71\,\mathrm{L}\cdot\mathrm{min}^{-1}$ and the pressure to 3.0 bar.

Chapter 4

Results & Discussion

This chapter presents findings on sample preparation for analysis of particles with sub-10 nm diameters. Electrolytic extraction was tested with several methanol based electrolytes to reduce undesired particle etching compared to chemical extraction. The extracted particles were analysed via the fractionating characterisation technique AUC. The smallest chemically extracted particles were isolated via differential centrifugation fractionation prior to analysis for resolution enhancement in the sub-10 nm diameter range. Analysis of the fractions provided size and chemical composition information of particles with diameters below 10 nm. Finally, a technique based on AUC analysis of chemically extracted particles and ICP-OES analysis of steel chippings was implemented and combined with APT for precipitate number density determination in microalloyed steels.

4.1 Electrolytic Extraction of Sub-10 nm Particles

Hegetschweiler et al. [1, 52] quantified TiNb(CN) particle loss for several etching solutions and developed a novel chemical extraction procedure minimising undesired particle etching and allowing for sub-10 nm particle extraction. This thesis aims at implementing electrolytic extraction to further reduce undesired particle loss in the sub-10 nm diameter range. Electrolytic extraction allows for selective dissolution of the matrix at potentials which are largely not affecting the more noble precipitates.[64–66] The undesired particle loss inherent to the matrix dissolution technique can therefore be reduced by electrolytic extraction. Undesired particle etching is therefore reduced in the case of electrolytic extraction [66, 95, 155]. Extracted precipitates are less altered than in chemical extraction and correspond more to the precipitates contained in the pristine microalloyed steel sample.

Non-aqueous electrolytes have been used in recent studies to extract precipitates from microalloyed steels.[6, 54, 66, 69, 95, 97] Aqueous electrolytes containing acids do not have the same potential as non-aqueous electrolytes to reduce undesired particle etching. In this thesis only non-aqueous methanol based electrolytes with a TMAC supporting electrolyte and a complexing agent were used. **Table 4.1** lists the different complexing agents tested. This section discusses the suitability of the different electrolytes reported in literature for precipitate extraction from microalloyed steels to provide a suspension allowing for AUC characterisation. TEM was used to assess successful particle extraction and to resolve undesired features of the obtained suspensions such as pronounced SiO_x-network formation, or steel fragments prior to potential AUC measurements. Such undesired features are detected in AUC measurements and can be mistaken for extracted particles. Finding undesired features in the suspensions impedes AUC characterisation, because no quantification of the contribution of undesired features to the PSD of extracted particles is available.

It cannot be excluded that AUC measurements of suspensions containing extracted particles, steel needles/fragments and SiO_x microparticles lead to distorted PSDs.

Sources	Complexing Agents
[6, 54, 64–66, 69, 72, 73, 94–96]	Acetylacetone
[54, 94, 97]	Methyl Salicylate / Salicylic Acid
[69]	Maleic Acid
[54, 94]	Maleic Anhydride

TABLE 4.1: Complexing agents of the electrolytes evaluated for obtention of suspensions suitable for colloidal analysis.

According to literature the electrolyte using acetylacetone as complexing agent allows for TiNb(CN) particle extraction [54, 64–66, 69, 72, 95]. Particle shape, size, morphology and chemical composition are commonly investigated via electron microscopy/EDS [6, 66, 69, 73, 95], XRD [64–66, 69], spectrometry [72, 95] after electrolytic extraction using the acetylacetone electrolyte. To the best of the author's knowledge only the work of Zimmermann [95] combined TiNb(CN) particle extraction using the acetylacetone electrolyte and colloidal characterisation techniques (DLS, FFF) to determine particle size distributions. The following section will study the suitability of the acetylacetone electrolyte for particle extraction and subsequent characterisation via AUC.

4.1.1 Acetylacetone Electrolyte

The acetylacetone electrolyte used in this thesis was methanol based and contained 10 wt% acetylacetone and 1 wt% TMAC. Electrolytic extractions were carried out with steel B (refer to **Table 3.1** for microalloyed steel composition) at three different potential values (**Table 4.2**) to investigate the interconnection between suspension quality, applied potential and amount of dissolved steel. The lower limit of applicable potentials was determined according to potentiodynamic curves.[66, 155]

Exp. n°	**Potential vs Ag/AgCl** (mV)	**Time** (h)	**Dissolved Sample** (mg)
1	500	5	158.0
2	300	5	70.4
3	100	5	41.5

TABLE 4.2: 10 wt% acetylacetone, 1 wt% TMAC, methanol.

To achieve a high sample throughput it was desirable to extract as many particles as possible per unit of time. An increase in applied potential increased the quantity of dissolved steel per unit time and of extracted particles if other extraction parameters were kept constant (**Table 4.2**). The upper limit of applicable potentials was determined by undesired particle loss considerations. The applied potential should not exceed 500 mV vs SCE to prevent undesired etching of Ti(C), Nb(C) particles.[66, 155] The investigated electrolyte composition and a potential of 500 mV correspond to the state of the art for electrolytic precipitate extraction from microalloyed steels. This knowledge is used as starting point for electrolysis and followed by extractions at lower potentials to study the interrelation between applied potential and suspension quality.

Extraction at 500 mV

TEM investigation of the suspension obtained after experiment n°1 revealed the presence of micrometer large steel needles/fragments according to EDS point analysis (**Fig. 4.1**). The TiNb(CN) particles appeared to be enclosed in the steel fragments. Discrete particles etched free from the microalloyed steel matrix could not be detected. The presence of steel fragments was assumed to originate from harsh etching. The potential at the upper-limit of the potential range regarded as acceptable [66] leads to aggressive steel sample etching and steel fragments/needles in the final suspension. To investigate this hypothesis the surface of the working electrode after electrolytic extraction was imaged via environmental SEM and compared to micrographs before extraction to ensure visible features originate from the electrolytic extraction and not from sample preparation (**Fig. 4.2**). Micrographs of the working electrode surface after experiment n°1 revealed smoothly etched regions with a relatively flat topography and regions with a rough topography containing sharp edges. Because the working electrode surface before electrolytic extraction did not exhibit aforementioned features it was concluded that the applied potential of 500 mV is responsible for steel fragment formation through harsh etching. Lowering the applied potential could prevent harsh sample etching responsible for steel fragment/needle obtainment in the suspension.

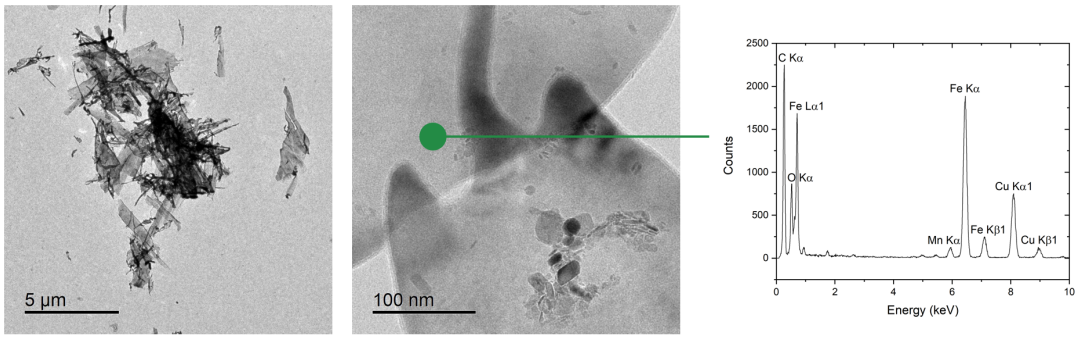

FIGURE 4.1: Identification of steel needles/fragments in the suspension obtained after experiment n°1 in TEM via EDS point analysis.

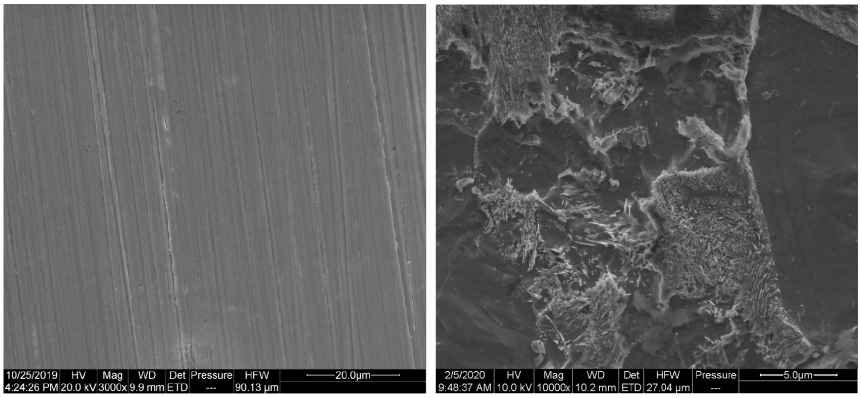

(A) Surface before electrolytic extraction (B) Surface after experiment n°1

FIGURE 4.2: Steel working electrode etching investigation via environmental SEM.

TEM investigation of the suspension obtained after experiment n°1 also revealed the presence of SiO_x microparticles with diameters ranging from several hundred

nanometres to micrometers (**Fig. 4.3**). While the SiO_x-network formation for chemical extraction using acids has been widely reported in the literature [1, 51, 52, 64, 65] it has not been mentioned so far for electrolytic extraction using the acetylacetone electrolyte [51, 64, 114]. SiO_x network/microparticle formation was observed in experiment n°1, but had not been mentioned in literature for the acetylacetone electrolyte possibly due to the different chemical compositions of the investigated microalloyed steel samples. Experiments n°2, and n°3 at lower potential values will allow to determine if the SiO_x network/microparticle formation depends only upon chemical composition of the investigated microalloyed steel samples or if the applied potential also plays a role. Steel needles/fragments and SiO_x microparticles identified via TEM in the suspension, combined with the lack of extracted discrete particles did not allow for AUC characterisation of the suspension obtained for experiment n°1.

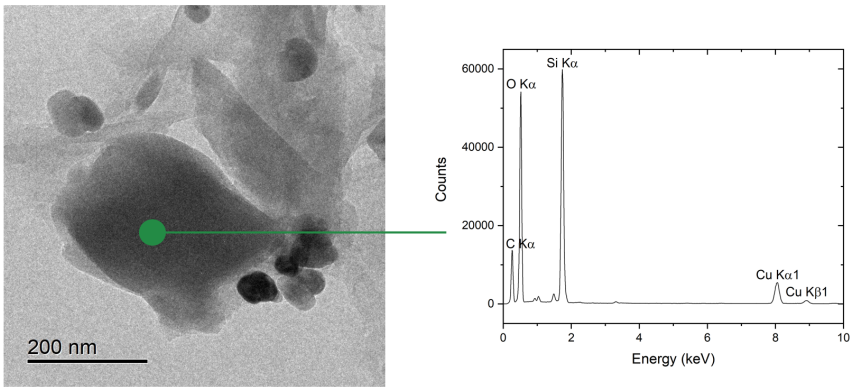

FIGURE 4.3: TEM micrograph and EDS point analysis of a SiO_x microparticle in the suspension obtained after experiment n°1.

Extraction at 300 mV

Potential reduction did not reduce steel needles/fragments in the suspension (**Fig. 4.4**). SEM investigation of the working electrode surface after electrolytic extraction revealed a reduced number of rough topography regions compared to experiment n°1 (**Fig. 4.5**) thus indicating a more uniform microalloyed steel sample dissolution.

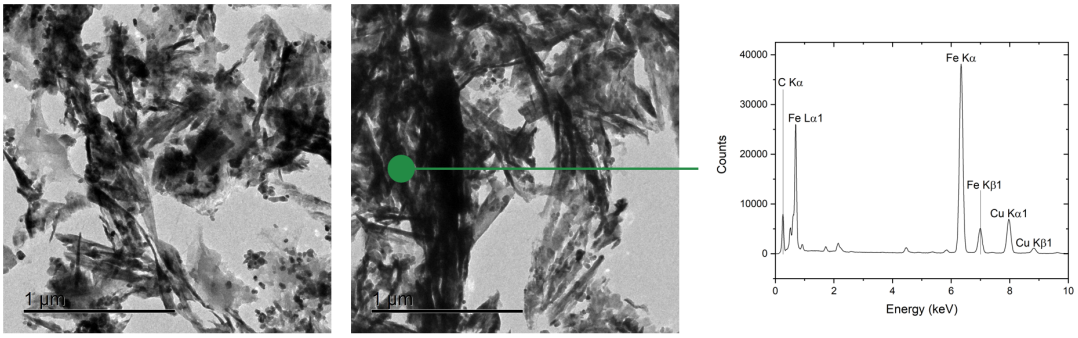

FIGURE 4.4: TEM micrographs and EDS point analysis of steel needles/fragments in the suspension obtained after experiment n°2.

TEM investigation of the obtained suspension revealed a SiO_x-network engulfing extracted particles (**Fig. 4.6**). This network was found to occasionally form SiO_x microparticles with a dimension of several 100 nm. Compared to the suspension obtained after experiment n°1 fewer and smaller SiO_x microparticles were visible. The

extent to which SiO_x network/microparticles form is related to the applied potential. It appears to also be related to the chemical composition of the investigated steel upon comparison with published data [51, 64, 114], since it can be observed also for a decreased applied potential in this thesis. AUC characterisation was not carried out for the suspension obtained after experiment n°2, because of the detrimental presence of steel needles/fragments and of a pronounced SiO_x-network.

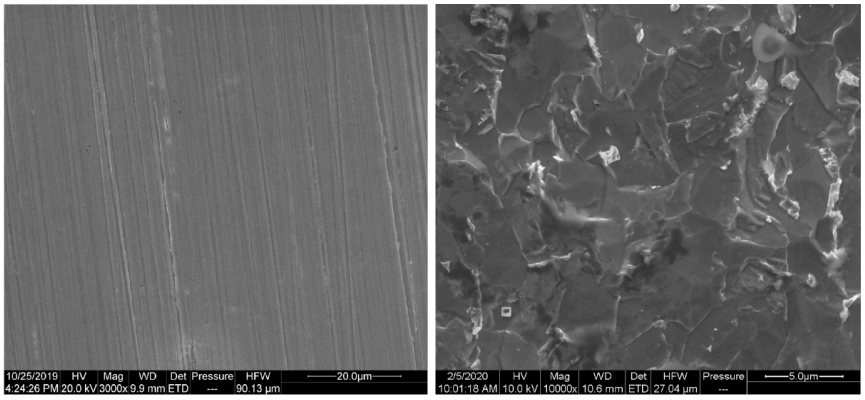

(A) Surface before electrolytic extraction (B) Surface after experiment n°2

FIGURE 4.5: Etching harshness investigation on steel working electrode via environmental SEM.

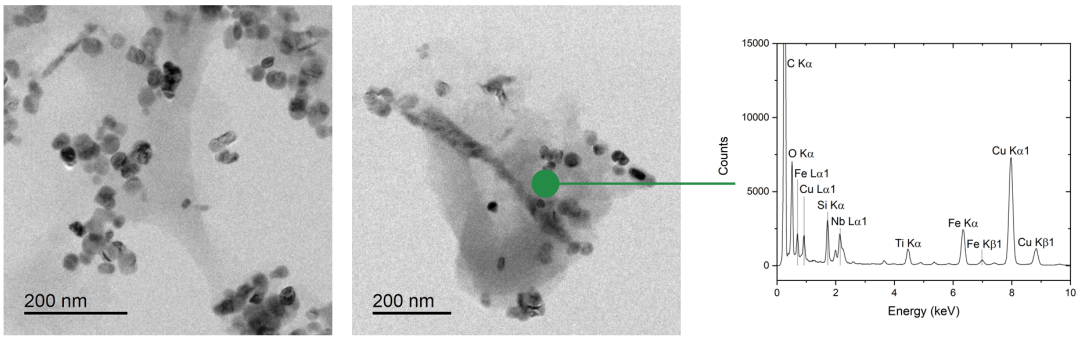

FIGURE 4.6: SiO_x-network identification in the suspension obtained after experiment n°2 in TEM via EDS point analysis.

Extraction at 100 mV

A further reduction in applied potential did not reduce steel needle/ fragment formation. The steel needles/fragments (**1**) visible in **Fig. 4.7** were also present in the suspension obtained after experiment n°3. A qualitative analysis of TEM micrographs of the suspension obtained after experiment n°3 suggests reduced number of steel needles/fragments compared to experiment n°2. Further applied potential reductions could therefore lead to limited steel needle/fragment formation, but would come at the cost of dissolving extremely small amounts of sample material which is deemed detrimental to the application intended in this thesis. The applied potential reduction from 300 to 100 mV did not reduce SiO_x-network and SiO_x microparticle formation. Discrete particles etched free from the microalloyed steel matrix were not detected. A SiO_x-network (**2**) similar to the one observable in the suspension obtained after experiment n°2 is visible in **Fig. 4.7**. Despite an applied potential reduction SiO_x microparticles (**3**) were found in the suspension obtained after experiment n°3 (**Fig. 4.7**). In light of the observed SiO_x-networks and SiO_x microparticles

over the range of suitable potentials it appeared that the microalloyed steel sample's chemical composition plays a major role in the SiO_x-network and SiO_x microparticle formation process. Applied potential plays a minor role in this formation process, because significant changes were only observed when reducing the applied potential from 500 to 300 mV The presence of steel needles/fragments, SiO_x-network and SiO_x microparticles did not allow for AUC characterisation of the suspension obtained after experiment n°3.

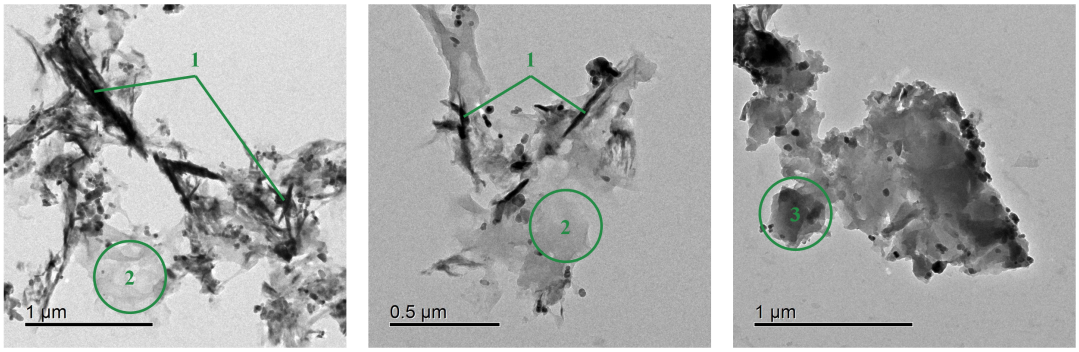

FIGURE 4.7: TEM micrographs of steel needles/fragments, SiO_x-network and SiO_x microparticles in the suspension obtained after experiment n°3.

The presence of steel needles/fragments, SiO_x-network, and SiO_x microparticles in all three suspensions obtained after electrolytic extraction at potentials in the range used for the acetylacetone electrolyte in literature [66, 155] indicates that the acetylacetone electrolyte is not suitable for extraction of TiNb(CN) nanoparticles from steel B. Literature [54, 64–66, 69, 72, 95] does not mention these undesired features. Lu [66] and Rivas et al. [69] present TEM micrographs with a SiO_x-network engulfing extracted particles without a discussion despite an EDS spectrum revealing the presence of silicon and oxygen [66]. Only Zimmermann [95] addressed the possibility of obtaining undesired features in the suspension. The chemical composition of steel B used for electrolytic extraction in this section differs in several elements from the chemical compositions of steels used in the literature [6, 64–66, 69, 72, 73, 95]. Matrix dissolution may thus differ from steel samples used in the literature. The suitability of electrolytes for electrolytic particle extraction can be classified depending on the particle types to extract [54, 94], or the types of steel investigated [69]. The classification according to steel types and compositions [69] confirms that the chemical composition of the investigated steel can greatly impact the electrolytic extraction process and the quality of the obtained suspension.

The acetylacetone electrolyte was used for Ti(CN), Nb(CN) particle extraction from steels displaying a broad range of chemical compositions in the literature.[54, 64–66, 69, 72, 95] Electrolytic particle extraction with the acetylacetone electrolyte for steel B did not lead to a suspension of desired quality in this thesis. The presence of steel needles/fragments, SiO_x-network and SiO_x microparticles in the suspension did not allow for AUC characterisation. To achieve a suspension without the aforementioned undesired features other electrolyte compositions were tested.

4.1.2 Methyl Salicylate / Salicylic Acid Electrolyte

Mizukami et al. [97] presented a methanol based electrolyte composed of 3 wt% methyl salicylate, 1 wt% salicylic acid, 1 wt% TMAC, and 0.05 wt% Sodium Dodecyl Sulfate (SDS) as alternative to the 10 wt% acetylacetone electrolyte. Methyl salicylate and salicylic acid both act as complexing agents and SDS as particle stabilising surfactant. No mention was made of the precipitate types that can be extracted with this specific electrolyte composition, but the authors used a colloidal characterisation technique (FFF) to determine the size distribution of extracted particles. Colloidal analysis of extracted particles requires a suspension free of aforementioned undesired features. Therefore the electrolyte composition presented by Mizukami et al. [97] was tested for TiNb(CN) particle extraction from steel A (refer to **Table 3.1** for microalloyed steel composition). The extraction was carried out at 500 mV vs Ag/AgCl for 7 h with the methanol based electrolyte presented by Mizukami et al. [97]. 251.1 mg of steel A were dissolved in the course of the extraction.

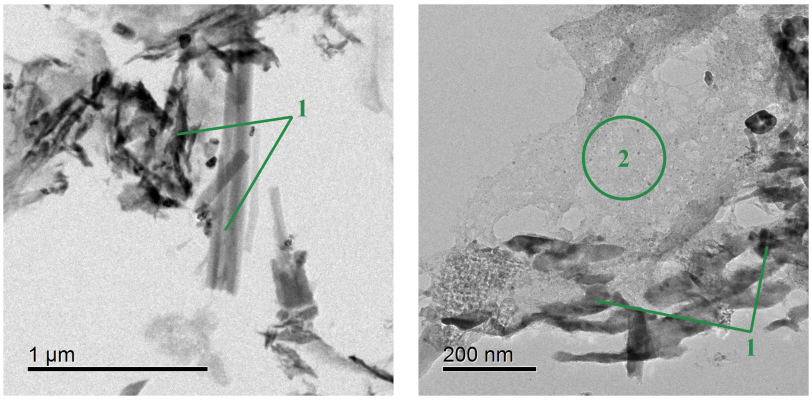

FIGURE 4.8: TEM micrographs of (**1**) steel needles/fragments, (**2**) SiO_x-network in the suspension obtained after electrolytic extraction with the electrolyte presented by Mizukami et al. [97].

TEM investigation of the suspension obtained after electrolytic extraction revealed the presence of steel needles/fragments (**1** in **Fig. 4.8**) and a pronounced SiO_x-network (**2** in **Fig. 4.8**). The observed features are similar to the ones observed in the suspension obtained by electrolytic extraction with the acetylacetone electrolyte and do not allow for AUC characterisation. No further attempt to circumvent the presence of steel needles/fragments in the suspension by potential reduction was undertaken for the electrolyte presented by Mizukami et al. [97].

Electrolytic particle extraction from steel A at 500 mV with the electrolyte presented by Mizukami et al. [97] did not provide a suspension suitable for AUC characterisation. According to findings presented for the acetylacetone electrolyte, it seems unlikely that the presence of steel needles/fragments and SiO_x-network in the suspension can be reduced by potential reduction. Instead of attempting process optimisation for the electrolyte presented by Mizukami et al. [97] for steel A, other electrolyte compositions were tested.

4.1.3 Maleic Acid Electrolyte

The maleic acid electrolyte listed by Rivas et al. [69] as suitable electrolyte for carbide particle extraction from steels containing 0.006 8 wt% C, 0.038 wt% Al, 0.026 wt% Ti or 0.082 wt% Ti was tested. Steel B has titanium and aluminium contents which are

similar to the values presented by Rivas et al. [69] (**Table 3.1**). Despite a significantly higher carbon content of steel B the maleic acid electrolyte was tested for electrolytic extraction of TiNb(CN) particles at 100 mV vs Ag/AgCl for 5 h with a methanol based electrolyte containing 10 wt% maleic acid and 2 wt% TMAC. 215.9 mg of steel B were dissolved in the course of the extraction.

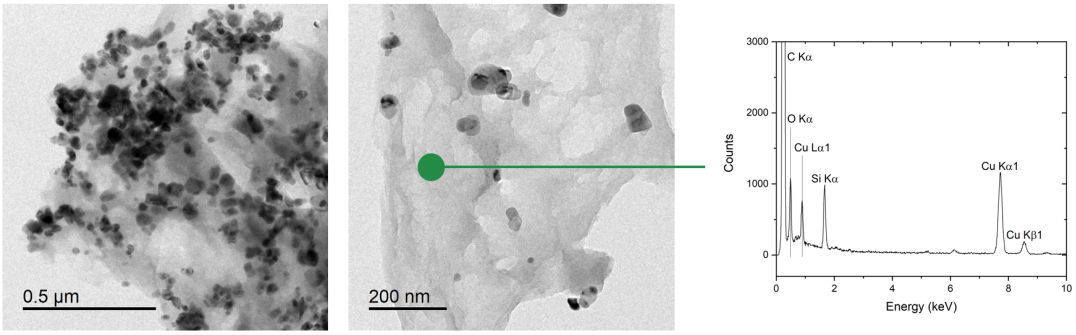

FIGURE 4.9: TEM micrographs and EDS point analysis of SiO_x-network engulfing particles extracted with the maleic acid electrolyte.

TEM investigation of extracted particles did not reveal steel needles or fragments in the suspension. This does not prove absence of these undesired features in the obtained suspension, but indicates that they may be more scarcely present in suspension compared to previously tested electrolytes. This finding is a significant step forward in suitable electrolyte identification. TEM investigation revealed a pronounced SiO_x-network engulfing extracted particles (**Fig. 4.9**). SiO_x microparticles with dimensions of several hundred nanometres were detected via TEM/EDS (**Fig. 4.10**). The maleic acid electrolyte did not allow to overcome the problematic formation of SiO_x-network and SiO_x microparticles.

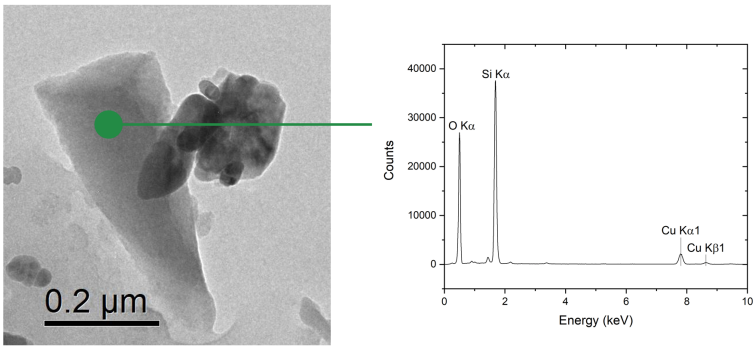

FIGURE 4.10: TEM micrograph and EDS point analysis of a SiO_x microparticle in the suspension obtained after electrolytic extraction with the maleic acid electrolyte.

4.1.4 Maleic Anhydride Electrolyte

Maleic anhydride was tested as an alternate complexing agent in the maleic acid electrolyte for precipitate extraction from steel B. Oxide inclusions such as TiO_2, $TiAl_2O_3$, ZrO_2 have been successfully extracted electrolytically from steel samples with a maleic anhydride electrolyte according to literature [54]. The maleic anhydride electrolyte mentioned in the literature is methanol based and composed of 40 wt% maleic anhydride and 3 wt% TMAC.[94] Using the maleic acid electrolyte

already allowed to drastically reduce the presence of steel needles/fragments in the suspension according to TEM. By substituting maleic acid with maleic anhydride the goal of maintaining the low level of steel needles/fragments in the suspension while improving upon SiO_x-network and SiO_x microparticle formation was pursued.

Potential Variation

The methanol based maleic anhydride electrolyte composed of 10 wt% maleic anhydride and 2 wt% TMAC was used for particle extraction from steel B at three different potential values (**Table 4.3**). Neither steel needles/fragments, nor SiO_x microparticles could be detected in TEM investigations for the suspensions obtained after the electrolytic extractions at the three different potentials (at the limited statistics of TEM). Particles extracted with the maleic anhydride electrolyte appear suitable for AUC analysis.

Exp. n°	**Potential vs Ag/AgCl** (mV)	**Time** (h)	**Dissolved Sample** (mg)
1	500	7	510.8
2	300	5	259.0
3	100	5	184.0

TABLE 4.3: 10 wt% maleic anhydride, 2 wt% TMAC, methanol.

The suspension obtained after extraction at 100 mV was analysed via speed ramp (SR) AUC, which allows to sediment all particles in suspension by gradually increasing rotor speed. If a suspension contains extracted particles, steel needles/fragments, and SiO_x microparticles, all three populations will sediment. The resulting number weighted PSD plotted in **Fig. 4.11** displays a broad peak ranging from approximately 20 to 200 nm which appears to contain three particle populations.

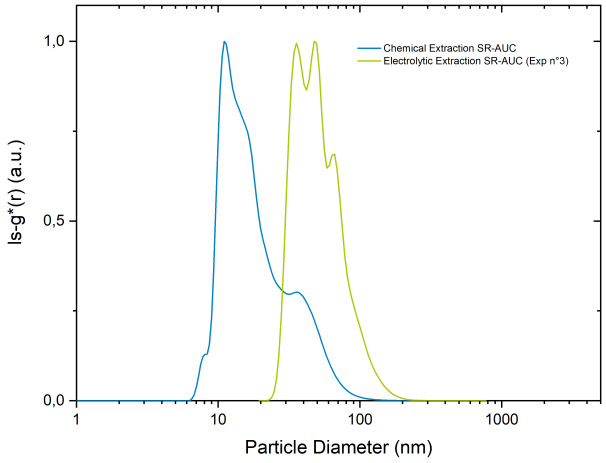

FIGURE 4.11: Number weighted PSDs for particles chemically extracted from steel A and electrolytically extracted from steel B.

Extinction has to occur at the wavelength selected for AUC data analysis for each population to be detected. AUC data analysis was carried out at 450 nm, a value that stems from optical property considerations of Ti(CN) and Nb(CN).[1] The extent to which steel needles/fragments and SiO_x microparticles contribute to the extinction signal composed of light scattering and absorption at 450 nm cannot be quantified due to missing size information. Possibly they contribute, together with extracted particles, to the acquired data. In AUC data analysis the sedimentation coefficient

distribution is converted in a number weighted PSD. This conversion requires to assume the density and refractive index of the investigated material. Depending on the size, density and optical properties of the steel needles/fragments, and SiO_x microparticles the three aforementioned populations may merge to a single population in the number weighted PSD graph. SR-AUC does not allow to exclude presence of steel needles/fragments and SiO_x microparticles in suspension, because it is unclear to which extent these undesired populations are detected in SR-AUC. A contribution of steel needles/fragments and SiO_x microparticles to the presented number weighted PSD of extracted particles is thought to be unlikely, because it requires a combination of significant extinction at 450 nm and appropriate size of the steel needles/fragments and SiO_x microparticles.

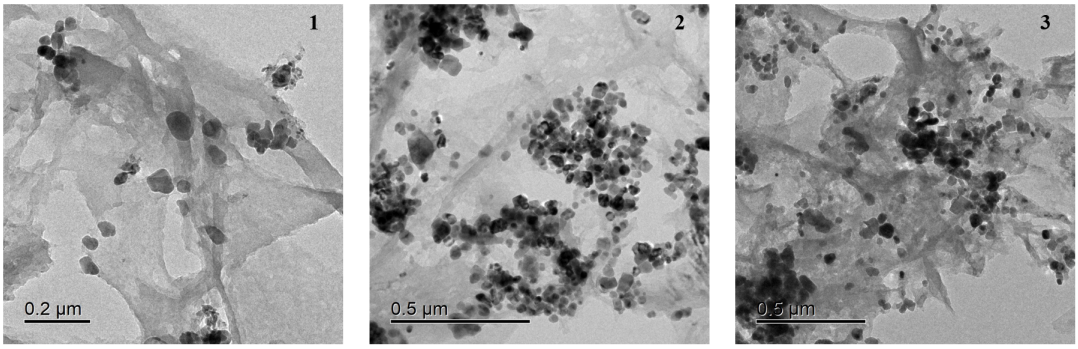

FIGURE 4.12: TEM micrographs after particle extraction at (**1**) 500 mV, (**2**) 300 mV, (**3**) 100 mV vs Ag/AgCl with the maleic anhydride electrolyte.

Comparison of the number weighted PSDs determined via SR-AUC for the electrolytically and chemically extracted particles reveals a pronounced shift towards higher particle diameters for the electrolytically extracted particles (**Fig. 4.11**). The PSD for chemically extracted particles is regarded as benchmark, because the chemical particle extraction has been validated in previous works [1, 52, 67] and is validated in this thesis by a number weighted PSD determined via STEM analysis of CER. The electrolytically extracted particles could appear larger than the chemically extracted particles because of particle agglomeration and/or a particle engulfing SiO_x-network. Detection of steel needles/fragments and SiO_x microparticles in addition to extracted particles in the AUC would result in a PSD starting at a similar particle diameter value than the PSD of chemically extracted particles and broadening towards larger particle diameters. The PSD for the electrolytically extracted particles in **Fig. 4.11** displays a shift in the sub-20 nm range compared to the PSD for chemically extracted particles. This indicates that steel needles/fragments and SiO_x microparticles cannot be responsible for the shift alone and that particle agglomeration and/or a particle engulfing SiO_x-network are most likely responsible for the PSD shift. The overall contribution of potentially present steel needles/fragments and SiO_x microparticles to the number weighted PSD appears to be negligible compared to the contribution of particle agglomeration and/or a particle engulfing SiO_x-network.

The maleic anhydride electrolyte is the first electrolyte tested in this thesis for which neither steel needles/fragments, nor SiO_x microparticles could unambiguously be detected. It appears that the presence of these undesired features depends primarily

upon electrolyte composition and more precisely upon complexing agent choice. Extraction parameters such as applied potential could well play a subordinate role in the formation of steel needles/fragments and SiO**x** microparticles. These undesired features represent electrolyte composition and extraction parameter related hurdles that can be overcome by appropriate electrolyte selection. In this thesis maleic anhydride electrolyte appeared to be suitable to avoid them. The pronounced SiO_x-network and extracted particle agglomeration observed for all maleic anhydride cases (**Fig. 4.12**) was similar to all other electrolytic extractions. The formation of a SiO_x-network in the course of the extraction appears to be inherent to the electrolytic extraction process. Extracted particle agglomeration appears to be another process-inherent problem.

Dispersing Agents

Commercial dispersing agents were added to the maleic anhydride electrolyte to attempt particle stabilisation and SiO_x-network formation reduction. A commercial dispersing agent has been successfully used in the chemical extraction process to reduce particle agglomeration and SiO_x-network formation.[52] Disperbyk-180 by Byk (Altana Group) and TEGO Dispers 662 C by Evonik were recommended by the respective manufacturer and added in quantities comprised in the recommended addition level range. 10 mg of Disperbyk-180 were added to the maleic anhydride electrolyte in experiment n°4. 4.05 g of TEGO Dispers 662 C were added to the maleic anhydride electrolyte in experiment n°5 (**Table 4.4**).

Exp. n°	**Potential vs Ag/AgCl** (mV)	**Time** (h)	**Dissolved Sample** (mg)
4	100	5	236.0
5	100	5	256.2

TABLE 4.4: 10 wt% maleic anhydride, 2 wt% TMAC, methanol with addition of commercial dispersing agents.

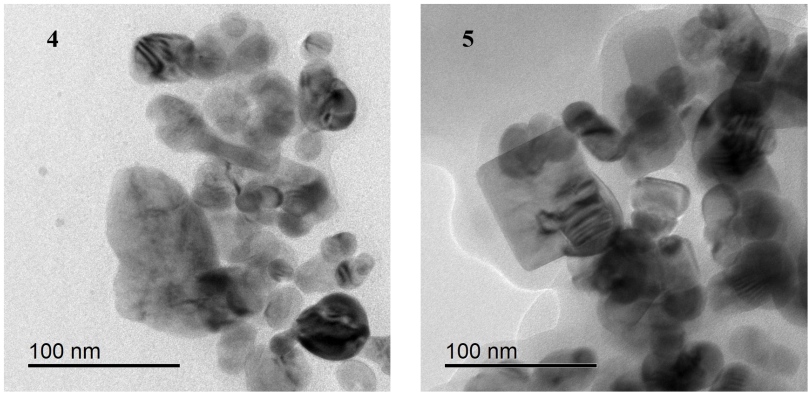

FIGURE 4.13: TEM micrographs of extracted particles after (**4**) experiment n°4 and (**5**) experiment n°5.

TEM investigation of the suspensions obtained after experiment n°4 and experiment n°5 reveals organic residues which are thought to originate from the used dispersing agents. The presence of a SiO_x-network hidden by the organic residues cannot be excluded. Few SiO_x microparticles were detected via TEM in suspensions provided by experiment n°4 and experiment n°5. For both experiments the obtained suspension presented agglomerated extracted particles (**Fig. 4.13**). To exclude the possibility that the TEM detected particle agglomeration originates from a suspension drying

effect on the TEM grid SR-AUC measurements were carried out. Number weighted PSDs for experiment n°4 and experiment n°5 did not greatly differ from the number weighted PSD for experiment n°3 (**Fig. 4.14**), suggesting that Dispberyk-180 and TEGO Dispers 662 C additions did not reduce particle agglomeration and SiO_x-network formation.

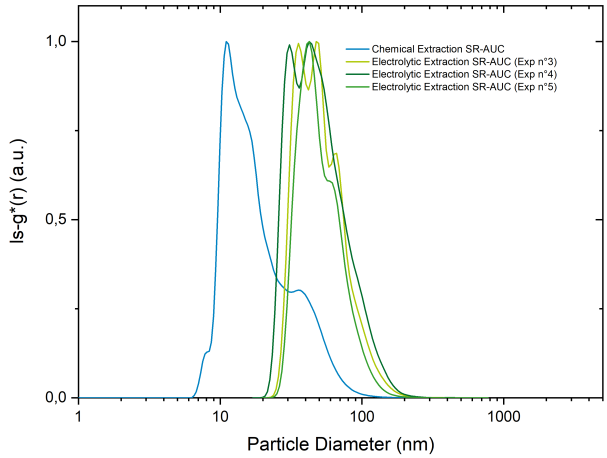

FIGURE 4.14: Number weighted PSDs comparison for electrolytically extracted particles.

SiO_x-network formation

Addition of dispersing agents did not stabilise extracted particles and did not reduce SiO_x-network formation. Process inherent hurdles remain a technological obstacle which needs to be overcome for the electrolytic extraction process to be able to compete with the chemical extraction process developed by Hegetschweiler et al. [52]. The formation mechanism of SiO_x-network throughout electrolysis must be understood to overcome the SiO_x-network technological obstacle.

Iler [98] extensively discusses silica polymerisation for aqueous systems. In aqueous systems silicic acid polymerises to form nanoparticles by silanol group condensation. Particle formation is followed by particle growth and then particle linking to a three dimensional network.[98] For non-aqueous systems the polymerisation mechanism of silicic acid is largely unknown.[98] Under the assumption that the silica polymerisation mechanism in non-aqueous systems could be similar to the polymerisation mechanism in aqueous systems, silica nanoparticles were added as heterogeneous nucleation sites. The SiO_x-network would predominantly form around the added 30 nm diameter silica particles instead of engulfing extracted particles. Electrolytic extraction was carried out at 100 mV vs Ag/AgCl for 5 h with the methanol based maleic anhydride electrolyte containing 10 wt% maleic anhydride, 2 wt% TMAC and 1.5 mL of silica particle suspension (41.644 nmol $\cdot$ L^{-1}). 221.1 mg of steel B were dissolved in the course of the extraction. The SiO_x-network did not selectively develop around silica nanoparticles according to TEM (**3** in **Fig. 4.15**).

Neither dispersing agent addition nor silica nanoparticle addition allowed to overcome process-inherent hurdles. The maleic anhydride electrolyte did not provide a suspension allowing for unbiased investigation with colloidal characterisation techniques. The suspension can be investigated with techniques already widely used such as spectrometry [1, 51, 60, 67, 72, 95], electron microscopy [1, 4, 6, 51, 66, 67,

69, 73, 95], or XRD [51, 60, 61, 64–66, 69]. Electrolysis with the maleic anhydride electrolyte has the advantage of dissolving more iron per unit time than other conventional electrolytes for identical electrolysis parameters.[94] This electrolyte appears to be the electrolyte of choice for further process developments when investigating the specific type of microalloyed steel utilised in this section.

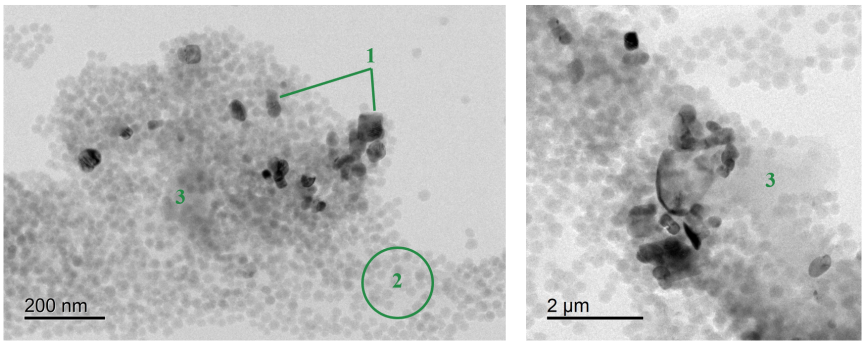

FIGURE 4.15: TEM micrographs of the suspension obtained after electrolytic extraction with the maleic anhydride electrolyte containing silica nanoparticles. (**1**) Extracted particles, (**2**) Silica particles, (**3**) SiO_x-network. Erratum: Both scale bars should indicate 200 nm.

4.1.5 Summarising Remarks

Several non-aqueous electrolytes were used for TiNb(CN) particle extraction from microalloyed steels and led to iron dissolution. Steel needles/fragments and SiO_x microparticles present in the suspensions obtained after extraction with the acetylacetone electrolyte, the methyl salicylate/salicylic acid electrolyte, and the maleic acid electrolyte did not allow for AUC characterisation. The methanol based electrolyte containing 10 wt% maleic anhydride and 2 wt% TMAC was suitable for AUC, but still affected by SiO_x network formation.

Particle agglomeration and a particle engulfing SiO_x-network were observed in suspension for all electrolytes. Formation of a SiO_x-network appears to be an issue inherent to the electrolytic extraction process for the microalloyed steel type investigated in this thesis. Particle agglomeration occurs either during electrolysis through particle engulfment in SiO_x-network, or upon electrolysis completion in the suspension cleaning centrifugation steps.

Process-inherent limitations for the suspension obtained after electrolytic extraction with the maleic anhydride electrolyte could not be remediated through addition of dispersing agents and silica nanoparticles to the electrolyte. While electrolytic extraction with the maleic anhydride electrolyte does provide a suspension suitable for AUC characterisation, it does not provide a suspension of discrete, SiO_x-network free, stabilised particles. The number weighted PSD of particles electrolytically extracted with the maleic anhydride electrolyte does not match the PSD of chemically extracted particles. Differences in PSDs provided by SR-AUC measurements originate from particle agglomeration and/or a particle engulfing SiO_x-network.

Electrolytic particle extraction was not found to be an undesired particle loss reducing alternative to the established chemical extraction route because of the above mentioned process-inherent limitations. Subsequent sections of this thesis rely on

chemical particle extraction developed by Hegetschweiler [1, 52] to enable sub-10 nm particle characterisation.

4.2 Size Fractionation of Chemically Extracted Particles

The chemically extracted particles exhibited multimodal, polydisperse size distributions with diameters ranging from a few nanometres to approximately a hundred nanometres (**Fig. 4.16**). This thesis focuses on the sub-10 nm fraction. The aim is to determine the size and chemical composition of sub-10 nm particles contained in the initial suspension of chemically extracted particles via TEM/EDS, DLS, AUC, ICP-OES. Electron microscopy allows investigations after up-concentration. Size determination in the sub-10 nm range with optical colloidal characterisation techniques such as DLS requires fractionation of the initial suspension to isolate sub-10 nm particles. The scattering intensity of light at nanoparticles is proportional to the sixth power of the particle diameter. Size determination in the sub-10 nm range can also be carried out with fractionating colloidal characterisation techniques. For qualitative chemical composition investigations of chemically extracted sub-10 nm particles via EDS in TEM fractionation is not required. For a quantitative chemical composition study of sub-10 nm particles via ICP-OES fractionation is mandatory to ensure only the elements composing the sub-10 nm particles are analysed.

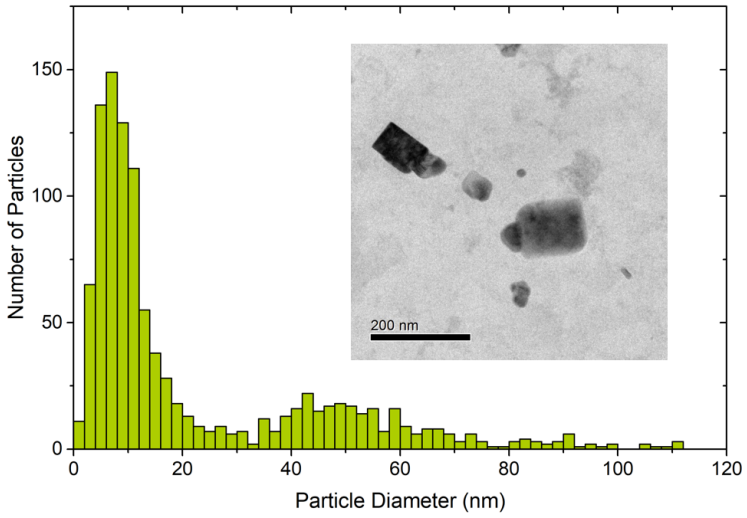

FIGURE 4.16: TEM size distribution of particles chemically extracted from steel C.

Fractionation techniques for the separation of sub-10 nm particles will be discussed prior to the presentation of AUC as a fractionating colloidal characterisation technique, followed by SR-AUC. The ability of SV-AUC and SR-AUC to resolve sub-10 nm particles will be discussed. Finally differential centrifugation will be used to fractionate extracted particles.

4.2.1 Particle Fractionation Techniques

Fractionation is common in nanoparticle applications relying on size and/or shape-dependent material properties. Fractionation can complement synthesis optimisation or be used as alternative to achieve highly monodisperse suspensions containing only desired particle shapes.[156, 157] This section discusses the suitability of

fractionation techniques for particles extracted from microalloyed steel.

Postextraction Fractionation

Membrane filtration is a fractionation technique employed for extracted particles [3, 4, 6, 7, 55–58, 61, 63, 69–73, 78, 93, 96] with two major drawbacks. First, commercial membranes with pore sizes ensuring sharp cut-off values around 10 nm in particle diameter are not available. Reports investigating particle fractionation in the sub-10 nm size range relied on self-manufactured membranes.[158, 159] In this thesis no suitable commercial membrane for the intended application was found. Second, particle loss in the membrane due to membrane/suspension interactions is a major concern.[160] The chemically extracted particles are stabilised with a dispersing agent. The membrane/dispersing agent interaction could severely impede fractionation efficiency. The suspension provided by chemical dissolution of microalloyed steel sample contains a SiO_x-network having an unknown interaction with the membrane.

Fractionation by size and shape of nanoparticle systems via electrophoresis has been reported by Surugau and Urban [161] but not for particles extracted from microalloyed steels in literature. Hanauer et al. [157] showcased the efficiency of gel electrophoresis for size and shape separation of gold and silver polyethylene glycol stabilised nanoparticles. Several sample-induced limitations have to be considered for gel electrophoresis of extracted particles. First, nanoparticle migration cannot be followed visually due to low sample concentration and optical properties of certain particle populations. Introduction of a fluorescent marker in the Disperbyk-2012 ligand shell is possible, but adds an undesired layer of complexity to the fractionation process. Second, the Disperbyk-2012 ligand shell and its unknown functional groups do not allow particle charge and mobility prediction. The stabilising Disperbyk-2012 ligand shell plays a major role in the separation process, but cannot be understood.[157, 161] No alternative ligands with known properties allowed for chemical precipitate extraction. Third, the mobility of extracted particles is affected by the various shapes, sizes, and chemical compositions of the particles. For such a complex system fractionation efficiency is compromised because empirical determination of the narrow electrophoresis window of operation under consideration of experimental conditions becomes unfeasible.[157, 162] Complex particle systems cannot undergo fractionation via gel electrophoresis only and need an additional fractionation method.[162] Fourth, the hypothetical retrieval of sub-10 nm particles from the gel after separation and subsequent suspension purification induces another processing step. In the light of the numerous limitations listed above, gel electrophoresis of particles chemically extracted from microalloyed steel samples was not considered a suitable fractionation technique in this thesis.

Chromatography is a well established nanoparticle suspension fractionation technique [160, 163, 164] which has not been reported for extracted particles in literature. Two major sample-induced limitations hinder employment of chromatography for fractionation of particles chemically extracted from microalloyed steel samples. First, particle/column interactions can harm fractionation efficiency.[165] Unavailable information regarding the functional groups of Disperbyk-2012 used to stabilise extracted particles complicates chromatographic system optimisation (e.g. mobile phase pH, sample concentration) to reduce particle/column interactions.[166, 167] Second, eluting fractions are usually identified via UV-Vis spectroscopy.[163–165,

167] The UV-Vis spectra of titanium and niobium carbonitrides investigated in this thesis were studied by Hegetschweiler.[1] Below 400 nm no particle related information is contained in the spectra due to Disperbyk-2012 absorption in the UV region. At higher wavelengths it becomes possible to distinguish between titanium and niobium carbides or nitrides. A suspension of particles chemically extracted from microalloyed steel samples typically exhibits a broad size distribution, various particle shapes and particle chemical compositions. Continuous size distributions add to the sample complexity for chromatography fractionation.

Controlled size-dependent agglomeration/aggregation has not been reported for extracted particles in literature. Controlled size-dependent agglomeration of nanoparticles can be achieved via temperature variations or salt addition to the suspension. No temperature-dependent agglomeration of chemically extracted particles stabilised with the commercial Disperbyk-2012 dispersing agent was observed. The agent stabilised chemically extracted particles and did not allow for particle agglomeration upon salt addition. Controlled size-dependent aggregation of nanoparticles can be achieved in binary liquid mixtures.[168–170] Guo et al. [168] studied aggregation of silica nanoparticles in a 2,6-dimethylpyridine/water mixture. Temperature and time dependency of the fractionation technique only allows for a narrow window of operation to retrieve desired fractions. Further the experimental setup does not allow for reproducible retrieval of particles with desired sizes. Separation of sub-10 nm particles from the initial suspension of chemically extracted particles via size-dependent aggregation in binary liquid mixtures was deemed impracticable with respect to setup and sample volume limitations.

Fractionation via centrifugation includes density and viscosity gradient centrifugation and differential centrifugation. Only differential centrifugation is reported in literature for extracted particles.[1, 51–53, 59, 64–67] Density and viscosity gradient centrifugation using gradients built from solutions of a single chemical are not considered in this thesis for fractionation of particles chemically extracted from microalloyed steel samples due to layer instability complicating sample handling.[171, 172] The use of aqueous multiphase systems ensures stable gradients facilitating sample handling.[173, 174] Density gradient centrifugation via aqueous multiphase systems allows for particle separation according to particle density differences.[173] The development of a density gradient suitable for separation of sub-10 nm particles from the suspension obtained after chemical dissolution of microalloyed steel samples requires consideration of the sample complexity. The obtained suspension displays a broad, continuous size distribution with no apparent distinct particle sub-populations. The chemical composition of the extracted particles strongly varies in terms of niobium and titanium contents depending on particle size. Chemical composition variations directly affect particle density and particle sedimentation behavior in a density gradient. Optimisation of a density gradient based on aqueous multiphases as performed by Akbulut et al. [174] for purification of a gold nanorod suspension was deemed unrealistic for the particle system investigated in this thesis due to sample complexity. Differential centrifugation allows to separate nanoparticles according to their density without a density, or viscosity gradient.[156] The sedimentation rate of particles in a homogeneous medium is determined via Stokes' law for a given rotor speed and centrifugation temperature. Centrifugation parameters are determined assuming spherical particles to ensure particles of a given size and chemical composition sediment. Compared to density gradient centrifugation, differential centrifugation is a straight-forward fractionation technique which can

swiftly be implemented after centrifugation parameter determination with Stokes' law. Differential centrifugation was selected because it provides satisfying fractionation efficiency while limiting tedious fractionation system optimisation for the complex colloidal system investigated in this thesis.

Fractionating Characterisation Techniques

Fractionating characterisation techniques are reported in literature for particles extracted from microalloyed steels.[1, 99–101] Flow-field flow fractionation separates particle populations according to diffusion coefficient differences. Fractions exiting the separation channel are then detected via DLS and/or UV-Vis spectroscopy. Preliminary works found membrane/particle interactions to be more pronounced in asymmetric F4 than in hollow-fiber F4.[175] Non-negligible particle loss in hollow-fiber F4 and lacking reproducibilty in obtained size distributions disqualified F4 as suitable fractionating characterisation technique for particles chemically extracted from microalloyed steel samples.[175]

AUC fractionates and analyses suspensions simultaneously, and no surface distorts size distributions. AUC is of particular interest for the colloidal system investigated in this thesis due to its ability to resolve all particles in presence with Ångström resolution. Suitability of SV-AUC and SR-AUC to resolve sub-10 nm particles in the multimodal, polydisperse suspensions of particles chemically extracted from microalloyed samples will first be discussed.

4.2.2 Analytical Ultracentrifugation

SR-AUC implementation was validated by comparing size distributions determined via SR-AUC and SV-AUC for a mixture of reference gold nanoparticles (**Appendix C**). The size distributions of chemically extracted particles were determined via SR-AUC and SV-AUC. Their validity is discussed by comparison with size distributions determined via electron microscopy analysis of CERs. Suitability of SR-AUC for qualitative statements upon chemical composition of extracted particles is discussed.

Particles chemically extracted from steel C and A/B were analysed via SR-AUC and SV-AUC (**Fig. 4.17**). SR-AUC and SV-AUC PSDs were in good agreement for both suspensions. SR-AUC is more time efficient than SV-AUC to provide NWPSDs with statistical significance. Minimum particle diameters determined via SR-AUC and SV-AUC were similar (≈ 7 nm). SR-AUC did not allow to improve particle diameter resolution in the sub-10 nm range. To determine whether initial suspension SR-AUC and SV-AUC measurements allow to detect all particles in suspension and enable true minimum particle diameter determination, results on fractionation with subsequent fraction analysis were performed. In the present section the CER STEM data presented for both steel samples suggests that not all particles present in the bulk microalloyed steel sample are present in suspension and/or detected in AUC (**Fig. 4.17**). This finding will be discussed in 4.3.1.

Automated STEM analysis of CERs has been used to validate NWPSDs provided by AUC.[1] NWPSDs provided by automated STEM analysis were previously cut off at 10 nm.[1] Despite reduced resolution in the sub-10 nm range, investigations on reference gold nanoparticle mixtures (**Appendix D**) indicate that automated STEM

analysis can be used in the sub-10 nm size range. Artefacts are likely to alter the true particle size distribution in the sub-10 nm range and require cautious consideration of provided results. Automated CER STEM analysis results for steel C and steel A/B are presented in **Fig. 4.17**. The determined CER STEM NWPSDs are shifted towards smaller particle diameters compared to the AUC NWPSDs. Result validity was investigated for each characterisation technique. TEM analysis of particles extracted from steel C was carried out (**Fig. 4.16**) to validate AUC NWPSD. Bright field TEM analysis reveals particles smaller than in the AUC NWPSD. This is thought to originate from counting artefacts as particles. In the sub-10 nm size range used TEM equipment does not allow for EDS measurements to unambiguously identify particles and distinguish between particles and artefacts. AUC reliably detects particles in suspension for diameters above 10 nm. Automated CER STEM analysis was carried out in oriented dark field (ODF)-mode. CERs present varying carbon film thicknesses and artefacts in the carbon film (grain boundaries, film defects, impurities). Analysis in ODF-mode reduced artefacts. Particles of different size and complex chemical composition exhibit different grayscales. A single particle with a complex chemical composition can display different grayscales. The broad range of particle grayscales in a CER leads to biased results. Both analysis precision and accuracy could be affected. A CER TEM analysis with subsequent manual data analysis provided results with limited statistics which validated automated CER STEM NWPSDS for steel C and steel A/B.

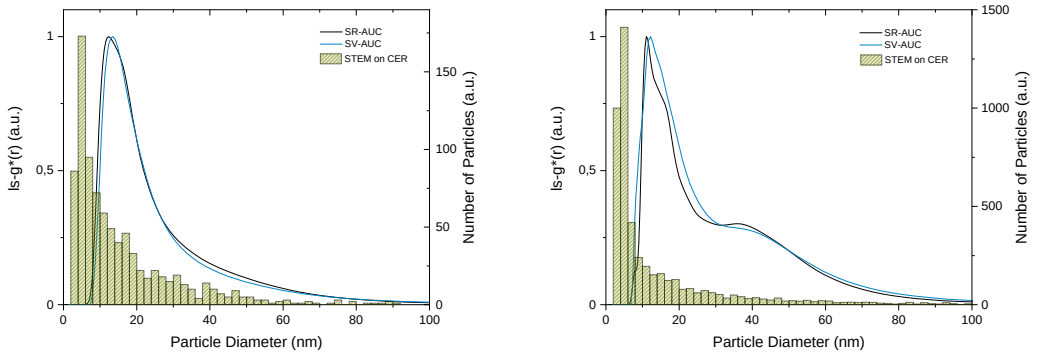

(A) Steel C (B) Steel A/B

FIGURE 4.17: SV-AUC and SR-AUC NWPSDs for chemically extracted particles and automated CER STEM analysis NWPSDs.

AUC analysis and automated CER STEM analysis provide results which could be validated by further investigations. Both characterisation techniques appear to provide reliable results. Discrepancies in AUC and automated CER STEM results are likely to originate from the minimum particle diameter used in the automated CER STEM analysis. Implementing a cut-off at 10 nm would have allowed to detect more particles with diameters above 10 nm which would have resulted in a better match between AUC and CER STEM NWPSDs. This is however not compatible with the aim of this thesis to investigate sub-10 nm particles. The minimum particle diameter selection is linked to the particle grayscale range which has to be detected. Setting a cut-off value at 10 nm could allow to narrow the grayscale range and provide more precise and accurate NWPSDs by discarding sub-10 nm particles with strongly differing contrasts. Due to the rather large number of particles detected in the automated CER STEM analysis discrepancies are not thought to originate from a purely

statistical bias. Isolating and up-concentrating sub-10 nm particles through differential centrifugation could allow for an improved AUC resolution in the sub-10 nm range and clarify whether particles detected in the CER are also contained in the suspension obtained via chemical extraction.

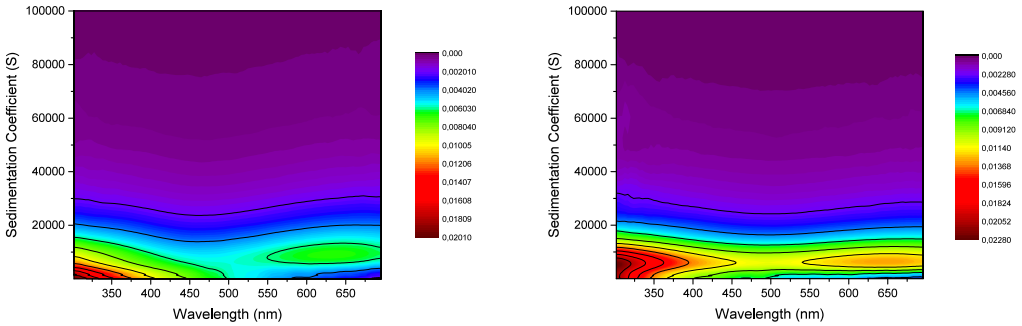

(A) Steel C (B) Steel A

FIGURE 4.18: Comparison of turbidity density projections provided by SR-AUC of extracted particles for two distinct microalloyed steel compositions.

In SR-AUC the turbidity density is recorded over the selected wavelength range for the determined sedimentation coefficients (**Fig. 4.18**). The sedimentation coefficient was used to represent particle size information to avoid biases generated by data analysis. Analysis of the turbidity density projections for steel C and steel A/B focuses on accessible particle chemical composition information rather than on particle size information. Turbidity contains information about the extinction coefficients of particles and sample concentration.[133] Differences in sample concentration are thought to originate exclusively from varying density of particles in the investigated microalloyed steel samples, because a standardised chemical extraction protocol and AUC measurement sample preparation protocol were used. Turbidity density values suggest that steel A has a higher density of particles than steel C (**Fig. 4.18**). Evolution of turbidity density over wavelength is in accordance with optical properties determined by Hegetschweiler for TiNb(CN) particles extracted from microalloyed steels.[1] The optical properties of sub-10 nm and larger particles extracted from both steel samples were similar and indicate similar particle chemical compositions. The difference in chemical particle composition of these populations is insufficient for fraction identification in turbidity density projection.

It remains unclear to which extent sample concentration in sub-10 nm particles enables detection in AUC and turbidity projection analysis. Despite implementation of SR-AUC and turbidity density analysis no additional information on sub-10 nm particles could be gathered compared to SV-AUC. Sub-10 nm particle characterisation via the fractionating characterisation technique AUC was found to provide insufficient resolution in the sub-10 nm range. Postextraction fractionation with subsequent fraction analysis will be carried out to isolate and up-concentrate sub-10 nm particles prior to analysis to improve NWPSD resolution in the sub-10 nm range and allow for unambiguous identification of sub-10 nm particle populations.

4.2.3 Differential Centrifugation Fractionation

Fractionation is required to precisely resolve sub-10 nm particles with colloidal characterisation techniques. Isolating sub-10 nm particles from the larger particles present in the initial suspension allows to prevent the signal intensity of the sub-10 nm particles from being masked by larger particles. Particle fractionation was achieved by differential centrifugation for steel C. Several fractionation experiments were carried out with the parameters listed in **Table 4.5**. The rotor speeds were selected based on Stokes' Law. The rotor speed selection aimed at progressively lowering the particle diameter cut-off value between the supernatant and the residue for a constant centrifugation time and temperature.

Exp. n°	**Temperature** (°C)	**Time** (min)	**Rotor Speed** (RCF)
1	20	15	10 270
2	20	15	23 108
3	20	15	92 434
4	20	15	164 326

TABLE 4.5: Fractionation parameters.

The supernatant and residue were investigated with colloidal characterisation techniques (DLS, SV-AUC) and TEM to determine the cut-off values and fractionation efficiencies. DLS was used to provide statistically meaningful intensity weighted particle distributions. The DLS results presented in **Fig. 4.19** showed size distributions shifted by orders of magnitude from the known size distribution of the sample determined via TEM (**Fig. 4.16**). The inability of DLS to properly depict complex particle mixtures has been reported by Hegetschweiler.[1] The observed trend of higher rotor speeds leading to smaller particles in the supernatant is expected; one would also expect the residue size distributions to retain their maximum values and to broaden towards smaller particle sizes with increasing rotor speeds, since smaller particles are added to the residue. The DLS data provided for residue size distributions n°1, 2, 4 displayed increasing size distribution broadening towards smaller particle diameters for increasing rotor speeds. The fact that residue distribution n°3 did not display the same maximum values as for the other experiments cannot be explained by a handling error during the fractionation experiment, because the supernatant distribution n°3 did not display a higher maximum particle diameter than supernatant distribution n°4. Further, all samples had similar particle concentrations and were sonicated identically. The inconsistency of the residue size distribution n°3 was due to a particle size calculation imprecision of the DLS device. One of the three DLS measurements was slightly different from the two others, leading to a biased average PSD. DLS results allow for a qualitative proof of increasing fractionation efficiency for increasing rotor speeds. Trustworthy cut-off values cannot be determined from DLS data. SV-AUC and TEM were used for more precise cut-off value determination and fractionation efficiency estimation.

The residue PSDs determined via SV-AUC (**Fig. 4.20 A**) broadened towards smaller particle diameters with increasing rotor speeds. This tendency was consistent with the residue PSD DLS results. In contrast to the DLS results, the residue PSDs determined via SV-AUC did not maintain their maximum particle size over increasing rotor speeds. This was most likely due to a combination of shift in particle population ratios over increasing rotor speed, applied conversion steps to achieve a NWPSD

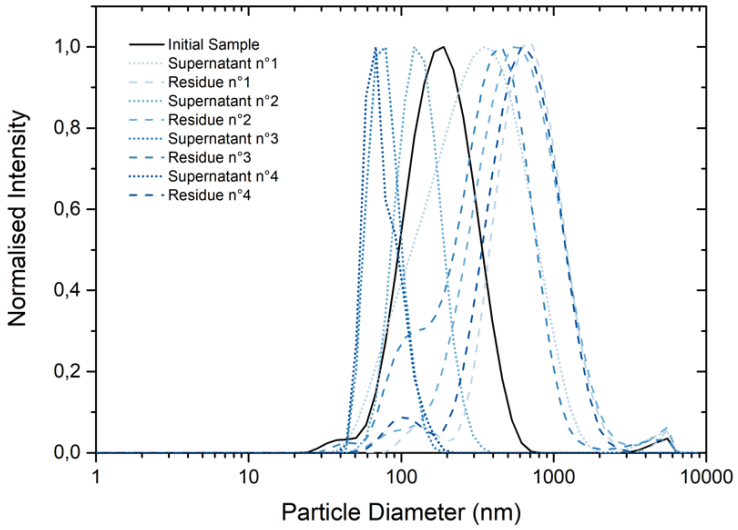

FIGURE 4.19: DLS PSDs for the residues and supernatants of the fractionation experiments.

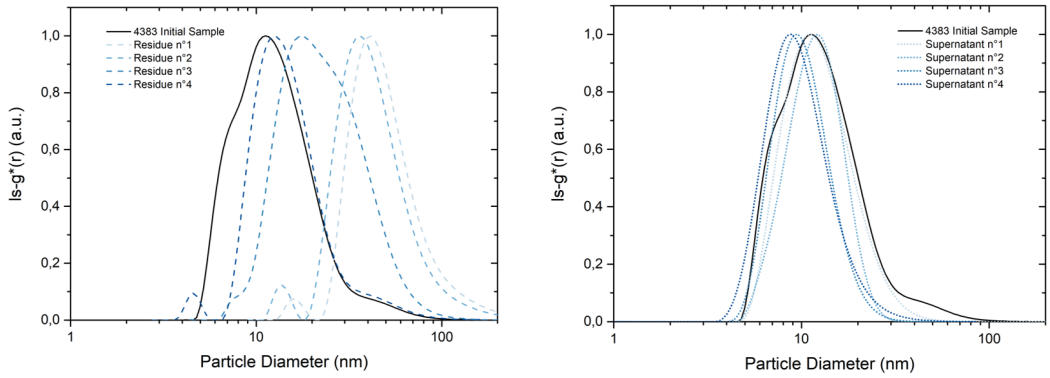

(A) Fractionation Residues

(B) Fractionation Supernatants

FIGURE 4.20: SV-AUC PSDs for the residues and supernatants of the fractionation experiments.

from an extinction weighted sedimentation coefficient distribution, and Mie correction to yield a NWPSD. This combination led to an overrepresentation of the smallest particles contained in the supernatants. The supernatant PSDs determined via SV-AUC (**Fig. 4.20 B**) displayed the same trend as the supernatant PSDs determined via DLS. Higher rotor speeds led to supernatants containing smaller particles. Even though the peak position of supernatant n°2 did not fit into the trend of decreasing peak positions over increasing rotor speeds, the maximum particle diameters detected for each supernatant did.

DLS and SV-AUC indicated successful fractionation experiments and SV-AUC allowed for precise fractionation efficiency determination. Residues and supernatants had an overlapping particle diameter region (**Fig. 4.20**) due to continuous particle size transition in the studied suspension. Despite particles with diameters below 10 nm being found in residue n°4, the fractionation parameters of experiment n°4 provided a promising fractionation efficiency for subsequent sub-10 nm particle characterisation, because the obtained supernatant peak position lied below 10 nm. TEM was used to determine the residue and supernatant PSDs (**Fig. 4.21**) to validate

the size range and partial overlapping of the residue and supernatant PSDs obtained by SV-AUC. The increase in experiment number correlated with an increase in rotor speed during differential centrifugation fractionation. The aim was to determine an adequate rotor speed for sub-10 nm particle isolation.

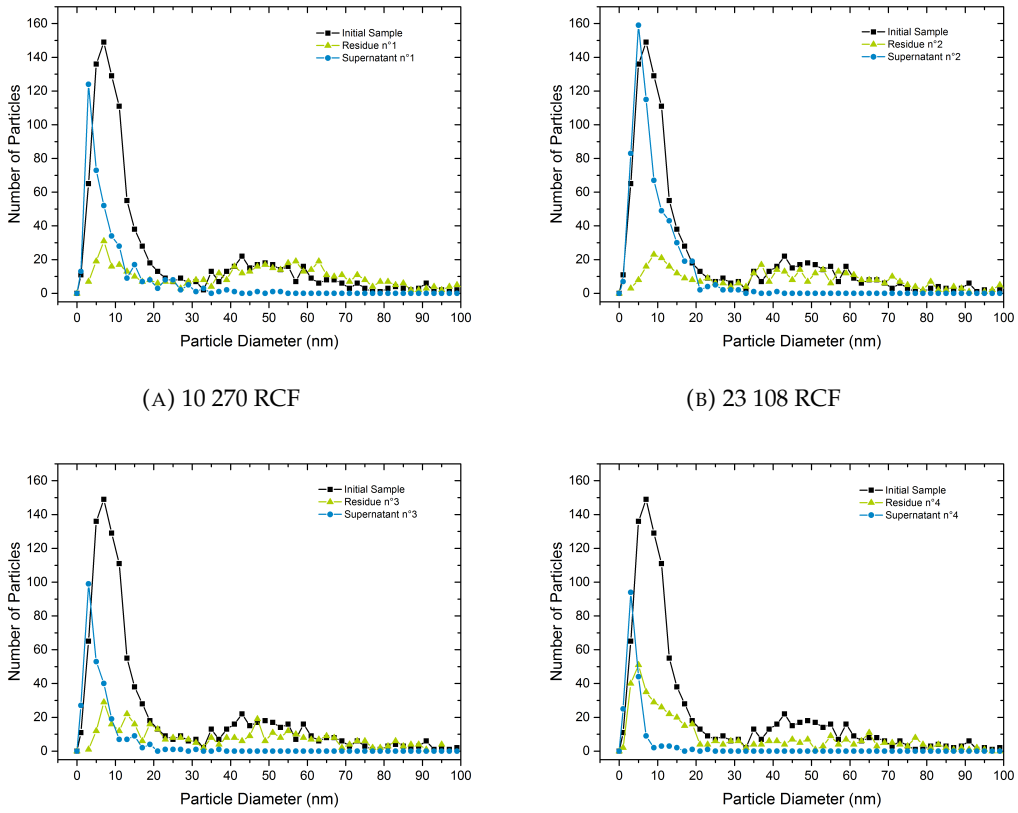

(A) 10 270 RCF

(B) 23 108 RCF

(C) 92 434 RCF

(D) 164 326 RCF

FIGURE 4.21: TEM particle size distributions for the residues and supernatants with increasing rotor speed during differential centrifugation fractionation.

TEM residue PSDs revealed a bimodal suspension with peaks at 10 nm and 50 nm. Detected particle diameter ranges in TEM and SV-AUC were consistent. TEM and SV-AUC supernatant PSDs were consistent and displayed progressive narrowing of the peak towards smaller particle diameters when increasing rotor speed. Almost the entire particle population of supernatant n°4 was in the sub-10 nm region for the TEM PSD. However the peak position which was shifted towards smaller particle diameters over increasing rotor speeds in SV-AUC, did not shift significantly according to TEM, most likely due to the poor statistical relevance of the determined TEM PSDs in comparison to collected SV-AUC data. TEM PSDs were incomplete and partially biased towards smaller particle diameters. SV-AUC was unable to resolve the two particle populations contained in the residues and provided a broad peak containing both populations for the experiments n°1 to 3. SV-AUC residue n°4 marked an exception, as besides the peak located around 10 nm, a shoulder indicating a second particle population started at 30 nm. TEM data indicated that the fractionation parameters of experiment n°4 were promising to isolate predominantly sub-10 nm particles from the initial suspension. TEM data also corroborated the SV-AUC finding relative to the overlap of residue and supernatant PSDs in all four fractionation

experiments.

AUC analysis of chemically extracted particles revealed the need for isolation and up-concentration of sub-10 nm particles for their sizing and chemical analysis. Differential centrifugation was identified as suitable fractionation technique. A combined investigation of the residues and supernatants of the fractionation experiments via DLS, SV-AUC, TEM was carried out for steel C. A rotor speed of 164 326 RCF was found to be beneficial to reduce the amount of particles larger than the desired cut-off value of 10 nm in the supernatant. Fractionation parameters of experiment n°4 were retained for separation of sub-10 nm particles from the initial suspension for subsequent characterisation, as SV-AUC and TEM results indicated that a vast majority of particles in the supernatant n°4 had diameters below 10 nm. A sharp cut-off value could not be achieved due to the sample polydispersity and resulted in a loss of sub-10 nm particles. Residue n°4 contained particles smaller 10 nm according to SV-AUC and TEM.

4.3 Post-Fractionation Analysis of Sub-10 nm Particles

Differential centrifugation fractionation of the suspension extracted from steel C allowed for isolation of sub-10 nm particles. Diameters of extracted particles in the sub-10 nm size range were investigated via AUC analysis of the supernatant. ICP-OES analysis of the fractions enabled chemical composition determination of sub-10 nm particles.

4.3.1 Size Distribution Determination

Analysis of the Fractions

The suspension chemically extracted from steel C underwent differential centrifugation fractionation with the parameters of experiment n°4 presented in 4.2.3 to isolate sub-10 nm particles. AUC was used to assess the number-weighted size distribution of the initial suspension and the fractionation products (**Fig. 4.22**). The supernatant obtained after differential centrifugation contained the smallest particles. AUC measurements were carried out with 12 mm centerpiece cells. The supernatant was measured at 7 kRPM (SV-AUC).

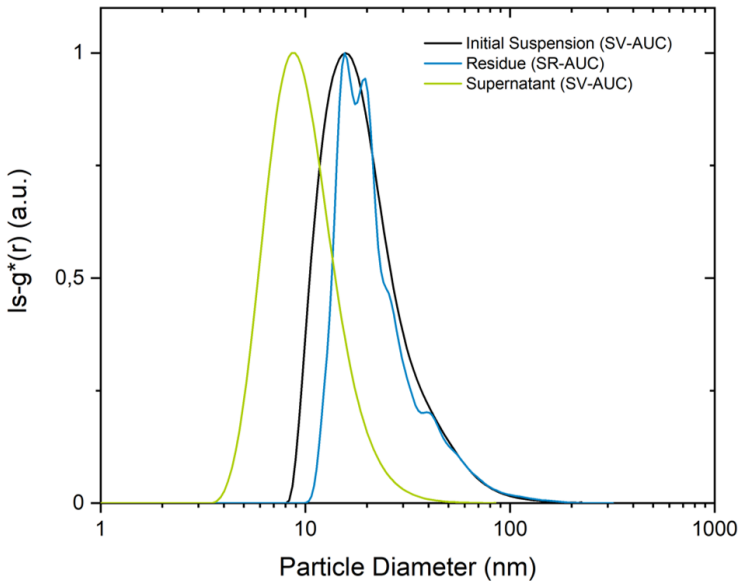

FIGURE 4.22: NWPSDs of the initial suspension and the differential centrigufation fractionation products determined via AUC.

The distribution of particle diameters in the original suspension ranged from 8.1 to 215.5 nm. The residue contained particles with diameters between 9.9 and 228.4 nm. The supernatant contained particles with diameters between 3.5 and 81.5 nm. Smaller particle diameters were detected in the supernatant than in the original suspension. This was thought to originate from the insufficient concentration of smallest particles in the original suspension. Compared to the original suspension, the supernatant contained particles with a minimum diameter 2.3 times smaller. A sharp fractionation cut-off value ensuring presence of sub-10 nm particles only in the supernatant could not be achieved. The supernatant size distribution indicated that the majority of particles in presence were smaller 10 nm. Differential centrifugation fractionation enabled improved particle detection in the sub-10 nm range for chemically extracted particles.

A measurement cell with a 20 mm centerpiece was used and STEM analysis of the supernatant was performed to ensure AUC detected all particles in the supernatant. Particles with diameters below 3.5 nm could remain undetected in AUC measurements with 12 mm centerpiece cells. The 20 mm centerpiece measurement cell only enables detection of sub-3.5 nm particles if the increased extinction compensates for the low particle concentration. The NWPSDs of the supernatant from AUC with 12 and 20 mm centerpiece measurement cells are presented in **Fig. 4.23**. The supernatants were measured at 7 kRPM (SV-AUC). Both distributions displayed a modal diameter at approximately 8.7 nm. The distributions discrepancy in the region of particle diameters larger 10 nm is attributed to handling inaccuracy in the fractionation step leading to slightly different cut-off values. A minimum particle diameter of 3.0 nm was determined with the 20 mm centerpiece measurement cell and of 3.5 nm with the 12 mm centerpiece measurement cell. Supernatant particle concentration was thought to be sufficient for detection of all present particles after the up-concentration step finalising differential centrifugation fractionation.

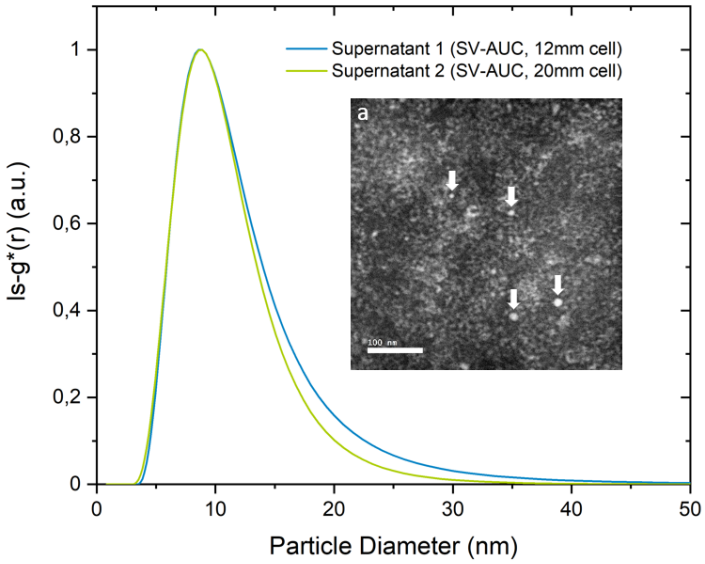

FIGURE 4.23: Comparison of supernatant NWPSDs measured with 12 and 20 mm centerpiece AUC cells. **a)** STEM micrograph of the supernatant.

STEM analysis of the supernatant was carried out to test whether particles smaller than 3.0 nm in diameter existed. All particle diameters determined via STEM corresponded to the size range determined by AUC. Note that STEM analysis did not represent a validation of the AUC minimum particle diameter because of limited statistics, but microalloyed steel samples commonly display continuous particle size distributions. A distinct sub-3.0 nm particle population that remained undetected in AUC and STEM was highly unlikely from a metallurgical point of view. Besides sub-10 nm particles a pronounced SiO_x-network was observed (**Fig. 4.23 a**). The contrast of the SiO_x-network was thought to originate from ions such as niobium or titanium which were formed during chemical extraction through undesired particle etching and were imprisoned in the forming SiO_x-network.[1, 52] The sub-3.0 nm particle contrast was assumed to be more pronounced than the SiO_x-network contrast, because more contrast-contributing elements such as niobium were thought to be present in a particle rather than in a small SiO_x-network portion.

AUC appeared to be a powerful characterisation technique for precise and accurate detection of extracted particles. The minimum particle diameter detected in the supernatant via AUC was of 3.0 nm. The question arised to which extent the minimum particle diameter determined for the supernatant corresponded to the actual minimum particle diameter in the initial microalloyed steel sample. Chemical extraction led to reduced particle diameters due to undesired particle loss. Hegetschweiler et al. [52] found the particle loss to induce a 5 % diameter reduction for titanium and niobium carbonitride particles, corresponding to a minimum particle diameter determined via AUC of 3.15 nm. To determine the minimum particle diameter in the initial microalloyed steel sample automated STEM analysis of a CER of steel C was carried out.

Carbon Extraction Replica Analysis

NWPSDs were determined via automated STEM analysis of a CER and compared to the SV-AUC of supernatants in the sub-10 nm range (**Fig. 4.24**). According to CER STEM analysis, the investigated microalloyed steel sample did not contain sub-3 nm particles. Minimum particle diameters were similar for both characterisation techniques. The STEM PSD was shifted towards smaller particle diameters compared to the SV-AUC NWPSDs. Investigations carried out on gold nanoparticles (**Appendix D**) revealed the tendency of automated STEM analysis to underestimate particle areas, which led to a PSD bias towards smaller particles.

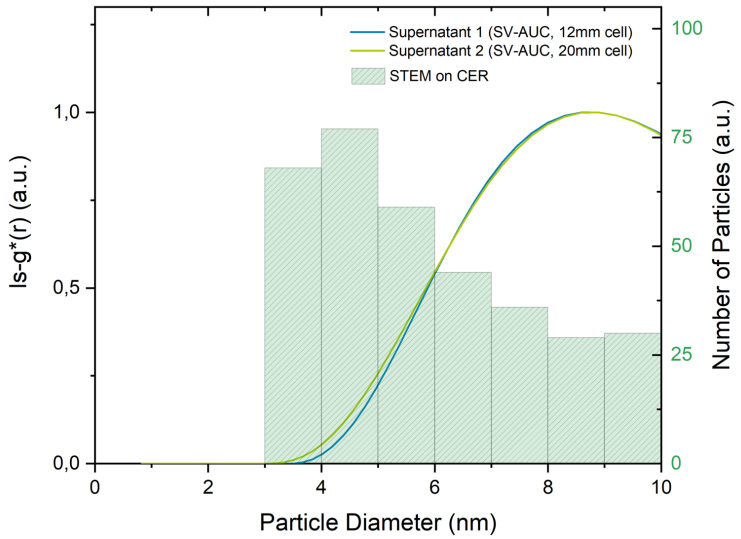

FIGURE 4.24: Sub-10 nm particle analysis via SV-AUC and STEM on CER.

Raw data provided by CER STEM analysis was sorted to avoid consideration of artefacts (**Appendix D**). Particles with an nonexistent EDS niobium signal of a circularity outside 0.1 - 1 were discarded to avoid a further PSD bias. Undesired particle etching inherent to chemical particle extraction leads to a 5 % decrease in particle diameter.[52] However the particles did not display smaller diameters in SV-AUC than in STEM analysis (**Fig. 4.24**) because of the STEM analysis bias towards smaller particle diameters. It remained unclear to which extent particles contained in the bulk sample were lost during chemical extraction and/or remained undetected in AUC analysis. APT was be used as complementary characterisation technique to investigate differences in bulk and extracted minimum particle diameters for steel D

in section 4.4. Differences in obtained NWPSDs for STEM and AUC analysis could potentially also originate from an AUC measurement error. Error sources affecting NWPSDs provided by AUC were discussed in the following section.

Error Sources in Size Distribution Determination via AUC

In this section error sources for NWPSD determination via AUC are discussed for particles chemically extracted from steel C prior to fractionation. Findings are of general nature and can be extended to fractions and other particle suspensions. Errors biasing the NWPSD can occur during AUC measurement and/or AUC data analysis. Errors occurring during the AUC measurement cannot be corrected for at a later stage and should be avoided at all cost. In AUC data analysis errors can be minimised by identifying key parameters and making judicious assumptions.

AUC analysis of chemically extracted particles requires unimpaired particle sedimentation. Chemical particle extraction is accompanied by a SiO_x-network formation.[1, 51, 52, 64, 65] I aimed at investigating the presence of a SiO_x-network in suspension via cryo-TEM and to assess its impact on particle sedimentation. STEM analysis of extracted particles revealed the presence of undesired SiO_x features hindering particle characterisation (**Fig. 4.23 a**). To understand if these features corresponded to drying artefacts cryo-TEM was used to investigate chemically extracted particle suspensions that were rapidly cooled down to cryogenic temperatures to ensure formation of amorphous ice. The SiO_x-network visible in classical electron microscopy was not a drying artefact and was also present in suspension (**Fig. 4.25**). SiO_x features imaged via classical electron microscopy were neither ionic nor dissolved species which dried on the TEM grid. The extent to which the observed SiO_x-network present in suspension affected particle sedimentation is largely unknown. In extreme cases the SiO_x-network enclosed a vast majority of extracted particles and instead of observing the sedimentation of single particles, the sedimentation of large SiO_x-network fragments containing particles was observed. For such extreme cases (**Fig. 4.11**) AUC analysis can clearly be identified as non-suitable characterisation technique. For the suspension of particles chemically extracted from steel C a commercial dispersing agent reduces SiO_x-network formation.[52] Good correspondence between NWPSDs determined via TEM and AUC analysis of extracted particles (**Fig. 4.26**) suggested that the observed SiO_x-network did not greatly bias extracted particle sedimentation. Discrepancies in minimum particle diameters for particles from steel C (**Fig. 4.17, 4.20, 4.22**) were thought to originate from SiO_x-network evolution over time which negatively impacted sample stability. Particle diffusion during AUC analysis can also impair particle sedimentation, but can be avoided through adequate rotor speed selection.

Uncertainties in the NWPSD are introduced by the material parameters assumed for data analysis. Chemically extracted particles are composed of the carbonitride particle core and a dispersing agent shell. The exact particle core density and complex refractive index are unknown for particles chemically extracted from microalloyed steel samples. Further, extracted particles can display populations with different chemical compositions. Particle core density and complex refractive index are estimated (refer to section 3.6.1) to analyse chemically extracted particles prior to fractionation. These estimated values are listed in **Table 4.6** under curve 1. A parametric study consisting in particle core density and complex refractive index variations was

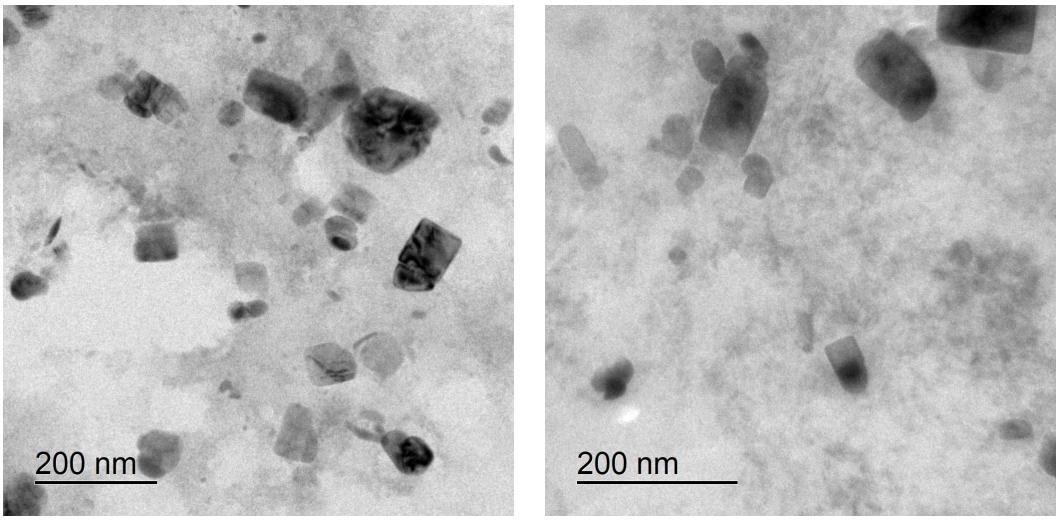

(A) TEM micrograph (B) Cryo-TEM micrograph

FIGURE 4.25: Evidence of SiO_x-network in suspensions of particles chemically extracted from steel C.

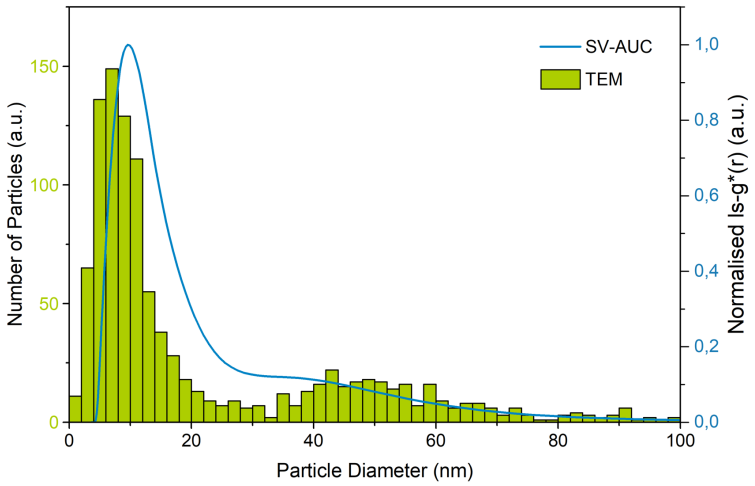

FIGURE 4.26: NWPSDs determined for particles chemically extracted from steel C via TEM and SV-AUC.

performed to determine the sensitivity of AUC NWPSD to erroneous material parameters (**Fig. 4.27**). Particles chemically extracted from steel C were analysed via AUC using the estimated particle core density and complex refractive index (curve 1 in **Table 4.6**). Each particle core material parameter was than varied by 10 % to determine the impact of this error on the NWPSD. A 10 % variation in particle core density led to peak position shifts of approximately 1 nm from 19.7 nm to 20.8 and 18.8 nm. This finding is in good agreement with the mean diameter shift of 1 to 2 nm reported by Goertz et al. [176] for a 5 % particle density error. A 10 % variation in particle core complex refractive index did not affect the peak position. Fractionation allows for refined material parameter estimations leading to a reduced error in obtained NWPSD, because each population can be investigated individually.

Hegetschweiler determined the ligand shell thickness and the ligand density to calculate the overall particle density required for NWPSD determination.[1] However

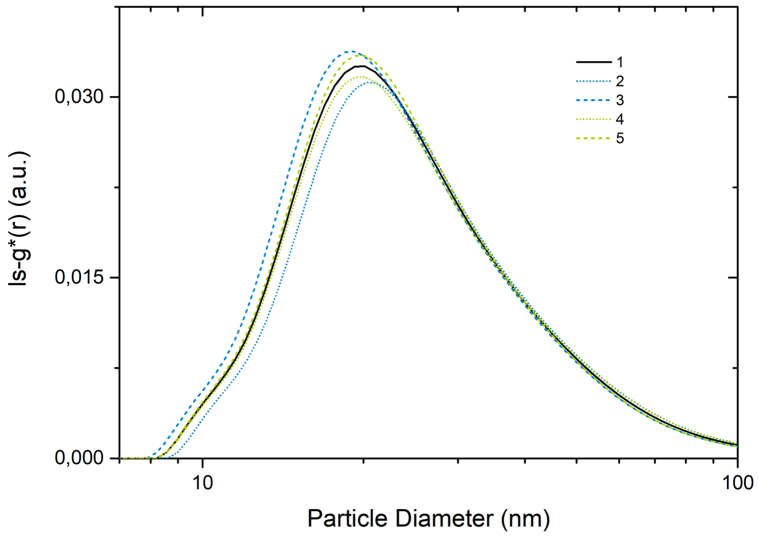

FIGURE 4.27: Bias in AUC NWPSD induced by uncertainties in particle material density and refractive index (**Table 4.6**).

Curve	**Core Density** ($kg \cdot m^{-3}$)	**Refractive Index**
1	6 655	1.72 + 1.55 i
2	5 989.5	1.72 + 1.55 i
3	7 320.5	1.72 + 1.55 i
4	6 655	1.548 + 1.395 i
5	6 655	1.892 + 1.705 i

TABLE 4.6: Effect of varied particle material parameters on NWPSDs displayed in **Fig. 4.27**.

the unknown refractive index of the ligand shell does not allow for optical consideration of the ligand shell during NWPSD determination. This is acceptable because variations in complex refractive index do not affect particle diameters in the NWPSD. Reliable size characterisation via AUC requires spherical precipitates, because AUC analysis only provides information on one particle dimension. Precipitate morphology investigations prior to AUC analysis are crucial to ensure the particle system can be characterised. Both disc-shaped and spherical precipitates can be formed during TMCP. Precipitate shape is determined by the lattice mismatch between the phase in which the precipitate starts to form and the precipitate lattice. Disc-shaped precipitates are predominantly formed for large, spherical precipitates for small phase/precipitate lattice mismatches.

The incident light is anisotropically scattered (Mie scattering) at the particles. In this thesis the Mie correction implemented by Hegetschweiler [1] was applied to determine NWPSDs from EWPSDs. It failed to correct extinction wavelength dependency for extracted particles, because of unknown shell material optical properties and complexity in particle chemical composition, morphology, and shape. Given this complexity, no generic Mie correction with validity for suspensions with particles extracted from various microalloyed steel samples can be developed. Mie correction inaccuracy due to unknown shell material properties could not be remedied by using electrolytic extraction as alternative extraction route. Combination of chemical extraction and differential centrifugation fractionation provided a supernatant

of predominantly spherical precipitates with homogeneous chemical composition, and morphology which was used for Mie correction efficiency investigation. The assumptions on particle properties are more valid for the isolated particles than for the initial suspension. The used Mie correction failed, because the determined NWPSDs differed for the investigated wavelengths (**Fig. 4.28**). Hegetschweiler [1] attributed discrepancies between NWPSDs for wavelengths below 400 nm to the strong light absorption of the ligand shell. With increasing wavelength the discrepancy between NWPSDs of consecutive wavelengths diminishes due to the decreasing light absorption of the ligand shell and to precipitate properties. Mie correction failure could not be prevented by investigation of the supernatant which contained predominantly spherical, morphologically homogeneous particles.

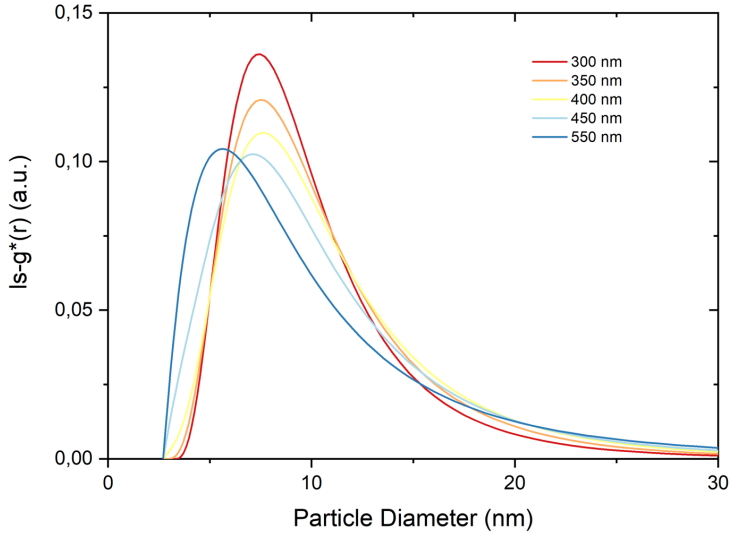

FIGURE 4.28: Wavelength dependent NWPSDs determined via SV-AUC for sub-10 nm particles chemically extracted from steel C.

According to Hegetschweiler [1], the Mie correction has a limited effect on the determined particle sizes and mainly affects the ratios between particle populations in suspension. Despite an inaccurate Mie correction the NWPSDs determined in this thesis are therefore valid.

This section presented several AUC error sources in NWPSD determination and assessed their importance in terms of particle diameter bias. All presented error sources are addressed throughout sample preparation and AUC data analysis to limit their impact on achieved NWPSDs. Both the CER STEM and the AUC analysis of precipitates suffer from limitations. Under careful consideration of those NWPSDs obtained via each technique can be reliably compared and discussed.

4.3.2 Chemical Composition of sub-10 nm Particles

The isolated sub-10 nm particles were investigated via EDS and ICP-OES to determine their chemical composition after differential centrifugation fractionation with the optimised parameters identified in fractionation experiment n°4 (**Fig. 4.21**). SP-ICP-MS which was introduced by Hegetschweiler et al. [1, 67] to quantitatively determine the chemical composition of extracted particles could not be used for sub-10 nm due to a lower detection limit of 26.5 nm for niobium particles (Nb(CN)) and 46.6 nm for titanium niobium particles (TiNb(CN)). It is however possible to target

specific particle populations in ICP-OES through fractionation of the initial suspension.

The supernatant with predominantly sub-10 nm particles was investigated via STEM after up-concentration. The imaged particles had disc shapes and the particle contrast indicated homogeneous particle compositions. EDS point analyses at the center of sub-10 nm particles were carried out (**Fig. 4.29**) to qualitatively examine the titanium and niobium contents. Besides a strong niobium signal, a weak titanium signal could be detected for all investigated sub-10 nm particles. The Ti Kα peak was probably not a pile-up of the Nb Lα1 signal, since the measured Ti Kα peak position was above the value of twice the Nb Lα1 peak position, and the low dead time of the detector made a pile-up unlikely.

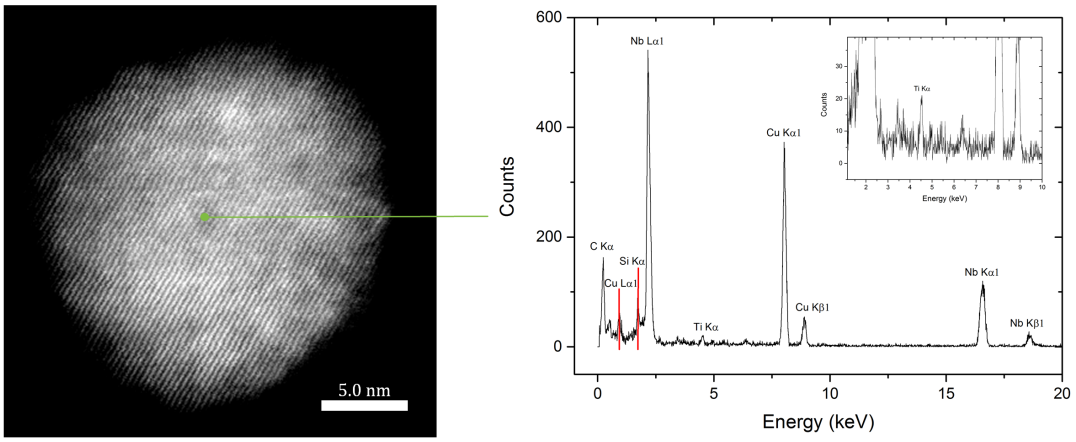

FIGURE 4.29: STEM micrograph and EDS spectrum of a chemically extracted sub-10 nm particle.

ICP-OES measurements were carried out (**Table 4.7**) to confirm the presence of titanium in the sub-10 nm particles.The titanium and niobium contents of the initial suspension containing particles spanning the diameter range presented in **Fig. 4.16** were determined. Then the titanium and niobium contents of the residue and up-concentrated supernatant were determined. Finally the titanium and niobium contents of the supernatants obtained after each of the eight cleaning steps were measured (**Fig. 4.30**). The latter were assumed to originate from non-precipitated titanium and niobium released from the matrix as ions during extraction, because centrifugation ensured complete particle sedimentation. Partial dissolution of particles during extraction also contributes.[52]

Sample	**Ti** ($mg \cdot L^{-1}$)	**Nb** ($mg \cdot L^{-1}$)
Initial Sample	8.275 ± 0.094	15.02 ± 0.13
Fractionation Residue	7.280 ± 0.110	11.800 ± 0.009
Fractionation Supernatant	0.0164 ± 0.0004	1.298 ± 0.005
Supernatant n°8	0.0130 ± 0.0008	0.1536 ± 0.0013

TABLE 4.7: Ti and Nb content in collected fractions determined via ICP-OES.

A slight increase of titanium content at cleaning step four and of niobium content at cleaning step five (**Fig. 4.30**) was not due to a handling error during sample processing after fractionation, because both contents did not increase simultaneously. Undesired SiO_x-network clusters enclosing ionic titanium and niobium [52] were possibly

retained in ICP-OES setup tubings and sporadically released during measurements of certain samples. Eight cleaning steps was a good compromise between obtention of a suspension sufficiently depleted in ionic species and time constraints.[1]

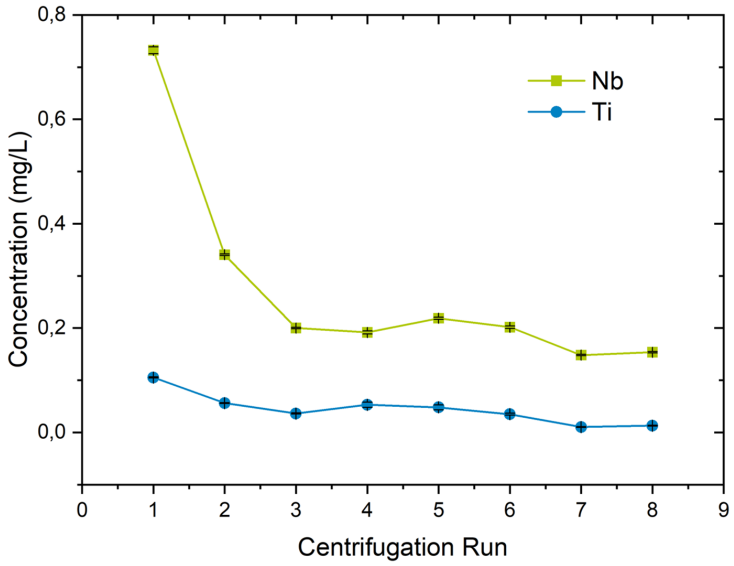

FIGURE 4.30: Decrease in niobium and titanium concentrations in supernatants over eight cleaning steps.

Above results (**Table 4.7**) suggested that the particles larger 10 nm contained close to 88 % of the titanium and close to 80 % of the niobium measured for the initial sample. The titanium to niobium ratio was larger for particles in the fractionation residue, than for particles in the up-concentrated fractionation supernatant. The results also suggested that sub-10 nm particles contained in steel C were almost exclusively composed of niobium. The titanium content of the up-concentrated supernatant which had particulate and ionic contributions exceeded the titanium content of the eighth cleaning step supernatant which had only an ionic contribution. This indicated that sub-10 nm particles contained titanium and corresponded to NbTi(CN) precipitates. 12 % of titanium and 13 % of niobium were lost between the content determination in the initial sample and in the fractionation products. These losses could partly be attributed to fractionation induced particle loss by particle adsorption in the centrifugation tube or in ICP-OES setup tubing. The presented ICP-OES results were regarded as valid evidence for the presence of niobium and titanium in the investigated sub-10 nm particles, because losses only slightly exceeded 10 %.

The quantitative ICP-OES results corroborated the qualitative results of EDS point analysis in STEM. Sub-10 nm particles chemically extracted from steel C contained predominantly niobium and non-negligible amounts of titanium. STEM was used to ensure homogeneity of sub-10 nm particles and EDS point analysis to provide a first qualitative impression of particle constituting elements. ICP-OES was subsequently used for quantitative chemical composition determination focusing on titanium and niobium previously detected in EDS. Atom probe tomography (APT) could provide complementary information about sub-10 nm particle chemical composition, but bulk APT measurements fail to rapidly provide statistically meaningful data for microalloyed steel samples with a low particle density, because it is not possible to target sub-10 nm particles. Efforts to artificially increase particle density in

APT tips to allow for targeted sub-10 nm particle analysis did not provide satisfying results.[177]

4.4 Determination of the Density of Precipitates in Microalloyed Steel

The presented advances in precipitate characterisation can be implemented for a broad range of microalloyed steel samples to foster TMCP optimisation. To further contribute to precipitation kinetics understanding and TMCP optimisation, determination of the number of precipitates contained in a given microalloyed steel volume is required. The number of precipitates contained in a specific microalloyed steel volume will be referred to as number density in the following. Determining the number density of precipitates in a bulk microalloyed steel sample at different TMCP stages leads to an improved understanding of TMCP parameter modification effect on microalloyed steel precipitate number density. Providing a reliable, high-throughput precipitate number density determination technique fosters comprehension of the precipitate number density/mechanical-technological properties correlation and contributes to further TMCP optimisation. Xie et al. [12] determined cluster number densities for distinct cluster size fractions in a niobium microalloyed steel. Precipitate number density determination via APT is limited to microalloyed steel samples with a homogeneous precipitate formation and a sufficiently high precipitate number density due to the limited investigable sample volume.

The precipitate number density determination technique presented in this section relied on AUC analysis of chemically extracted particles and ICP-OES analysis of the bulk sample. It allowed for investigation of several hundred milligrams of microalloyed steel. The sample (steel D) investigated in this section was selected to ensure formation of homogeneous NbC precipitates. A specific heat treatment was carried out to ensure complete niobium precipitation and formation of precipitates with sizes allowing for number density determination via APT and AUC/ICP-OES.

4.4.1 Precipitate Number Density Determination via AUC & ICP-OES

Precipitate number density was determined using **Eq. 4.1**. The chemically extracted precipitates were analysed via AUC to determine a representative precipitate radius which provided an average precipitate mass according to **Eq. 4.2**.

$$\frac{m_{\mathrm{Nb}} + m_{\mathrm{C}}}{m_{\mathrm{P}}} \cdot \frac{\rho_{\mathrm{Steel}}}{m_{\mathrm{Dissolved\ Steel}}} = precipitates\ per\ m^3 \tag{4.1}$$

with m_{Nb} the total mass of niobium and m_{C} the total mass of carbon contained in the precipitates, m_{P} the particle mass, ρ_{Steel} the steel density ($7\,860\,\mathrm{kg \cdot m^{-3}}$), and $m_{\mathrm{Dissolved\ Steel}}$ the mass of dissolved steel.

$$m_{\mathrm{P}} = \rho_{\mathrm{Core}} \cdot \frac{4}{3} \cdot \pi \cdot r_{Particle}^3 \tag{4.2}$$

with ρ_{Core} the particle core density ($7\,820\,\mathrm{kg \cdot m^{-3}}$) and $r_{Particle}$ the particle radius.

To ensure successful precipitate extraction the obtained suspension was investigated via TEM and EDS point analysis was used to identify the homogeneous NbC precipitates (**Fig. 4.31**). SR-AUC indicated a monomodal precipitate population with a maximum at a precipitate diameter of 9.5 nm (**Fig. 4.32**). Contribution of the Disperbyk-2012 ligand shell to the precipitate mass was found to be negligible. ICP-OES was used to determine the total mass of niobium contained in the extracted

precipitates. The ICP-OES analysis of steel D determined a niobium concentration of $0.3635 \pm 0.0061\ \mathrm{mg \cdot L^{-1}}$ with a limit of detection of $1.23\ \mu\mathrm{g \cdot L^{-1}}$, and a limit of quantification of $4.08\ \mu\mathrm{g \cdot L^{-1}}$. This result corresponded to approximately 0.42 mg of niobium in 509.5 mg of steel D.

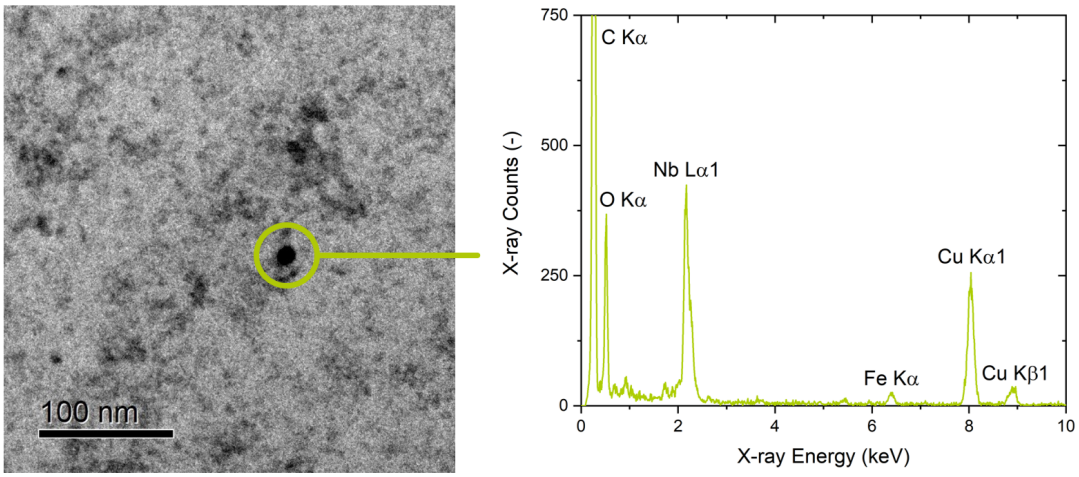

FIGURE 4.31: TEM micrograph and EDS spectrum of a precipitate chemically extracted from steel D.

The total carbon mass contained in the precipitates was derived from the niobium mass in the case of complete niobium precipitation, under assumption of NbC precipitate stoichiometry. EDS analysis identified extracted particles as NbC precipitates. Assuming a NbC precipitate stoichiometry of 1:1 [45] the total carbon mass contained in the precipitates could be determined. Knowing the niobium mass and the mass of a single niobium atom the number of niobium atoms contained in precipitates could be determined. The carbon mass of 0.05 mg contained in precipitates was determined by multiplying the number of niobium atoms by the mass of a single carbon atom. The investigated microalloyed steel contained 2.64 x 10^{11} particles per mg of steel D which corresponds to 2.08 x 10^{21} precipitates per m^3 assuming a steel density of $7\,860\ \mathrm{kg \cdot m^{-3}}$.

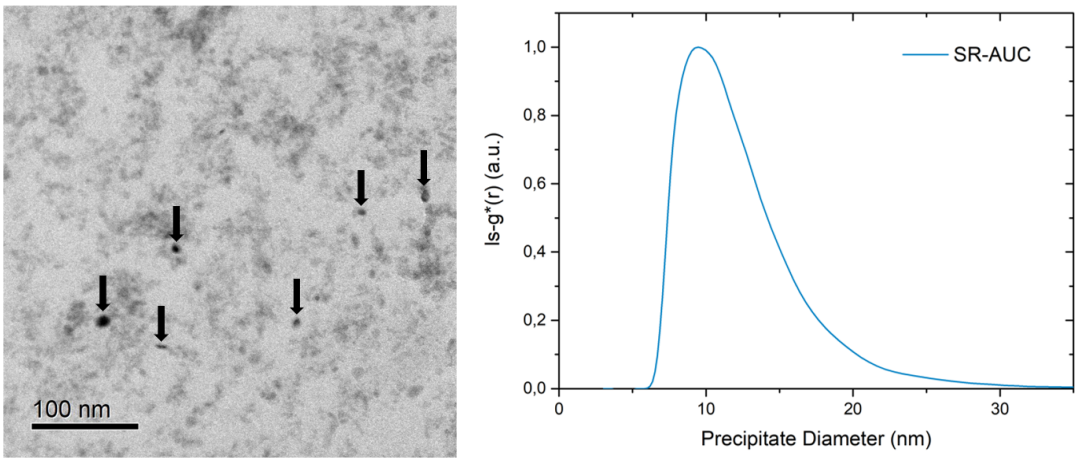

(A) TEM Micrograph

(B) NWPSD determined via SR-AUC

FIGURE 4.32: Size analysis of chemically extracted particles.

4.4.2 Precipitate Number Density Determination via APT

Complementary to precipitate number density determination via AUC & ICP-OES, APT was used because of its ability to detect clusters in addition to precipitates. Particles contained in APT specimens can be defined via isoconcentration surfaces or cluster analysis. First the particle definition based on isoconcentration surfaces will be explained. The APT reconstruction is divided into small 3D pixels also called volume pixels, or voxels. The default voxel size is defined as 1 x 1 x 1 nm^3. For each voxel the niobium concentration can be determined. An isoconcentration surface corresponds to the surface enclosing voxels with a niobium concentration exceeding a defined value. In this thesis a 1 at% niobium isocentration surface was used to define precipitates. Cluster analysis is required for specimens with clusters smaller than a voxel. Particle definition via cluster analysis is more error prone than via isoconcentration surfaces because several parameters have to be considered:

- Minimum number of atoms defining a cluster.
- Maximum distance between two atoms belonging to the same cluster (D_{max}).
- Erosion operation on clusters resulting in removal of atoms at their edges.
- Number of atoms of niobium which must be within a sphere of diameter equal to D_{max} to form a cluster.

The plausibility of selected parameter values was always verified by consideration of the atom distribution outside clusters. Particle definition for each of the four APT specimens was performed with isoconcentration surfaces and cluster analysis to determine the number of precipitates per specimen (**Table 4.8**). Precipitate numbers determined via isoconcentration surfaces were taken as lower limits and precipitate numbers determined via cluster analysis as upper limits. For each specimen a mean precipitate number with the corresponding particle definition error was determined (**Table 4.8**). Besides particle definition, location of precipitates/clusters cutting the edge of APT specimens also impacts the precipitate number density. These precipitates/clusters are only partly contained in the investigated APT specimens and are accounted for with a factor of 0.5 according to the planimetric or Jeffries' procedure.[178] APT precipitate number density was determined by taking the mean of the average cluster analysis and isoconcentration surfaces precipitate number densities. A measurement error of 16.9 % was calculated for APT precipitate density determination.

Specimen n°	Isoconc. Surfaces	Cluster Analysis	Mean	Error
1	8 + 3x0.5 = 9.5	13 + 4x0.5 = 15.0	12.3 $\pm$ 2.8	22.8 %
2	4 + 2x0.5 = 5.0	8 + 2x0.5 = 9.0	7.0 $\pm$ 2.0	28.6 %
3	17 + 7x0.5 = 20.5	25 + 7x0.5 = 28.5	24.5 $\pm$ 4.0	16.3 %
4	5 + 1x0.5 = 5.5	5 + 1x0.5 = 5.5	5.5 $\pm$ 0.0	0.0 %

TABLE 4.8: Precipitate identification in APT for each specimen via isoconcentration surfaces and cluster analysis.

Reconstructed atom maps of steel D specimens are displayed in **Fig. 4.33**. Each specimen contained several precipitates which hints at a homogeneous NbC precipitation formation. For each specimen the precipitate number density in precipitates

per m^3 of investigated steel D sample was calculated by counting the detected precipitates in the specimen of known volume (**Table 4.9**). Averaging precipitate densities over the four investigated specimens provided the niobium microalloyed steel precipitate density of 165.94 x 10^{21} precipitates per m^3.

Specimen n°	**Number of Precipitates**	**Specimen Volume** (nm^3)
1	12.3 ± 2.8	48 700
2	7.0 ± 2.0	75 500
3	24.5 ± 4.0	140 100
4	5.5 ± 0.0	38 300

TABLE 4.9: Precipitate number density in APT based on precipitate identification in specimens of known volumes.

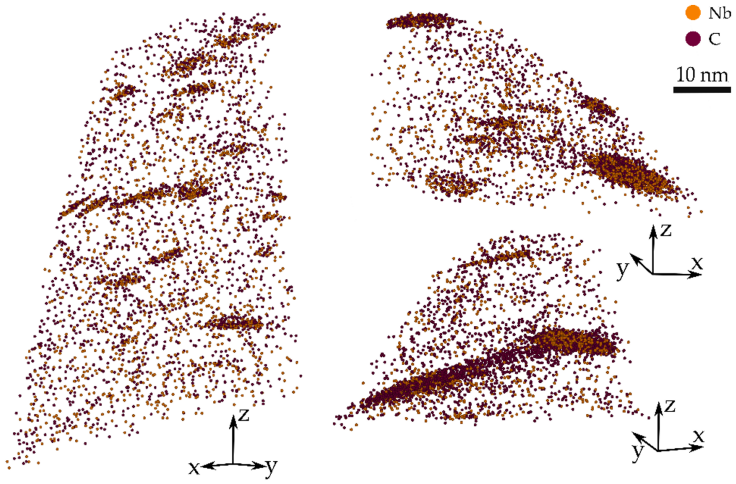

FIGURE 4.33: Reconstructed atom maps of several APT specimens of steel D showing only Nb and C atoms.

APT also provided information on shape and chemical composition of precipitates. These findings allowed validation of assumptions made during precipitate number density determination via AUC & ICP-OES. Precipitates were found to contain predominantly niobium and carbon. Seldomly traces of nitrogen of up to a tenth of the carbon fraction could be detected in the precipitates. Detected precipitates were therefore approximated to NbC precipitates. In the four investigated specimens the atomic fraction for Nb:C varied from 42:58 to 55:45. The NbC precipitates were considered to contain niobium and carbon in equal atomic fraction. Precipitates displayed an oblate, almost disc-shaped morphology (**Fig. 4.33**). Precipitate reconstruction can be distorted by the so-called local magnification effect. The local magnification effect is induced by the existence of neighbouring phases with different evaporation field strengths. The phase with the larger field strength value experiences a local magnification.[179] Because Nb-precipitates have a much higher field strength than iron according to Webel et al. [177] the local magnification effect distorts precipitate reconstruction. A definitive statement on precipitate shape cannot be made via APT only.

4.4.3 Comparison of Precipitate Number Density Determination Techniques

Precipitate number densities were determined via AUC/ICP-OES and APT (**Table 4.10**). The precipitate number density determination technique relying on AUC/ICP-OES allowed for investigation of a up to fifteen orders of magnitude larger sample volume than APT. Possible explanations for discrepancies in obtained precipitate number densities between the two distinct techniques will be discussed in this section. First, assumptions on complete precipitate formation and sample homogeneity will be discussed. Second, the measurement errors and statistical uncertainties of APT and AUC/ICP-OES will be determined. Finally, the resolution power of APT and AUC across the precipitate size range will be discussed.

Technique	AUC/ICP-OES	APT
Precipitates per m^3 of steel	$2.08 \pm 0.10 \times 10^{21}$	$165.94 \pm 28.07 \times 10^{21}$
Investigated steel volume (m^3)	6.5×10^{-8}	7.6×10^{-23}

TABLE 4.10: Summary of determined precipitate number densities.

Degree of Niobium Precipitation

Precipitate number density determination via AUC/ICP-OES required complete niobium precipitation (95 - 99 %), because ICP-OES was used to determine the niobium mass contained in the steel D chipping mass dissolved for precipitate AUC analysis. ICP-OES provided a niobium content comprising niobium dissolved in the matrix and niobium contained in precipitates. Bulk sample analysis did not allow differentiation between these two contributions. The AUC/ICP-OES precipitate density determination technique could only be used if the determined niobium mass corresponded predominantly to niobium contained in precipitates. A time temperature transformation (TTT) diagram was experimentally determined via small-angle neutron scattering for a α-Fe-Nb-C system by Perrard et al. [180]. For steel D a niobium precipitation superior to 99 % was expected according to the TTT diagram. To validate this finding the niobium content in the matrix of the APT specimens was measured and highlighted characterisation technique complementarity. Less than 0.002 wt% niobium was found in the matrix via APT. Steel D experienced a niobium precipitation of 97.5 %. The complete niobium precipitation assumption was valid and enabled precipitate density determination via AUC/ICP-OES. Rather than putting the AUC/ICP-OES and APT precipitate number density determination techniques in competition this thesis aims at emphasizing their complementarity. APT allowed to validate the assumption of complete niobium precipitation and to confirm the assumed NbC stoichiometry which are required for precipitate number density determination via AUC/ICP-OES.

Sample Homogeneity

A comparison of precipitate number densities determined with the AUC/ICP-OES and APT precipitate number density determination techniques is only valid if homogeneous precipitate formation occurred in steel D at a microscopic scale. Inhomogeneous precipitate formation at the microscopic scale would lead to pronounced discrepancies in determined precipitate number densities, because APT investigates

significantly smaller sample volumes than AUC/ICP-OES (**Table 4.10**). The AUC/ICP-OES precipitate number density determination technique allowed for analysis of several tens of mm^3 of steel. The ability of the AUC/ICP-OES precipitate number density determination technique to investigate such a large sample volume makes it suitable for analysis of microalloyed steel samples with both homogeneous and inhomogeneous precipitate formation at a microscopic scale. This is not the case for APT due to the investigated specimens of limited volumes. The number of precipitates identified via APT in each specimen indicated a fairly homogeneous precipitate formation for steel D at a microscopic/nanoscopic scale. The combination of small investigated sample volume and investigation of a microalloyed steel sample with inhomogeneous precipitate formation leads to discrepancies in determined precipitate number densities.

STEM was used to further investigate precipitate formation homogeneity at the microscopic scale by imaging an electron transparent foil (ETF) of steel D. A foil region containing precipitates is shown in **Fig. 4.34** and indicated homogeneous precipitate formation on the microscopic scale. A minimum particle diameter of 3.3 nm was detected. STEM analysis of an ETF is a two-dimensional technique which is not suitable for precipitate number density determination. The contrast of precipitates in the ETF limited precipitate identification. It depends on precipitate volume and crystallographic orientation. ETF orientation during STEM analysis, volumes of precipitates contained in the foil and foil thickness are key factors impacting precipitate identification.

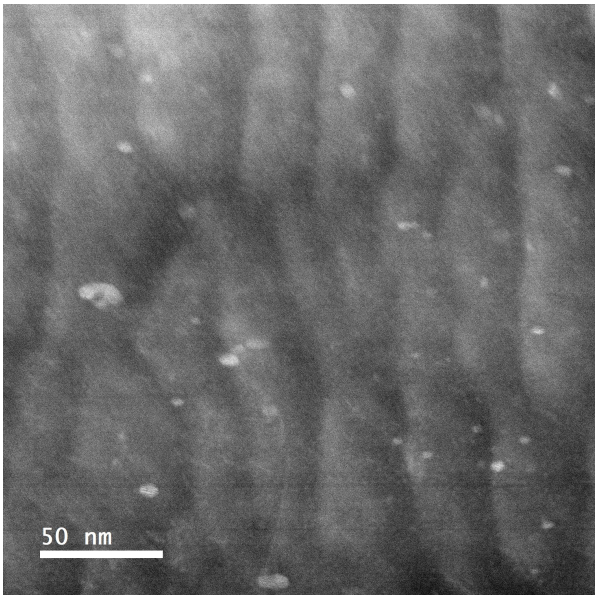

FIGURE 4.34: Precipitate formation homogeneity investigation via STEM of an ETF.

Measurement Errors & Statistical Uncertainties

APT allows to precisely resolve precipitates and clusters, but suffers from a pronounced statistical uncertainty due to specimens volume. AUC/ICP-OES on the other hand provides statistically meaningful data, but suffers from undesired particle loss during extraction which biases AUC results. The APT statistical uncertainty encompassing the measurement error and the AUC/ICP-OES measurement error

were determined to investigate the discrepancy in obtained precipitate number densities.

The APT measurement error of 16.9 % was determined by precipitate identification via isoconcentration surface and cluster analysis for each specimen (**Table 4.8**). The statistical uncertainty was determined by Poisson distribution calculation (**Eq. 4.3**) with $\lambda \in \mathbb{R}_+$ and X a real random variable. X follows Poisson's law of parameter λ and $X \hookrightarrow P(\lambda)$ if:

$$X(\Omega) = \mathbb{N} \; and \; \forall n \in \mathbb{N}, P(X = n) = e^{-\lambda} \cdot \frac{\lambda^n}{n!} \tag{4.3}$$

The uncertainty corresponded to the range of precipitates per specimen encompassing 95 % of the calculated Poisson distribution probability values. Under consideration of the average specimen volume those values were converted to precipitate number densities. The statistical uncertainty which considers the measurement error is displayed in **Fig. 4.35**.

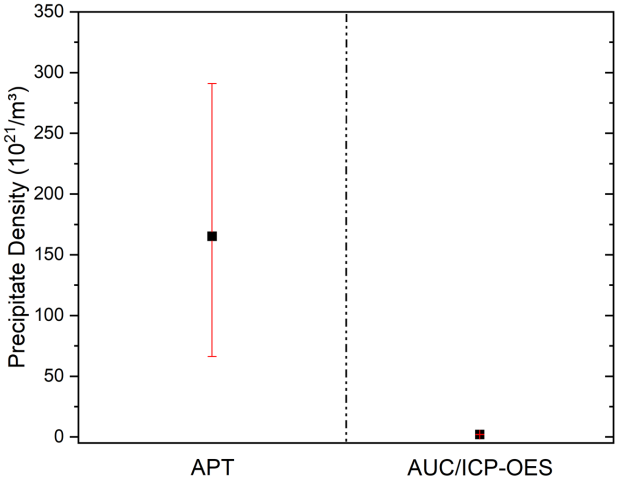

FIGURE 4.35: Comparison of determined precipitate number densities with the statistical uncertainty containing the measurement error for APT and the measurement error for AUC/ICP-OES.

To determine the measurement error of precipitate number density determination via AUC/ ICP-OES error sources in both characterisation techniques are considered. Random and/or systematic errors in AUC and ICP-OES affect the precipitate mass and niobium mass required for precipitate number density calculation. The niobium content was determined with a measurement error of 1.7 % via ICP-OES. Due to the Ångström resolution of AUC, the precipitate diameter is determined with an error of approximately 1 %. Considering the impact of these measurement errors on the determined niobium mass and precipitate mass a measurement error of approximately 5 % can be calculated for the AUC/ICP-OES precipitate density determination technique (**Fig. 4.35**). This measurement error did not account for undesired particle loss. The APT statistical uncertainty did not overlap with the AUC/ICP-OES measurement error thus indicating that undesired particle loss strongly affects the precipitate number density determined via AUC/ICP-OES.

Particle Size Detection Limits

Analysis of APT and AUC NWPSDs (**Fig. 4.36**) as well as of minimum precipitate diameters determined via AUC, APT, and STEM (**Table 4.11**) clearly indicated that the suspension of extracted precipitates was not representative of all precipitates contained in the pristine sample. Precipitate size determination in APT was carried out according to the method introduced by Breen et al. [30].

Characterisation Technique	Minimum Precipitate Diameter (nm)
AUC	6.1
APT	1.2
STEM	3.3

TABLE 4.11: Minimum precipitate diameters in AUC, APT, and STEM.

Sub-6 nm precipitates were contained in the bulk microalloyed steel, but not in the suspension of chemically extracted precipitates. This was due to precipitate loss occurring during the chemical extraction process, which was investigated and quantified by Hegetschweiler et al. [52]. They found the particle loss to reduce precipitate diameters by 5 %. The observed loss of sub-6 nm precipitates did not correspond to a 5 % loss in precipitate diameters. A 3 nm precipitate detected in APT would have a diameter of 2.85 nm in AUC according to Hegetschweiler et al. [52]. In the sub-10 nm diameter region certain precipitates experienced a diameter reduction and others were completely dissolved (**Fig. 4.36**). A 3 nm NbC precipitate is composed of 418 pairs of niobium and carbon atoms and a 30 nm precipitate of 418 570 pairs. An increase in precipitate diameter by one order of magnitude leads to an increase in pairs of niobium and carbon atoms by three orders of magnitude. According to the SR-AUC NWPSD precipitates with diameters below 6 nm or with less than 3 348 pairs of niobium and carbon atoms were completely dissolved during the chemical extraction process. This is plausible since these precipitates are only composed of a few hundreds to thousands of niobium and carbon atom pairs.

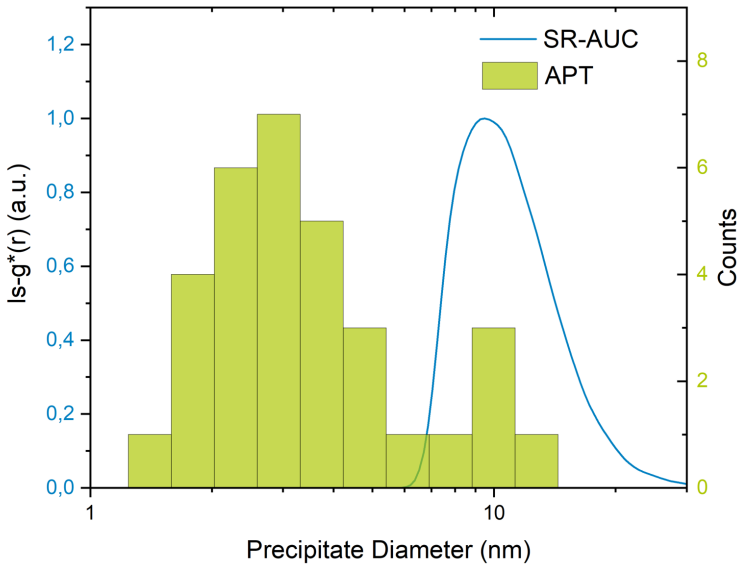

FIGURE 4.36: Difference in accessible, sphere equivalent, particle diameters for AUC and APT.

Loss of sub-6 nm precipitates during the chemical extraction process for steel D led to a partially biased precipitate number density for the AUC/ICP-OES precipitate number density determination technique. Precipitate loss led to a biased NWPSD and determined precipitate mass. Because the niobium mass determined via ICP-OES accounted for sub-6 nm precipitates the calculated precipitate number density was only partly biased. AUC/ICP-OES is suitable for precipitate number density determination of microalloyed steel samples predominantly containing precipitates with diameters above 6 nm. For samples also containing sub-6 nm precipitates the AUC/ICP-OES precipitate number density determination technique has to be combined with APT and/or STEM to allow for comprehensive precipitate analysis. Compared to STEM, APT provided supplementary data on precipitates which were only partially accounted for in the precipitate number density determined via AUC/ICP-OES. STEM theoretically allows to detect precipitates with diameters corresponding to the size range accessible via the combination of AUC and APT in ETFs. STEM analysis of an ETF of steel D was carried out to confirm presence of precipitates with diameters determined via APT and AUC in the bulk microalloyed steel sample. STEM was thought to cover the size range of precipitates detected both in APT and AUC. Practically, contrast considerations and sample heterogeneity greatly impaired STEM analysis and detection of precipitates as small as in APT. Combination of APT and AUC/ICP-OES allows for comprehensive precipitate characterisation. Both techniques access distinct precipitate populations and accordingly provide differing precipitate number densities. The upper limit of diameters which can be detected via AUC allows for detection of even the largest precipitates present in suspension. APT allows for identification of precipitates of a few nanometres and even of clusters. The maximum precipitate size which can be analysed via APT is limited by APT specimen dimensions. A combination of AUC and APT is crucial for precipitate analysis across the whole size range of precipitates contained in the bulk sample.

The observed discrepancy of two orders of magnitude in precipitate number densities determined via APT and AUC/ICP-OES is predominantly thought to originate from undesired particle loss during extraction and the resulting distinct precipitate size ranges investigated by APT and AUC. APT investigations were necessary to investigate precipitates in the size range which was not accessible by AUC/ICP-OES and to achieve a holistic microalloyed steel sample characterisation and study correlations between TMCP parameters and achieved precipitate number densities. Precipitate number density determination via APT is limited to microalloyed steel samples with homogeneous precipitate formation due to the limited sample volume which can be investigated. The AUC/ICP-OES precipitate number density determination technique allows for investigation of microalloyed steel samples with homogeneous and heterogeneous precipitate formation at microscopic scale as well as samples with low precipitate number densities which cannot realistically be investigated via APT. This is due to the comparatively large sample volume which can be investigated via AUC/ICP-OES. Investigation of microalloyed steel samples containing several populations of heterogeneous precipitates represents a limitation of the herein introduced AUC/ICP-OES precipitate number density determination technique.

Chapter 5

Conclusion & Outlook

This thesis focused on developing and implementing new analysis routines to quantify precipitate size, chemical composition, shape, number density, and foster TMCP optimisation. It extends the existing analysis routine to allow for characterisation of sub-10 nm precipitates. Size, chemical composition, shape of sub-10 nm precipitates, and their distributions were investigated by particle extraction, fractionation, and characterisation. This thesis also presents precipitation number density determination techniques.

Undesired particle etching during chemical extraction is a challenge for sub-10 nm particle analysis. Electrolytic particle extraction was tested as alternative extraction technique to minimise particle loss and to allow for analysis of a largely unbiased sub-10 nm particle suspension. The suitability of several non-aqueous electrolytes to provide a suspension of discrete and stabilised particles was assessed. Electrolytic particle extraction provided suspensions with undesired features such as steel needles/fragments, SiO_x microparticles, SiO_x-network, and particle agglomerates hindering subsequent particle characterisation. The methanol based electrolyte containing 10 wt% maleic anhydride and 2 wt% TMAC provided a suspension free of steel needles/fragments and SiO_x microparticles. Attempts to control SiO_x-network formation by addition of silica nanoparticles and to prevent particle agglomeration by addition of dispersing agents to this electrolyte were not successful. Electrolytic extraction was not found to be advantageous compared to chemical extraction. Development of the understanding of SiO_x-network formation in non-aqueous systems undergoing electrolysis is key to inhibit SiO_x-network formation and to achieve suspensions of extracted particles suitable for characterisation with colloidal techniques. This would allow for analysis of unbiased precipitates and for particle loss quantification during chemical extraction.

Sub-10 nm particles were investigated by chemical particle extraction on a microalloyed steel sample. Isolation of sub-10 nm particles from the initial suspension was achieved via differential ultracentrifugation fractionation. ICP-OES analysis of the initial suspension and the fractions indicated that sub-10 nm particles contained in the investigated microalloyed steel were predominantly composed of niobium and also of non-negligible amounts of titanium. Particle detection in the sub-10 nm size range was pursued with SR-AUC analysis of unfractionated suspensions and a combination of AUC and electron microscopy analysis of sub-10 nm particles isolated through differential centrifugation. SR-AUC did not allow for an improved detection of sub-10 nm particle populations without post-extraction fractionation. NW-PSDs in the sub-10 nm diameter range determined via SV-AUC and automated CER STEM analysis were compared to study differences in minimum particle diameters

in the pristine microalloyed steel and in the suspension containing chemically extracted particles. Error sources in NWPSD determination via AUC were identified and discussed. Extension of the existing analysis routine to sub-10 nm particles benefits TMCP optimisation by providing adequate tools for the monitoring of precipitate properties during TMCP.

The precipitate number density in microalloyed steels is crucial to study the effect of changes in TMCP parameters on the number density and resulting mechanical-technological properties. It was determined for a niobium microalloyed steel using APT analysis and a combination of AUC analysis of extracted particles and ICP-OES analysis of steel chippings. The difference of two orders of magnitude in determined precipitate number densities between the two techniques stemmed from undesired particle loss during extraction. This thesis highlights the complementarity of the matrix dissolution technique with subsequent particle characterisation and of APT analysis of bulk microalloyed steel samples. A combination of the existing analysis routine relying on chemical particle extraction with APT allows for a holistic precipitate property profile determination. This complementarity allowed for an improved estimation of undesired particle loss during chemical extraction by comparison of NWPSD determined via AUC and APT. Application of this technique combination to technical relevant microalloyed steels at different stages of their TMCP would foster precipitation kinetics understanding. Concomitant monitoring of the precipitate number density and resulting mechanical-technological properties would enable comprehensive analysis of these steels.

Appendix A

Mathematical Theory of Particle Sedimentation

A.1 Sedimentation Equivalent Diameter Determination

$$m_P \cdot (1 - \bar{v} \cdot \rho_S) = 3 \cdot \pi \cdot \eta_S \cdot s \cdot x \tag{A.1}$$

Which can be rewritten since $\bar{v} = \frac{1}{\rho_P} = \frac{V_P}{m_P}$:

$$V_P \cdot (\rho_P - \rho_S) = 3 \cdot \pi \cdot \eta_S \cdot s \cdot x \tag{A.2}$$

Which leads to the following equation with the particle volume $V_P = \frac{4}{3} \cdot \pi \cdot \left(\frac{x}{2}\right)^3$:

$$x^3 \cdot (\rho_P - \rho_S) \cdot \frac{\pi}{6} = 3 \cdot \pi \cdot \eta_S \cdot s \cdot x \tag{A.3}$$

$$x^2 = \frac{18 \cdot \eta_S \cdot s}{\rho_P - \rho_S} \tag{A.4}$$

$$x = \sqrt{\frac{18 \cdot \eta_S \cdot s}{\rho_P - \rho_S}} \tag{A.5}$$

with the particle diameter x, the solvent viscosity η_S, the sedimentation coefficient s, the particle density ρ_P, the solvent density ρ_S.

A.2 Core-Shell Particle Density Determination

$$\rho_P = \frac{\rho_{Core} \cdot V_{Core} + \rho_{Shell} \cdot V_{Shell}}{V_{Core} + V_{Shell}} \tag{A.6}$$

$$V_{Core} = \frac{4}{3} \cdot \pi \cdot {l_C}^3 = \frac{4}{3} \cdot \pi \cdot \left(\frac{x}{2} - l_S\right)^3 \tag{A.7}$$

$$V_{Shell} = \frac{4}{3} \cdot \pi \cdot \left(\frac{x}{2}\right)^3 - \frac{4}{3} \cdot \pi \cdot \left(\frac{x}{2} - l_S\right)^3 \tag{A.8}$$

Knowing the expressions for the core, and shell volume **A.5** can be rewritten:

$$\rho_P = \frac{\rho_{Core} \cdot \frac{4}{3} \cdot \pi \cdot \left(\frac{x}{2} - l_S\right)^3 + \rho_{Shell} \cdot \left(\frac{4}{3} \cdot \pi \cdot \left(\frac{x}{2}\right)^3 - \frac{4}{3} \cdot \pi \cdot \left(\frac{x}{2} - l_S\right)^3\right)}{\frac{4}{3} \cdot \pi \cdot \left(\frac{x}{2} - l_S\right)^3 + \frac{4}{3} \cdot \pi \cdot \left(\frac{x}{2}\right)^3 - \frac{4}{3} \cdot \pi \cdot \left(\frac{x}{2} - l_S\right)^3} \tag{A.9}$$

$$\rho_P = \rho_{Shell} + (\rho_{Core} - \rho_{Shell}) \cdot \left(\frac{\frac{x}{2} - l_S}{\frac{x}{2}}\right)^3 \tag{A.10}$$

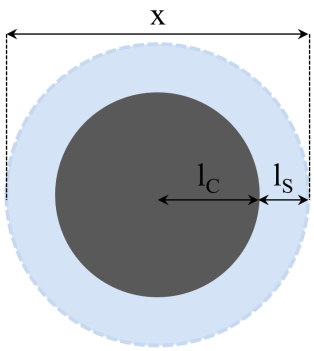

FIGURE A.1: Schematic particle representation with the hydrodynamic diameter x, the core radius l_C, the ligand shell thickness l_S.

$$\rho_P = \rho_{Shell} + (\rho_{Core} - \rho_{Shell}) \cdot \left(\frac{x - 2 \cdot l_S}{x}\right)^3 \tag{A.11}$$

A.3 Particle Diameter Determination

Eq. 2.17 is obtained by combining **A.12**, and **A.11**:

$$x = \sqrt{\frac{18 \cdot \eta_S \cdot s}{\rho_P - \rho_S}} \tag{A.12}$$

$$\frac{x^2 \cdot (\rho_P - \rho_S)}{18 \cdot \eta_S} = s \tag{A.13}$$

$$\frac{x^2}{18 \cdot \eta} \cdot \left(\rho_{Shell} + (\rho_{Core} - \rho_{Shell}) \cdot \left(\frac{x - 2 \cdot l_S}{x}\right)^3 - \rho_S\right) - s = 0 \tag{A.14}$$

$$\frac{x^2}{18 \cdot \eta} \cdot \left(\rho_{Shell} \cdot \left(1 - \left(\frac{x - 2 \cdot l_S}{x}\right)^3\right) + \rho_{Core} \cdot \left(\frac{x - 2 \cdot l_S}{x}\right)^3 - \rho_S\right) - s = 0 \tag{A.15}$$

$$\frac{x^2}{18 \cdot \eta} \cdot \left(\frac{\rho_{Shell} \cdot (x^3 - (x - 2 \cdot l_S)^3) + \rho_{Core} \cdot (x - 2 \cdot l_S)^3}{x^3} - \rho_S\right) - s = 0 \tag{A.16}$$

Appendix B

Electrolytic Cell Setup

An electrolytic cell capable of accommodating three to four electrodes and allowing for a controlled argon atmosphere is required to carry out electrolytic extraction of precipitates from microalloyed steel. Further, the electrodes have to be contacted outside of the cell to avoid corrosion and the setup should be easy to clean, assemble and reuse to allow for high throughput.

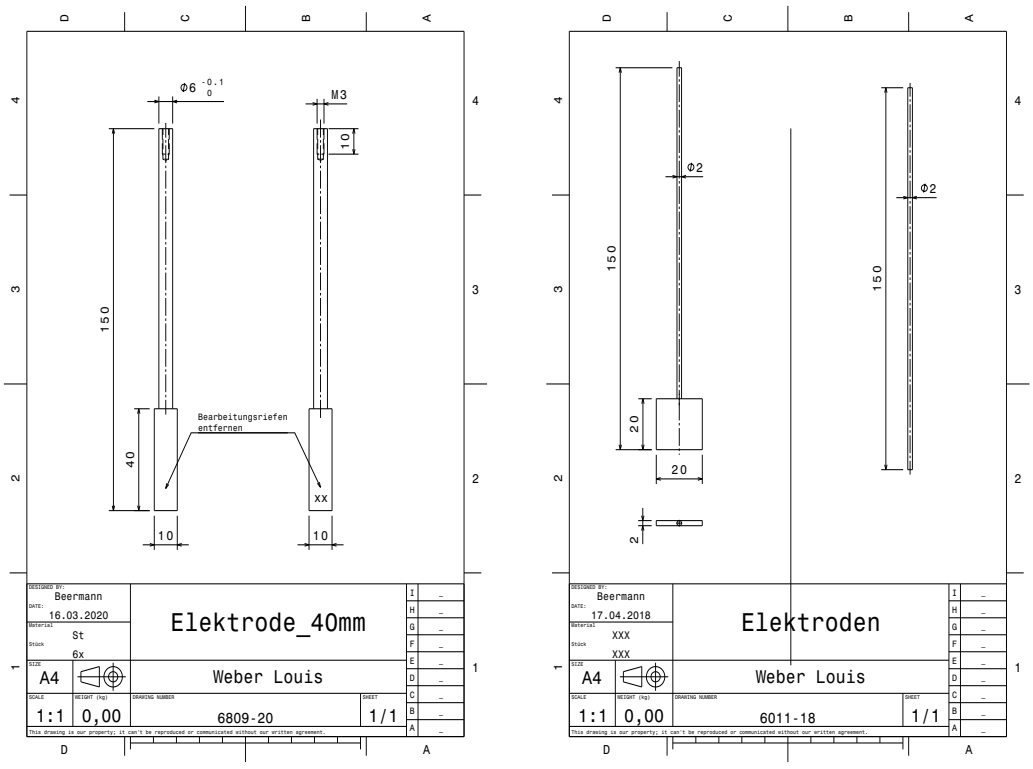

(A) Working electrode. (B) Counter, and reference electrodes.

FIGURE B.1: Technical drawings of the electrodes employed in the electrolytic cell setup.

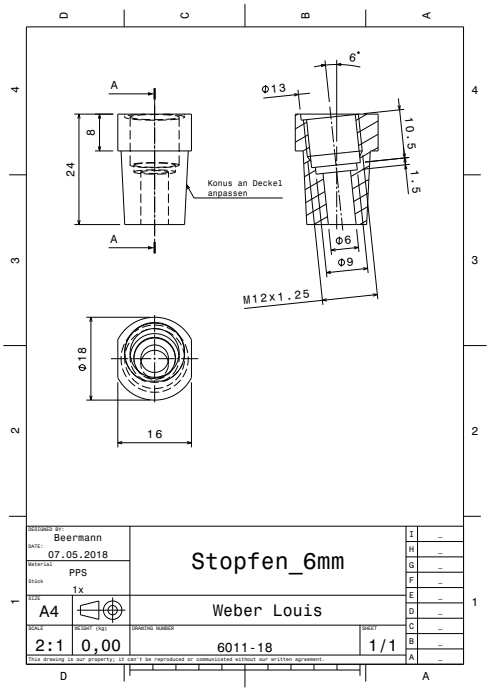

(A) Working electrode plug.

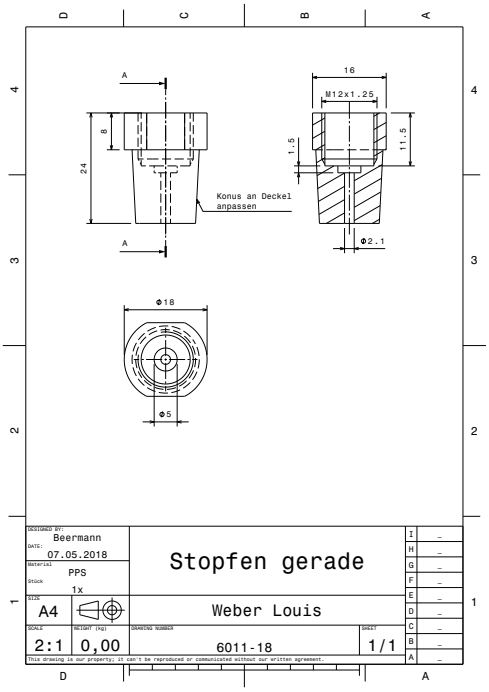

(B) Counter electrode plug.

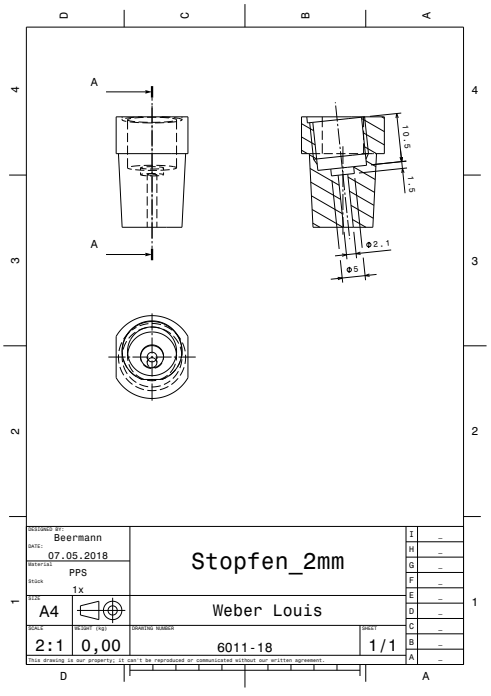

(C) Reference electrode plug.

FIGURE B.2: Technical drawings of the electrode plugs employed in the electrolytic cell setup.

Appendix C

SR-AUC Implementation

C.1 Reference Gold Nanoparticles

Gold nanoparticles of 5, 10 and 30 nm in diameter were separately measured via SV-AUC to determine extinction weighted size distributions. The gold nanoparticle mixture was measured via SV-AUC and SR-AUC to determine extinction weighted size distributions. The extinction size distributions of the single species and the mixture were superimposed to identify differences in gold nanoparticle mixture resolution for SV-AUC and SR-AUC (**Fig. C.1**). Extinction weighted particle size distributions were considered in this section because they are less prone to artifacts and data distortion than the mass and number weighted size distributions.

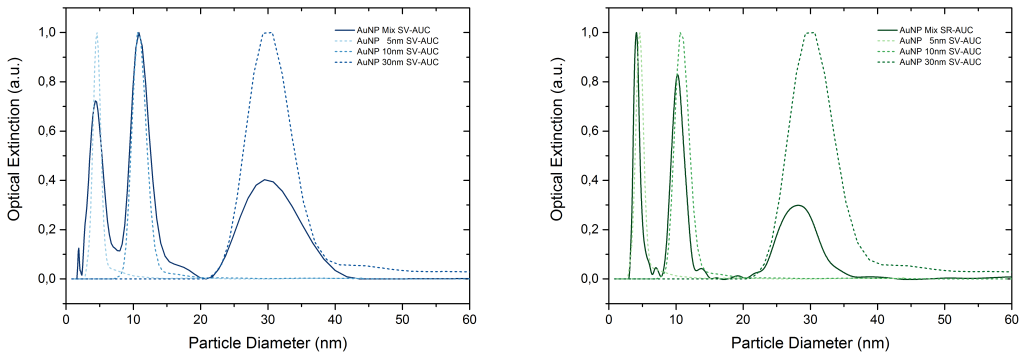

(A) SV-AUC (B) SR-AUC

FIGURE C.1: Comparison of EWPSDs provided by SV-AUC and SR-AUC.

The particle size distributions of the single species determined via SV-AUC provided mean particle diameters which corresponded to manufacturer's specifications (**Table C.1**). TEM analysis of the single species provided particle diameters which were in good agreement to the SV-AUC results and manufacturer's specifications. DLS failed to resolve the single species as precisely as SV-AUC and TEM. The extinction weighted size distributions of the gold nanoparticle mixture determined via SV-AUC and SR-AUC displayed differences but overall provided mean particle diameters which were in good agreement to manufacturer's specifications (**Table C.1**). SR-AUC resolved the 5 and 10 nm gold nanoparticle populations more precisely than SV-AUC. SV-AUC and SR-AUC appeared to resolve the gold nanoparticle mixture with similar accuracy (**Table C.1**). Precision and accuracy of the newly implemented SR-AUC were validated by analysis of reference gold nanoparticles

and comparison of the results to those provided by SV-AUC, TEM, and DLS. SR-AUC appeared to be a reliable, efficient fractionating characterisation technique for analysis of colloidal systems.

Sample	**Characterisation**	**5 ± 1** (nm)	**10 ± 2** (nm)	**30 ± 3** (nm)
AuNP Mix	SV-AUC	4.3 ± 1.3	10.6 ± 2.2	33.0 ± 7.8
AuNP Mix	SR-AUC	3.8 ± 0.4	10.0 ± 1.0	27.3 ± 2.6
Single Species	SV-AUC	4.4 ± 1.8	10.8 ± 1.4	28.6 ± 1.7
Single Species	TEM	5.5 ± 0.7	12.2 ± 1.0	31.9 ± 2.7
Single Species	DLS	7.5 ± 4.2	14.5 ± 5.8	28.2 ± 11.2

TABLE C.1: Diameter determination of the reference gold nanoparticles via AUC, TEM, and DLS.

SR-AUC has three main advantages over SV-AUC for characterisation of multimodal colloidal systems with broad particle size distributions. Two advantages result from the use of a speed ramp and one from the use of a MWL detector. First, measurement time is drastically reduced for SR-AUC compared to SV-AUC. SR-AUC analysis of the gold nanoparticle mixture was carried out approximately 30 times faster than SV-AUC analysis of the same mixture. This is due to rotor speed and particle sedimentation rate considerations. In SV-AUC the fixed rotor speed was selected to ensure enough boundaries were acquired for each particle population and subsequent data analysis was reliable. The selected rotor speed was a compromise between acquisition of sufficient data for the particles with the highest sedimentation rate and measurement of the particles with the lowest sedimentation rate in a reasonable amount of time. Maximum acceptable rotor speed is imposed by the sedimentation rate of the largest particles present in the mixture. Rotor speed should not have exceeded a critical value to avoid collecting insufficient boundaries for the 30 nm gold nanoparticles. Sedimentation rates of 5, 10, and 30 nm gold nanoparticles in water at 20 °C strongly differ for a fixed rotor speed. SV-AUC of the gold nanoparticle mixture lasted approximately 30 times longer than SR-AUC because the rotor speed was selected to ensure enough boundaries were acquired for the 30 nm gold nanoparticles. This rotor speed value led to slow sedimentation of the smallest, 5 nm gold nanoparticles present in the mixture. In SR-AUC the gradually increasing rotor speed ensured all particles in presence were swiftly brought to sedimentation and analysed. Duration of gold nanoparticle mixture SV-AUC could be reduced by fractionation with subsequent single species SV-AUC. Analysis of single species allows to adjust the rotor speed to the investigated particle population. Sufficient boundaries could be acquired faster for the 5 and 10 nm gold nanoparticles than in gold nanoparticle mixture SV-AUC. Single species SV-AUC took approximately 4.5 times longer than gold nanoparticle mixture SR-AUC, but was approximately 6.5 times faster than gold nanoparticle mixture SV-AUC. For a reference system it is feasible to fractionate the nanoparticle mixture to facilitate SV-AUC. For a colloidal system with unknown particle size distribution such a fractionation approach requires multiple empirical optimisation steps.

Second, SR-AUC does not rely on a compromise rotor speed requiring knowledge about investigated particle size distribution. SR-AUC of multimodal colloidal systems with unknown particle size distributions generates accurate and precise particle size distributions from the first measurement on. No optimisation of measurement parameters is required compared to SV-AUC. Valid particle size information for all three gold nanoparticle populations present in the mixture was determined

via SR-AUC within a few hours without previous measurement parameter optimisation.

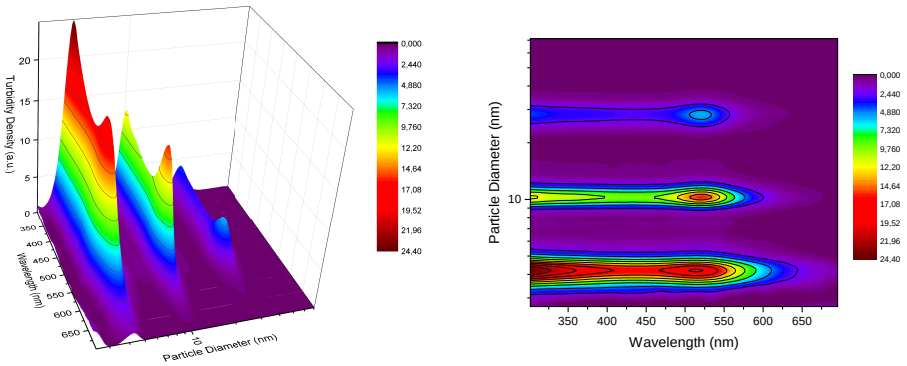

(A) 3D Plot (B) Projection

FIGURE C.2: MWL detector information in SR-AUC.

Third, SR-AUC employs a MWL detector to allow for optical properties analysis of the investigated colloidal system over a broad wavelength range. SR-AUC provides a 3D plot with the turbidity of particles in suspension over detection wavelengths and sedimentation coefficients or diameters (**Fig. C.2 A**). Acquired turbidity signal contains information about sample concentration and extinction coefficients or diameters of particles.[1] Because the optical properties of particles depend upon their chemical composition, variations in particle chemical composition between samples can qualitatively be monitored via SR-AUC by analysing the turbidity density projection onto sedimentation coefficients or diameters and wavelengths (**Fig. C.2 B**). Analysing the turbidity over the sedimentation coefficients or diameters also allows to identify distinct particle populations. For the gold nanoparticle mixture investigated in this section the diameter of the particle populations and the plasmon resonance peak red-shift over increasing particle diameters could be observed (**Fig. C.2**). Representation of turbidity density over particle diameters was preferred to representation of turbidity over sedimentation coefficients, for ease of size information understanding. Corrections performed in HDR-Multifit to convert from sedimentation coefficients to diameters were valid for well defined systems. Sample analysis over a broad wavelength range is of particular interest for analysis of multimodal and/or polydisperse colloidal systems composed of particles with varying chemical compositions because such chemical composition variations affecting the particle optical properties can be identified. Particle population ratios can qualitatively be determined under cautious consideration of information contained in the turbidity signal.

A mixture of reference gold nanoparticles was used to validate SR-AUC and to compare it to the already existing SV-AUC. SR-AUC proved to offer a more time-efficient and straightforward access to particle size distributions compared to SV-AUC. Sample analysis over a broad range of wavelengths performed in SR-AUC allows for collection of particle chemical composition information. SR-AUC represents a major improvement for analysis of multimodal and/or polydisperse colloidal systems with unknown particle size distributions and possible variations in particle chemical composition.

Appendix D

Automated STEM Analysis of Gold Nanoparticles

To determine the suitability of automated STEM analysis in the sub-10 nm particle diameter range a reference colloidal system composed of three gold nanoparticle populations was investigated with STEM, TEM and AUC. Number weighted particle size distributions (NWPSDs) of the reference gold nanoparticle mixture were determined via manual TEM data evaluation, automated STEM analysis, and SR-AUC (**Fig. D.1 A**). NWPSDs provided by TEM, and SR-AUC are in good agreement, and correspond to manufacturer's specifications. The gold nanoparticle mixture was automatically analysed via STEM to evaluate suitability of automated STEM analysis for the sub-10 nm size range. Automated STEM analysis enables identification of the 30 nm particle population with strong statistical significance. Automated STEM analysis detects a second particle population spanning the 5 - 10 nm size range. This second particle population contains the 5, and 10 nm particle populations. Automated STEM analysis is unable to resolve the distinct 5, and 10 nm particle populations. Automated STEM analysis detects particles with unexpected diameters (**Fig. D.1 A**). This can be explained by two observations:

- For numerous 10 nm particles the grayscales complicate automated STEM analysis. In **Fig. D.1 B** the particle surface marked in red is smaller than the particle surface identifiable by eye (**1**). Concerned particles are detected, and labelled with a particle diameter slightly smaller than the true particle diameter. Automated STEM analysis can assign a particle diameter of 7.53 nm to a 10 nm particle (**1**).

  This observation partly explains the presence of particles with unexpected diameters in the 5 - 10 nm, and 15 - 25 nm ranges. Respectively 10, and 30 nm particles are detected, and labelled with a smaller particle diameter.

- Particle agglomeration, and/or insufficient apparatus resolution capabilities do not allow the automated analysis to differentiate particles composing agglomerates, and/or particles located close to each other. In **Fig. D.1 B** the particle surface of two distinct 30 nm particles is marked in red, and assimilated to a single particle by the automated analysis program.

  This observation explains the presence of particles with unexpected diameters in the 35 - 50 nm range. This observation could also explain the presence of particles with unexpected diameters in the 5 - 10 nm range through agglomeration of 5 nm particles, and/or limited apparatus resolution capabilities for 5 nm particles located close to each other.

Limited automated STEM analysis suitability in the sub-10 nm range was demonstrated by analysis of a reference gold nanoparticle mixture. The sub-10 nm range

corresponds to the lower limit of the automated STEM analysis operating window. Automated STEM analysis detects particles in presence in the sub-10 nm range, but fails to identify distinct particle populations. Automated STEM analysis can be employed in the sub-10 nm range for CER analysis under cautious consideration of provided results. Manual triage of provided results to avoid consideration of artefacts/program limitations is strongly recommended. Artefacts can be discarded by considering particles with a defined circularity (e.g. 0.6 - 1) and a significant Ti/Nb EDS count.

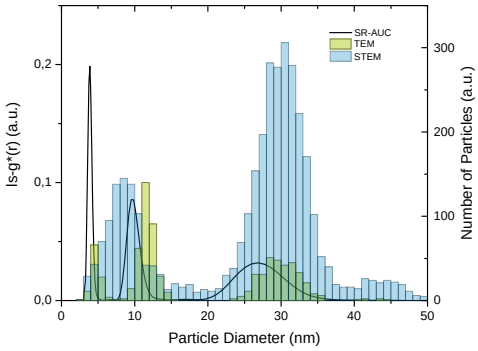

(A) NWPSDs

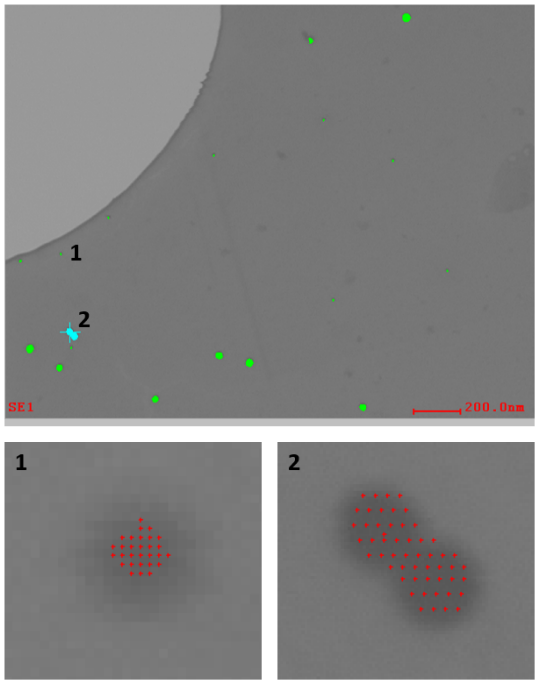

(B) STEM Micrographs

FIGURE D.1: Automated STEM analysis of a gold nanoparticle mixture. (**A**) NWPSDs determined via SR-AUC, TEM, STEM. (**B**) STEM micrographs with particles identified by the automated analysis program.

Bibliography

[1] A. Hegetschweiler.
"Colloidal analysis of particles extracted from microalloyed steels".
PhD thesis. Universität des Saarlandes, Germany, 2018.

[2] I. Timokhina et al.
"On the Ti-Mo-Fe-C atomic clustering during interphase precipitation in the Ti-Mo steel studied by advanced microscopic techniques".
In: *Materials & Design* 111 (2016), pp. 222–229.

[3] T. Sipola et al. "Determination of alloying elements Ti, Nb, Mn, Ni, and Cr in double-stabilized ferritic stainless steel process sample using an electrolytic extraction method and separate analysis of inclusions".
In: *Metallurgical and Materials Transactions B* 46 (2015), pp. 1775–1781.

[4] Y. Bi, A.V. Karasev, and P.G. Jönsson.
"Three dimensional evaluations of REM clusters in stainless steel".
In: *ISIJ International* 54 (2014), pp. 1266–1273.

[5] E. Garfías García, M. Aguilar Sánchez, and M.A. Romero Romo.
"Electrochemical extraction technique and SEM study of precipitated carbides at grain boundaries in austenitic stainless steel".
In: *ECS Transactions* 47 (2013), pp. 149–156.

[6] D. Janis et al. "Application of different extraction methods for investigation of non-metallic inclusions and clusters in steels and alloys".
In: *Advances in Materials Science and Engineering* 2014 (2014).

[7] M. Fernandes, N. Cheung, and A. Garcia.
"Investigation of nonmetallic inclusions in continuously cast carbon steel by dissolution of the ferritic matrix".
In: *Materials characterization* 48 (2002), pp. 255–261.

[8] M. Sennour and C. Esnouf.
"Contribution of advanced microscopy techniques to nanoprecipitates characterization: case of AlN precipitation in low-carbon steel".
In: *Acta Materialia* 51 (2003), pp. 943–957.

[9] H.C. Wang et al. "Effect of Nb on improving the impact toughness of Mo-containing low-alloyed steels".
In: *Journal of Materials Science* 54 (2019), pp. 7307–7321.

[10] L. Jiang et al. "The effect of molybdenum on clustering and precipitation behaviour of strip-cast steels containing niobium".
In: *Materialia* 8.100462 (2019).

[11] K.Y. Xie et al.
"Effect of Nb microalloying and hot rolling on microstructure and properties of ultrathin cast strip steels produced by the Castrip process".
In: *Metallurgical and Materials Transactions A* 42 (2011), pp. 2199–2206.

[12] K.Y. Xie et al.
"Strengthening from Nb-rich clusters in a Nb-microalloyed steel".
In: *Scripta Materialia* 66 (2012), pp. 710–713.

[13] S.L. Shrestha et al. "Cluster strengthening of Nb-microalloyed ultra-thin cast strip steels produced by the Castrip process".
In: *Materials Science and Engineering A* 568 (2013), pp. 88–95.

[14] Y. Kobayashi, J. Takahashi, and K. Kawakami. "Experimental evaluation of the particle size dependence of the dislocation-particle interaction force in TiC-precipitation-strengthened steel".
In: *Scripta Materialia* 67 (2012), pp. 854–857.

[15] M. Charleux et al. "Precipitation behavior and its effect on strengthening of an HSLA-Nb/Ti steel".
In: *Metallurgical and Materials Transactions A* 32 (2001), pp. 1635–1647.

[16] R.D.K. Misra et al.
"Precipitation behavior during thin slab thermomechanical processing and isothermal aging of copper-bearing niobium-microalloyed high strength structural steels: The effect on mechanical properties".
In: *Materials Science and Engineering A* 528 (2011), pp. 8772–8780.

[17] Y.F. Shen, C.M. Wang, and X. Sun.
"A micro-alloyed ferritic steel strengthened by nanoscale precipitates".
In: *Materials Science and Engineering A* 528 (2011), pp. 8150–8156.

[18] C.Y. Chen et al. "Precipitation hardening of high-strength low-alloy steels by nanometer-sized carbides".
In: *Materials Science and Engineering A* 499 (2009), pp. 162–166.

[19] Z.J. Xie et al. "Nano-sized precipitation and properties of a low carbon niobium micro-alloyed bainitic steel".
In: *Materials Science and Engineering A* 641 (2015), pp. 37–44.

[20] M. Béreš et al.
"TEM investigations of fine niobium precipitates in HSLA steel".
In: *Steel Research International* 75 (2004), pp. 753–758.

[21] P. Gong, E.J. Palmiere, and W.M. Rainforth.
"Dissolution and precipitation behaviour in steels microalloyed with niobium during thermomechanical processing".
In: *Acta Materialia* 97 (2015), pp. 392–403.

[22] E.V. Pereloma et al. "Effect of austenite deformation temperature on Nb clustering and precipitation in microalloyed steel".
In: *Scripta Materialia* 75 (2014), pp. 74–77.

[23] M. Nöhrer et al. "Influence of deformation on the precipitation behavior of Nb(CN) in austenite and ferrite".
In: *Metallurgical and Materials Transactions A* 45 (2014), pp. 4210–4219.

[24] H. Dong et al. "Analysis of the interaction between moving α/γ interfaces and interphase precipitated carbides during cyclic phase transformations in a Nb-containing Fe-C-Mn alloy". In: *Acta Materialia* 158 (2018), pp. 167–179.

[25] T. Dorin et al. "Effect of coiling treatment on microstructural development and precipitate strengthening of a strip cast steel".
In: *Acta Materialia* 115 (2016), pp. 167–177.

[26] M. Kapoor, R. O'Malley, and G.B. Thompson. "Atom probe tomography study of multi-microalloyed carbide and carbo-nitride precipitates and the precipitation sequence in Nb-Ti HSLA steels".
In: *Metallurgical and Materials Transactions A* 47 (2016), pp. 1984–1995.

[27] A. Deschamps et al.
"Low temperature precipitation kinetics of niobium nitride platelets in Fe".
In: *Materials Letters* 65 (2011), pp. 2265–2268.

[28] E. Bemont et al. "Precipitation of niobium carbides in Fe-C-Nb steel".
In: *Surface and Interface Analysis* 36 (2004), pp. 585–588.

[29] E.J. Palmiere, C.I. Garcia, and A.J. De Ardo.
"Compositional and microstructural changes which attend reheating and grain coarsening in steels containing niobium".
In: *Metallurgical and Materials Transactions A* 25 (1994), pp. 277–286.

[30] A.J. Breen et al. "Resolving the morphology of niobium carbonitride nano-precipitates in steel using atom probe tomography".
In: *Microscopy and Microanalysis* 20 (2014), pp. 1100–1110.

[31] N. Maruyama, R. Uemori, and M. Sugiyama. "The role of niobium in the retardation of the early stage of austenite recovery in hot-deformed steels".
In: *Materials Science and Engineering A* 250 (1998), pp. 2–7.

[32] F. Danoix et al. "Atom probe tomography I. Early stages of precipitation of NbC and NbN in ferritic steels".
In: *Advanced Engineering Materials* 8 (2006), pp. 1202–1205.

[33] M. Nöhrer et al. "Atom probe study of vanadium interphase precipitates and randomly distributed vanadium precipitates in ferrite".
In: *Micron* 54-55 (2013), pp. 57–64.

[34] J. Takahashi, K. Kawakami, and T. Tarui.
"Direct observation of hydrogen-trapping sites in vanadium carbide precipitation steel by atom probe tomography".
In: *Scripta Materialia* 67 (2012), pp. 213–216.

[35] J.-B. Seol et al. "Core-shell nanoparticle arrays double the strength of steel".
In: *Scientific Reports* 7.42547 (2017).

[36] Y. Kobayashi, J. Takahashi, and K. Kawakami.
"Effects of dislocations on the early stage of TiC precipitation kinetics in ferritic steel: A comparative study with and without a pre-deformation".
In: *Acta Materialia* 176 (2019), pp. 145–154.

[37] Y. Zhang, G. Miyamoto, and T. Furuhara.
"Atom probe compositional analysis of interphase precipitated nano-sized alloy carbide in multiple microalloyed low-carbon steels".
In: *Microscopy and Microanalysis* 25 (2019), pp. 447–453.

[38] S. Dhara et al. "Precipitation and clustering in a Ti-Mo steel investigated using atom probe tomography and small-angle neutron scattering".
In: *Materials Science and Engineering A* 718 (2018), pp. 74–86.

[39] S. Mukherjee et al. "Clustering and precipitation processes in a ferritic titanium-molybdenum microalloyed steel".
In: *Journal of Alloys and Compounds* 690 (2017), pp. 621–632.

[40] S. Mukherjee et al. “Three-dimensional atom probe microscopy study of interphase precipitation and nanoclusters in thermomechanically treated titanium – molybdenum steels”. In: *Acta Materialia* 61 (2013), pp. 2521–2530.

[41] J. Takahashi et al. “The first direct observation of hydrogen trapping sites in TiC precipitation-hardening steel through atom probe tomography”. In: *Scripta Materialia* 63 (2010), pp. 261–264.

[42] J. Wang et al. “Transformation from cluster to nano-precipitate in microalloyed ferritic steel”. In: *Scripta Materialia* 160 (2019), pp. 53–57.

[43] R. Simoneau, G. Bégin, and A.H. Marquis. “Progress of NbCN precipitation in HSLA steels as determined by electrical resistivity measurements”. In: *Metal Science* 12 (1978), pp. 381–386.

[44] Z. Li et al. “Precipitates in Nb and Nb-V microalloyed X80 pipeline steel”. In: *Microscopy and Microanalysis* 19 (2013), pp. 62–65.

[45] G.K. Tirumalasetty et al. “Characterization of NbC and (Nb,Ti)N nanoprecipitates in TRIP assisted multiphase steels”. In: *Acta Materialia* 59 (2011), pp. 7406–7415.

[46] C.P. Scott et al. “Quantitative analysis of complex carbo-nitride precipitates in steels”. In: *Scripta Materialia* 47 (2002), pp. 845–849.

[47] E. Smith and J. Nutting. “Direct carbon replicas from metal surfaces”. In: *British Journal of Applied Physics* 7 (1956), pp. 214–217.

[48] T. Mukherjee, W.E. Stumpf, and C.M. Sellars. “Quantitative assessment of extraction replicas for particle analysis”. In: *Journal of Materials Science* 3 (1968), pp. 127–135.

[49] A.J. Craven et al. “Complex heterogeneous precipitations in titanium-niobium microalloyed Al-killed HSLA steels – I. (Ti,Nb)(C,N) particles”. In: *Acta Materialia* 48 (2000), pp. 3857–3868.

[50] A.J. Craven et al. “Complex heterogeneous precipitations in titanium-niobium microalloyed Al-killed HSLA steels – II. Non-titanium based particles”. In: *Acta Materialia* 48 (2000), pp. 3869–3878.

[51] J. Lu, D. Ivey, and H. Henein. “Quantification of nano-sized precipitates in microalloyed steels by matrix dissolution”. In: *ASME International Pipeline Conference* 3 (2006), pp. 635–642.

[52] A. Hegetschweiler, T. Staudt, and T. Kraus. “An improved method for the matrix dissolution extraction of nanoparticles from microalloyed steel”. In: *Journal of Materials Science* 54 (2019), pp. 5813–5824.

[53] S. Read, R.K. Gibbs, and B.A. Parker. “Extraction and characterization of precipitates formed in a niobium HSLA steel”. In: *Materials Forum* 14 (1990), pp. 304–307.

[54] K. Yamada and R. Inoue. “Analysis for non-metal inclusions and precipitates leading to the optimal steel-properties and processes”. In: *Tetsu-to-Hagané* 100 (2014), pp. 867–872.

[55] J.G. Thompson and J.S. Acken. “Determination of alumina and silica in steel by the hydrochloric acid residue method”. In: *Bureau of Standard Journal of Research* 9 (1932), pp. 615–623.

[56] J.E. Garside, T.E. Rooney, and J.J.J. Belli.
"The alcoholic-iodine method for the extraction of inclusions from steel".
In: *Journal of the Iron and Steel Institute* 185 (1957), pp. 95–103.

[57] H. Bruncková and S. Nižník. "Chemical isolation of precipitates in IF steels".
In: *Chemical Papers* 47 (1993), pp. 346–350.

[58] T.R. Cunningham and R.J. Price.
"Determination of nonmetallic inclusions in plain carbon and manganese steels – Iodine and nitric acid extraction methods".
In: *Industrial & Engineering Chemistry Analytical Edition* 5 (1933), pp. 27–29.

[59] U. Bohnstedt. "Brom-Methanol als Hilfsmittel bei der Oxidisolierung aus Stählen und verwandten Legierungen".
In: *Fresenius' Journal of Analytical Chemistry* 199 (1964), pp. 109–117.

[60] R.G. Smerko and D.A. Flinchbaugh. "Recent progress in the chemical extraction of non-metallic inclusions in steel – Techniques and applications".
In: *Journal of Metals* 20 (1968), pp. 43–51.

[61] K.E. Burke. "Chemical extraction of refractory inclusions from iron- and nickel-base alloys". In: *Metallography* 8 (1975), pp. 473–488.

[62] I.B. Timokhina et al. "Precipitate characterisation of an advanced high-strength low-alloy (HSLA) steel using atom probe tomography".
In: *Scripta Materialia* 56 (2007), pp. 601–604.

[63] R. Dekkers. "Chapter 3 - Characterisation of inclusions".
PhD thesis. Katholieke Universiteit Leuven, Belgium, 2002.

[64] J. Lu et al. "Matrix dissolution techniques applied to extract and quantify precipitates from a microalloyed steel".
In: *Metallurgical and Materials Transactions A* 42 (2011), pp. 1767–1784.

[65] J. Lu et al. "Extraction and characterization of nano-precipitates in microalloyed steels".
In: *ASME International Pipeline Conference* 3 (2008), pp. 85–94.

[66] J. Lu.
"Quantitative microstructured characterization of microalloyed steels".
PhD thesis. University of Alberta, Canada, 2009.

[67] A. Hegetschweiler et al. "Single-particle mass spectrometry of titanium and niobium carbonitride precipitates in steels".
In: *Analytical Chemistry* 91 (2019), pp. 943–950.

[68] J. Webel et al. "Tracing microalloy precipitation in Nb-Ti HSLA steel during austenite conditioning". In: *Metals* 10.243 (2020).

[69] A.L. Rivas et al.
"Electrochemical extraction of microalloy carbides in Nb-steel".
In: *Revista de Metalurgia* 44 (2008), pp. 447–456.

[70] R. Inoue et al.
"Extraction of nonmetallic inclusion particles containing MgO from steel".
In: *ISIJ International* 51 (2011), pp. 2050–2055.

[71] J.C. Herman, B. Donnay, and V. Leroy. "Precipitation kinetics of microalloying additions during hot-rolling of HSLA steels".
In: *ISIJ International* 32 (1992), pp. 779–785.

[72] J.-S. Park et al. “Dissolution and precipitation kinetics of Nb(C,N) in austenite of a low-carbon Nb-microalloyed steel”.
In: *Metallurgical and Materials Transactions A* 40 (2009), pp. 560–568.

[73] H. Doostmohammadi, A.V. Karasev, and P.G. Jönsson.
“A comparison of a two-dimensional and a three-dimensional method for inclusion determinations in tool steel”.
In: *Steel Research International* 81 (2010), pp. 398–406.

[74] S.S. Hansen, J.B. Vander Sande, and M. Cohen.
“Niobium carbonitride precipitation and austenite recrystallisation in hot-rolled microalloyed steels”.
In: *Metallurgical and Materials Transactions A* 11 (1980), pp. 387–402.

[75] J.S. Park and Y.K. Lee. “Determination of Nb(C,N) dissolution temperature by electrical resistivity measurement in a low-carbon microalloyed steel”.
In: *Scripta Materialia* 56 (2007), pp. 225–228.

[76] J.-G. Jung, J.-H. Bae, and Y.-K. Lee.
“Quantitative evaluation of dynamic precipitation kinetics in a complex Nb-Ti-V microalloyed steel using electrical resistivity measurements”.
In: *Metals and Materials International* 19 (2013), pp. 1159–1162.

[77] J.-G. Jung et al. “Carbide precipitation kinetics in austenite of a Nb–Ti–V microalloyed steel”.
In: *Materials Science and Engineering A* 528 (2011), pp. 5529–5535.

[78] L.M. Rothleutner, R. Cryderman, and C.J. Van Tyne.
“Influence of temperature and holding time on the interaction of V, Al, and N in microalloyed forging steels”.
In: *Metallurgical and Materials Transactions A* 45 (2014), pp. 4594–4609.

[79] D. Acevedo-Reyes et al. “Characterization of precipitates size distribution: validation of low-voltage STEM”.
In: *Journal of Microscopy* 232 (2008), pp. 112–122.

[80] E. Courtois, T. Epicier, and C. Scott.
“EELS study of niobium carbo-nitride nano-precipitates in ferrite”.
In: *Micron* 37 (2006), pp. 492–502.

[81] Y. Lee and B.C. De Cooman. “TiN/NbC compound particle formation during thin slab direct rolling of HSLA steel”.
In: *Steel Research International* 85 (2014), pp. 1158–1172.

[82] E.J. Pavlina, C.J. Van Tyne, and J.G. Speer. “Effects of combined silicon and molybdenum alloying on the size and evolution of microalloy precipitates in HSLA steels containing niobium and titanium”.
In: *Materials Characterization* 102 (2015), pp. 35–46.

[83] X. Zhang et al. “Microstructure, precipitate and property evolution in cold-rolled Ti-V high strength low alloy steel”.
In: *Materials and Design* 192.108720 (2020).

[84] H. Lee et al. “Dissolution behaviour of NbC during slab reheating”.
In: *ISIJ International* 54 (2014), pp. 1677–1681.

[85] W. Xiong et al.
“Phase transformation and precipitation mechanisms of Nb microalloyed bainite-martensite offshore platform steel at different cooling rates”.
In: *Steel Research International* 90.1900224 (2019).

[86] A.J. Craven et al. “Spectrum imaging of complex nanostructures using DualEELS: II. Absolute quantification using standards”.
In: *Ultramicroscopy* 186 (2018), pp. 66–81.

[87] B. Sala. “Scanning transmission electron microscopy characterisation of carbide precipitates in steel”.
PhD thesis. University of Glasgow, United-Kingdom, 2019.

[88] C.A. Hoffman and B.C. Buzek.
“Use of surface replication, extraction replication, and thin-film electron microscopy in the study of dispersion-strengthened materials”.
In: *National Aeronautics and Space Administration Technical Note D-4461* (1968).

[89] M.F. Ashby and R. Ebeling.
“On the determination of the number, size, spacing, and volume fraction of spherical second-phase particles from extraction replicas”.
In: *AIME Metallurgical Society Transactions* 236 (1966), pp. 1396–1404.

[90] H. Masuda and K. Gotoh. “Study on the sample size required for the estimation of mean particle diameter”.
In: *Advanced Powder Technology* 10 (1999), pp. 159–173.

[91] A. Weibel et al.
“The big problem of small particles : a comparison of methods for determination of particle size in nanocrystalline anatase powders”.
In: *Chemistry of Materials* 17 (2005), pp. 2378–2385.

[92] Ö.N. Doğan, G.M. Michal, and H.W. Kwon. “True size distribution of simple polyhedral particles obtained from TEM images of extraction replicas”.
In: *Materials Characterization* 34 (1995), pp. 173–179.

[93] “Standard test method for acid-insoluble content of copper and iron powders”. In: *ASTM* E194-10 (2015).

[94] R. Inoue et al. “Applicability of nonaqueous electrolytes for electrolytic extraction of inclusion particles containing Zr, Ti, and Ce”.
In: *ISIJ International* 53 (2013), pp. 1906–1912.

[95] A. Zimmermann. “Development of an electrolytic extraction path of particles in low-carbon microalloyed steel”.
MSc thesis. Universität des Saarlandes, Germany, 2016.

[96] Y. Bi, A.V. Karasev, and P.G. Jönsson.
“Three-dimensional investigations of inclusions in ferroalloys”.
In: *Steel Research International* 85 (2014), pp. 659–669.

[97] K. Mizukami et al. “Method of analysing particle size distribution of particles in metal material”. In: *US Patent* 8,384,897 B2 (2013).

[98] R.K. Iler. *The chemistry of silica – Solubility, polymerization, colloid and surface properties, and biochemistry, Chap. 3, pp. 174-176*. John Wiley & Sons, 1979.

[99] D. Itabashi et al. “Determination of size distribution of nanoparticles using asymmetric flow field-flow fractionation (AF4)”.
In: *ISIJ International* 60 (2020), pp. 979–987.

[100] O. Meili-Borovinskaya et al. “Analysis of complex particle mixtures by asymmetrical flow field-flow fractionation coupled to inductively coupled plasma time-of-flight mass spectrometry”.
In: *Journal of Chromatography A* 1641.461981 (2021).

[101] A. Hegetschweiler et al.
"Colloidal analysis of particles extracted from microalloyed steels".
In: *Particle & Particle Systems Characterization* 2000236 (2021).

[102] R. Lagneborg et al. "The role of vanadium in microalloyed steels".
In: *Scandinavian Journal of Metallurgy* 28 (1999), pp. 186–241.

[103] K. Nishioka and K. Ichikawa. "Progress in thermomechanical control of steel plates and their commercialization".
In: *Science and Technology of Advanced Materials* 13.023001 (2012).

[104] I. Tomoharu, K. Yoshihisa, and Y. Naoshi.
"Analysis method of particulate steel".
In: *Japanese Patent* 2009008584 A (2009).

[105] C. Klinkenberg, K. Hulka, and W. Bleck.
"Niobium carbide precipitation in microalloyed steel".
In: *Steel Research International* 75 (2004), pp. 744–752.

[106] J.R. Davis. "Alloying: understanding the basics".
In: *ASM International* (2001), pp. 193–202.

[107] J.G. Lenard. *Primer on flat rolling, Chap. 8*. Elsevier, 2014.

[108] H.-J. Bargel and G. Schulze. *Werkstoffkunde*. Springer, 2005.

[109] T.N. Baker.
"Processes, microstructure and properties of vanadium microalloyed steels".
In: *Materials Science and Technology* 25 (2009).

[110] T. Gladman. "Precipitation hardening in metals".
In: *Materials Science and Technology* 15 (1999).

[111] W.D. Callister and D.G. Rethwisch.
Fundamentals of materiasl science and engineering, Chap. 8.
John Wiley & Sons, 2008.

[112] M. Meyers and K. Chawla. *Mechanical behavior of materials, Chap. 10*.
Cambridge University Press, 2008.

[113] T.N. Baker. "Microalloyed Steels".
In: *Ironmaking & Steelmaking* 43 (2016), pp. 264–307.

[114] I. Tamura et al. *Thermomechanical processing of high-strength low-alloy steels*.
Butterworth & Co., 1988.

[115] Y. Liu et al. "Effect of TMCP parameters on the microstructure and properties of an Nb-Ti microalloyed steel".
In: *ISIJ International* 45 (2005), pp. 851–857.

[116] T. Gladman. *The physical metallurgy of microalloyed steels*. CRC Press, 1996.

[117] A. Yoshie et al. "Modelling of microstructural evolution and mechanical properties of steel plates produced by thermo-mechanical control process".
In: *ISIJ International* 32 (1992), pp. 395–404.

[118] D.B. Williams and C.B. Carter. *Transmission Electron Microscopy*.
Springer, 1996.

[119] E.A. Kenikt and P.J. Maziasz. "Application of extraction replicas and analytical electron microscopy to precipitate phase studies".
In: *Microbeam Analysis Society analytical electron microscopy meeting* (1984).

[120] D.E. Bradley. "Replica techniques in applied electron microscopy". In: *Journal of the Royal Microscopial Society* 79 (1960), pp. 101–118.

[121] A.R. Marder. "Replication microscopy techniques for NDE". In: *ASM Handbook* 17 (1989), pp. 52–56.

[122] C. Lefrou, J. Fouletier, and P. Fabry. "Conductivité des électrolytes". In: *Techniques de l'ingénieur* K840 V1 (2010).

[123] A.J. Bard, G. Inzelt, and F. Scholz. *Electrochemical dictionary*. Springer, 2012.

[124] T. Kawai, H. Nishihara, and K. Aramaki. "The corrosion reactions of iron with some complexing agents in an electrolytic anhydrous methanol solution". In: *Corrosion Science* 36 (1994), pp. 2111–2124.

[125] F. Kurosawa, I. Taguchi, and R. Matsumoto. "Observation and analysis of carbides in steels using non-aqueous electrolyte-potentiostatic etching method". In: *The journal of the Japan Institute of Metals* 44 (1980), pp. 1288–1295.

[126] F. Kurosawa et al. "Observation and analysis of nitrides in steels using the non-aqueous electrolyte-potentiostatic etching method". In: *The journal of the Japan Institute of Metals* 45 (1981), pp. 63–71.

[127] R. Varano et al. "FE-SEM study of fine Nb precipitates in carbon extraction replicas". In: *Materials Science Forum* 500-501 (2005), pp. 663–668.

[128] H.H. Cölfen. "Characterization of polymers and particles with the analytical ultracentrifuge". In: *Proceedings of SPIE* 10291 (1997), pp. 525–552.

[129] K.L. Planken and H. Cölfen. "Analytical ultracentrifugation of colloids". In: *Nanoscale* 2 (2010), pp. 1849–1869.

[130] W. Mächtle and L. Börger. *Analytical ultracentrifugation of polymers and nanoparticles*. Springer, 2006.

[131] J. Ma et al. "Variable field analytical ultracentrifugation: II. Gravitational sweep sedimentation velocity". In: *Biophysical Journal* 110 (2016), pp. 103–112.

[132] T.L. Williams, G.E. Gorbet, and B. Demeler. "Multi-speed sedimentation velocity simulations with UltraScan-III". In: *European Biophysics Journal* 47 (2018), pp. 815–823.

[133] J. Walter and W. Peukert. "Dynamic range multiwavelength particle characterization using analytical ultracentrifugation". In: *Nanoscale* 8 (2016), pp. 7484–7495.

[134] W.F. Stafford. "Boundary analysis in sedimentation transport experiments: a procedure for obtaining sedimentation coefficient distributions using the time derivative of the concentration profile". In: *Analytical Biochemistry* 203 (1992), pp. 295–301.

[135] W.F. Stafford. "Analytical ultracentrifugation: sedimentation velocity analysis". In: *Current Protocols in Protein Science* 31 (2003), pp. 20.7.1–20.7.11.

[136] W.F. Stafford. "Boundary analysis in sedimentation velocity experiments". In: *Methods in Enzymology* 240 (1994), pp. 478–501.

[137] W.F. Stafford. "Analysis of reversibly interacting macromolecular systems by time derivative sedimentation velocity".
In: *Methods in Enzymology* 323 (2000), pp. 302–325.

[138] K.E. Van Holde and W.O. Weischet.
"Boundary analysis of sedimentation-velocity experiments with monodisperse and paucidisperse solutes".
In: *Biopolymers* 17 (1978), pp. 1387–1403.

[139] P. Schuck and P. Rossmanith. "Determination of the sedimentation coefficient distribution by least-squares boundary modeling".
In: *Biopolymers* 54 (2000), pp. 328–341.

[140] P. Schuck. "Size-distribution analysis of macromolecules by sedimentation velocity ultracentrifugation and Lamm equation modeling".
In: *Biophysical Journal* 78 (2000), pp. 1606–1619.

[141] L.A. Holladay. "Simultaneous rapid estimation of sedimentation coefficient and molecular weight". In: *Biophysical Chemistry* 11 (1980), pp. 303–308.

[142] B. Demeler and H. Saber. "Determination of molecular parameters by fitting sedimentation data to finite-element solutions of the Lamm equation".
In: *Biophysical Journal* 74 (1998), pp. 444–454.

[143] J. Walter. *Multidimensional characterization of nanoparticles by means of analytical ultracentrifugation*. Verlag Dr. Hut, 2017.

[144] V. Mittal, A. Völkel, and H. Cölfen. "Analytical ultracentrifugation of model nanoparticles: comparison of different analysis methods".
In: *Macromolecular Bioscience* 10 (2010), pp. 754–762.

[145] J. Walter et al. "Multidimensional analysis of nanoparticles with highly disperse properties using multiwavelength analytical ultracentrifugation".
In: *ACS Nano* 8 (2014), pp. 8871–8886.

[146] H.M. Strauss et al. "Performance of a fast fiber based UV/Vis multiwavelength detector for the analytical ultracentrifuge".
In: *Colloid and Polymer Science* 286 (2008), pp. 121–128.

[147] J. Pearson and H. Cölfen.
"Practical aspects of multiwavelength analytical ultracentrifugation".
In: *Instruments* 3 (2019).

[148] H. Cölfen et al. "The open AUC project".
In: *European Biophysics Journal* 39 (2010), pp. 347–359.

[149] W. Hergert and T. Wriedt. *The Mie theory - Basics and applications*.
Springer, 2012.

[150] C.F. Bohren and D.R. Huffman.
Absorption and scattering of light by small particles. John Wiley & Sons, 1983.

[151] C. Mätzler. *MATLAB functions for Mie scattering and absorption*.
Institute of Applied Physics, University of Bern, 2002.

[152] C. Mätzler. *MATLAB functions for Mie scattering and absorption - Version 2*.
Institute of Applied Physics, University of Bern, 2002.

[153] K.D. Hartlen, A.P.T. Athanasopoulos, and V. Kitaev.
"Facile preparation of highly monodisperse small silica spheres (15 to >200 nm) suitable for colloidal templating and formation of ordered arrays".
In: *Langmuir* 24.5 (2008), pp. 1714–1720.

[154] K. Thompson et al.
"In situ site-specific specimen preparation for atom probe tomography".
In: *Ultramicroscopy* 107 (2007), pp. 131–139.

[155] L.M. Rothleutner. "Influence of reheat temperature and holding time on the interaction of V, Al, and N in air-cooled forging steels".
MSc thesis, p.25. Colorado School of Mines, United States of America, 2016.

[156] X. Sun et al. *Nanoseparation using density gradient ultracentrifugation*.
Springer, 2018.

[157] M. Hanauer et al. "Separation of nanoparticles by gel electrophoresis according to size and shape". In: *Nano Letters* 7.9 (2007), pp. 2881–2885.

[158] S. Frost and M. Ulbricht. "Thermoresponsive ultrafiltration membranes for the switchable permeation and fractionation of nanoparticles".
In: *Journal of Membrane Science* 448 (2013), pp. 1–11.

[159] T.R. Gaborski et al. "High performance separation of nanoparticles with ultrathin porous nanocrystalline silicon membranes".
In: *ACS Nano* 4.11 (2010), pp. 6973–6981.

[160] P.S. Fedotov et al. "Fractionation and characterization of nano- and microparticles in liquid media".
In: *Analytical and Bioanalytical Chemistry* 400 (2011), pp. 1787–1804.

[161] N. Surugau and P.L. Urban.
"Electrophoretic methods for separation of nanoparticles".
In: *Journal of Separation Science* 32.11 (2009), pp. 1889–1906.

[162] W. Wu et al.
"Two-step size- and shape-separation of biosynthesized gold nanoparticles".
In: *Separation and Purification Technology* 106 (2013), pp. 117–122.

[163] G.-T. Wei, F.-K. Liu, and C.R.C. Wang. "Shape separation of nanometer gold particles by size-exclusion chromatography".
In: *Analytical Chemistry* 71.11 (1999), pp. 2085–2091.

[164] T. Takeuchi et al. "Hydrodynamic chromatography of silica colloids on small spherical nonporous silica particles".
In: *Analytical Sciences* 25.2 (2009), pp. 301–306.

[165] K.M. Krueger et al. "Characterization of nanocrystalline CdSe by size exclusion chromatography".
In: *Analytical Chemistry* 77.11 (2005), pp. 3511–3515.

[166] C.H. Fischer and M. Giersig. "Analysis of colloids VII. Wide-bore hydrodynamic chromatography, a simple method for the determination of particle size in the nanometer size regime".
In: *Journal of Chromatography A* 688 (1994), pp. 97–105.

[167] Z. Aspanut et al. "Light-scattering and turbidimetric detection of silica colloids in size-exclusion chromatography".
In: *Analytical and Bioanalytical Chemistry* 391 (2008), pp. 353–359.

[168] H. Guo, G. Stan, and Y. Liu.
"Nanoparticle separation based on size-dependent aggregation of nanoparticles due to the critical Casimir effect".
In: *Soft Matter* 14.8 (2018), pp. 1311–1318.

[169] P.D. Gallagher, M.L. Kurnaz, and J.V. Maher. "Aggregation in polystyrene-sphere suspensions in near-critical binary liquid mixtures". In: *Physical Review A* 46.12 (1992), pp. 7750–7755.

[170] B. Rathke, H. Grüll, and D. Woermann. "Stability of dilute colloidal silica suspensions in the vicinity of the binodal curve of the system 2-butoxyethanol/water". In: *Journal of Colloid and Interface Science* 192 (1997), pp. 334–337.

[171] P. Qiu and C. Mao. "Viscosity gradient as a novel mechanism for the centrifugation-based separation of nanoparticles". In: *Advanced Materials* 23 (2011), pp. 4880–4885.

[172] D. Steinigeweg et al. "Fast and cost-effective purification of gold nanoparticles in the 20-250 nm size range by continuous density gradient centrifugation". In: *Small* 7.17 (2011), pp. 2443–2448.

[173] C.R. Mace et al. "Aqueous multiphase systems of polymers and surfactants provide self-assembling step-gradients in density". In: *Journal of the American Chemical Society* 134 (2012), pp. 9094–9097.

[174] O. Akbulut et al. "Separation of nanoparticles in aqueous multiphase systems through centrifugation". In: *Nano Letters* 12 (2012), pp. 4060–4064.

[175] M. Klos. "Characterisation of nanoparticles extracted from steel by means of flow field-flow fractionation". Vertiefungspraktikum. Universität des Saarlandes, Germany, 2018.

[176] V. Goertz, N. Dingenouts, and H. Nirschl. "Comparison of nanometric particle size distributions as determined by SAXS, TEM and analytical ultracentrifuge". In: *Particle & Particle Systems Characterization* 26 (2009), pp. 17–24.

[177] J. Webel et al. "Particle encapsulation techniques for atom probe tomography of precipitates in microalloyed steels". In: *Ultramicroscopy* 223.113219 (2021).

[178] "Standard test methods for determining average grain size". In: *ASTM* E112-10 (2010).

[179] F. Vurpillot, A. Bostel, and D. Blavette. "Trajectory overlaps and local magnification in three-dimensional atom probe". In: *Applied Physics Letters* 76 (2000), pp. 3127–3129.

[180] F. Perrard et al. "A small-angle neutron scattering study of fine-scale NbC precipitation kinetics in the α-Fe-Nb-C system". In: *Journal of Applied Crystallography* 39 (2006), pp. 473–482.